ATOMIC AND MOLECULAR LAYER DEPOSITION FOR EFFICIENT CAPACITIVE DEIONIZATION, PLASMA CORROSION PROTECTION AND STABLE HIGH-ENERGY LITHIUM ION BATTERIES

By

Jasmine Melissa Wallas

B.A., Smith College, 2011

A thesis submitted to the

Faculty of the Graduate School of the

University of Colorado in partial fulfillment

of the requirement for the degree of

Doctor of Philosophy

Department of Chemistry

2019

This thesis entitled:

Atomic and Molecular Layer Deposition for Efficient Capacitive Deionization, Plasma Corrosion Protection and Stable High-Energy Lithium Ion Batteries

written by Jasmine Melissa Wallas

has been approved for the Department of Chemistry

_____

Steven M. George

_____

Michael P. Marshak

Date_____

The final copy of this thesis has been examined by the signatories, and we find that both the content and the form meet acceptable presentation standards of scholarly work in the above mentioned discipline.

Wallas, Jasmine Melissa (Ph.D., Materials Chemistry)

Atomic and Molecular Layer Deposition for Efficient Capacitive Deionization, Plasma Corrosion Protection and Stable High-Energy Lithium Ion Batteries

Thesis directed by Professor Steven M. George

Atomic layer deposition (ALD) is a technique to deposit thin films with great precision. Molecular layer deposition (MLD), developed as an analog of ALD, is a technique to deposit organic polymer or hybrid organic-inorganic thin films with great precision. ALD and MLD techniques have played a major role in advancing many fields, such as in semiconductor fabrication, sensors, energy production and energy storage. In this dissertation I describe three research projects in which ALD or MLD thin films were developed for applications in water desalination, energy storage and semiconductor fabrication. One project investigated an ultrathin polyamide coating developed for the silicon anode in lithium-ion batteries. The coating, deposited via spatial molecular layer deposition (MLD), enhanced the structural integrity of the anode and permitted stable electrochemical cycling. In the second project thin-film sodium manganese oxide (NMO) was used as an electrode coating in capacitive deionization (CDI). CDI is an emerging electrochemical desalination technology that shows promise but suffers from capacity and efficiency limitations. An NMO coating on the cathode within a CDI device improved desalination capacity and efficiency. The focus of the third project was the development of ALD YF_3 and YO_xF_y thin films with a

tunable composition to be deployed as plasma corrosion barriers. These new ALD chemistries have distinct properties and may interact differently with different reactive plasmas. With the high level of control over the composition of these films, it may be possible to tailor a protective coating for the type of reactive plasma used in each unique plasma chamber. These three projects highlight the versatility and value of ALD and MLD thin films.

Acknowledgements

Scientific pursuits are by nature collaborative. To that end, I'd like to acknowledge the many people and institutions who contributed to this dissertation in one way or another. Foremost, I'd like to thank my mentors, collaborators and funders, without whom this dissertation would not exist. I'm grateful for the support I received from my advisor, Professor Steven George, who provided guidance throughout my graduate work and encouraged perseverance and self-direction. I'm also grateful for the support I received from Professors Chunmei Ban and Matthias Young, who both taught me a lot about the scientific process. I'd like to thank all of my collaborators for their valuable contributions to this research. I'd also like to thank the funding organizations without whom this research would not have been possible. Funding for the research in Chapter Three was provided by the National Renewable Energy Laboratory and the Vehicle Technologies Office of the U.S. Department of Energy (DOE). Funding for the research in Chapter Four was provided by a DOE SBIR grant subcontracted through ALD NanoSolutions. Funding for the research in Chapter Five was funded by Applied Materials, Inc.

I would like to thank all of the past and present members of the George group for their help and guidance over the years. Special thanks go to my many lab mates, and especially to Andrew Cavanagh, Daniel Higgs, Jaime Dumont, Joel Clancey, Arrelaine

Dameron, Dave Zywotko, Austin Cano, Tyler Myers and Jonas Gertsch for providing both technical and moral support, both in and outside of the lab.

I have been fortunate to have many wonderful friends outside of the lab who have supported me through graduate school. I'm grateful for my first-year buddies Orion Pierce, Dylan Mori, Steve Fatur and James Utterback. The members of BC, Hayden Hamby, Jon Church, Alyssa Landin, Rob Wells and Dave Zywotko, who brought joy into every week. Allison Harris, Yonit Bousany, Alyssa Stanek, Angela Oliverio, Ashley Heist and Nicole Williamson deserve a big shout out for all of the support and suppers over the years. I'd also like to thank Rachel O'Sullivan for helping me through that final push in putting this dissertation together.

Finally, I would like to acknowledge my family for the encouragement and support that they have provided over the years. Thanks go to my parents and grandparents, not only for supporting me through my many, many years of schooling, but also for showing me the value in knowledge. Thanks also go to my siblings for supporting and encouraging me to pursue science. Most of all, I'd like to thank my partner, Laura Putnam, for her steadfast encouragement, support and patience through this entire process. I can't thank you enough.

Table of Contents

List of Figures

1. Introduction

In the last twenty years, with technology trending smaller and more intricate, thin film research has become an increasingly important topic. Thin films are generally defined by their thickness, ranging from less than 1 nm to about 100 μm. The push towards miniaturization has led to a greater focus on nanoscale materials in many fields. If a material is to maintain its nanoscale properties, and thus its relevance in the current market, any coating applied to it must be a thin film. Thin films have applications in areas such as semiconductor fabrication, displays, energy storage, and energy production. Because of thin film technology, a single integrated circuit can contain millions of transistors and an optical device can be mechanically flexible. As thin film technology evolves, the number and type of applications for which this field of technology is relevant will continue to expand rapidly.

1.1 Atomic Layer Deposition and Molecular Layer Deposition

Atomic layer deposition (ALD) is a technique to deposit thin films with great precision. Because of its ability to deposit very conformal films of precise thickness onto nanoscale structures with high aspect ratios, ALD has played a key role in device miniaturization over the last twenty years. ALD consists of a series of self-limiting reactions that take place between gas-phase reactants, called precursors, and a surface.

Each precursor used in the reaction sequence is separated from the others, thereby allowing a high level of control over the deposition. Complete separation of the precursors prevents their reaction in the gas phase, which can result in the deposition of granular and inhomogeneous films. Precursors are exposed to the surface sequentially to deposit a thin film in a layer-by-layer fashion. These techniques produce films that are generally homogeneous, dense and pin-hole free. For this reason, ALD is relevant in a number of key applications, as will be discussed in a later section.

ALD is most often composed of a binary reaction sequence, with two separate precursor exposures and two half reactions. The most prevalent ALD methods deposit metal oxide films. The general reaction sequence to deposit a metal oxide is 1) the reaction of a gaseous metal complex with hydroxyl groups on the surface of a substrate, and 2) the reaction of a surface-bound metal complex with a gaseous oxygen source. A schematic of this reaction sequence is shown in Figure 1.1. The metal complex might, for example, be a metal halide or metal alkyl. The oxygen source is commonly water but can also be O_2, O_3, or an energetic species. The two half reactions that make up one cycle of ALD are a condensation reaction that occurs upon metal complex exposure and a hydrolysis reaction that occurs upon oxygen source exposure. This reaction sequence is repeated to deposit the desired film thickness, thereby enabling a high level of thickness control.

Along with thickness precision, ALD offers a high level of control over the

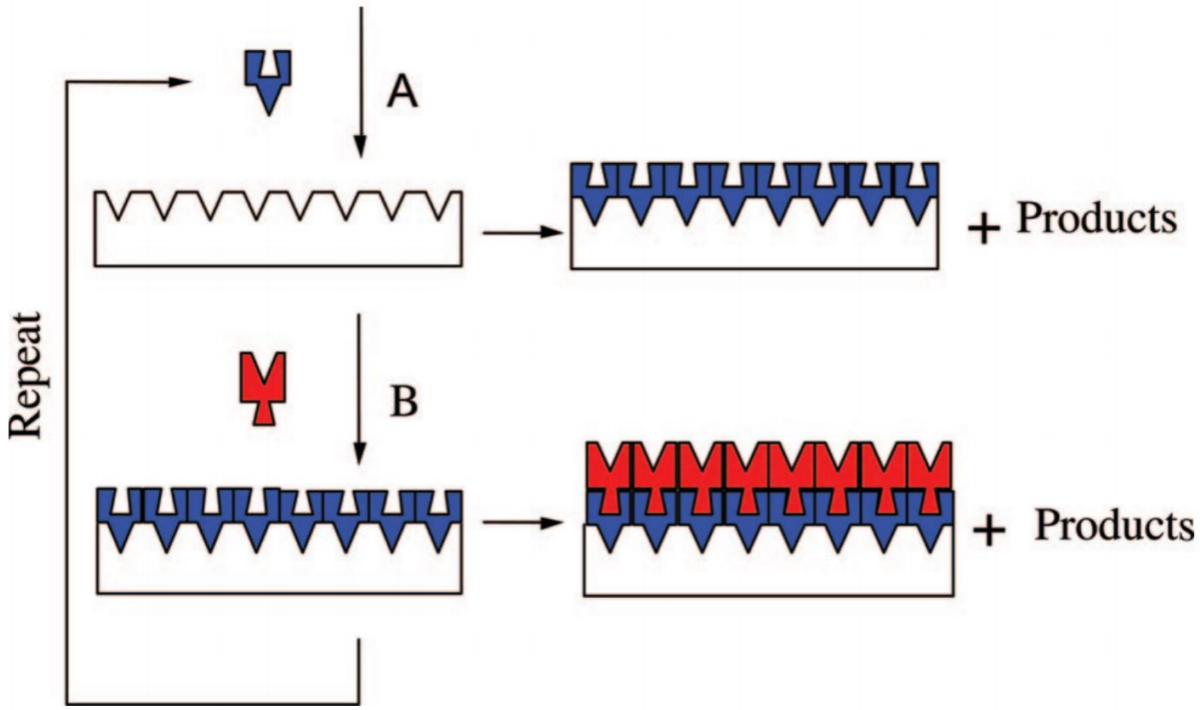

Figure 1.1 ALD scheme showing sequential, self-limiting surface reactions that produce ultrathin conformal films with Å-level control. *Reproduced from George, S. M. Chemical Reviews 2009, 110, 111-131.*

composition of the film. With careful selection of precursors and dosing sequence, ALD can be used to deposit uniform thin films of single elements, such as W[1] or Pt,[2] compounds containing two elements, such as Al_2O_3[3] or BN,[4] or compounds containing several elements, such as $Li_7La_3Zr_2O_{12}$[5] or Cu_2ZnSnS_4.[6] Multi-element compounds are often deposited using a super cycle approach, where multiple ALD reactions are alternated periodically to deposit a uniform film. A super cycle approach can also be used to deposit a nanolaminate thin film, composed of distinct nanoscale layers of different materials. In this case, the choice of materials in the nanolaminate and the thickness of the interlayers can be tuned to create thin films with novel electronic and mechanical properties. For example, ZrO_2-Al_2O_3 nanolaminates were recently developed that contain metastable polymorphs of ZrO_2 with higher permittivity than normally seen.[7] Novel ALD thin films are continually being developed, expanding the number of applications in which ALD is relevant.

ALD can be categorized by the type of excitation that drives the reactions. The excitation method can be thermal, plasma, or electron enhanced. Thermal ALD is likely the simplest of the three, and it is widely used to deposit both metal and ceramic films. Reaction temperatures generally range from 100 – 500 ˚C. With thermal ALD it is possible to deposit thin films onto nanoscale and high aspect ratio structures. Plasma-enhanced ALD offers the ability to deposit materials that cannot otherwise be controllably deposited with thermal ALD as well as lower deposition temperatures.

Using plasma, thin films can be deposited onto thermally sensitive substrates, such as polymers or biological materials. The trade-off in plasma-enhanced ALD is the inability to coat high aspect ratio structures due to ion or radical recombination.[24] Electron-enhanced ALD is a relatively new technique that uses low energy electrons to excite surfaces to deposit crystalline thin films at low temperatures of 25 -100 ˚C. Electron-enhanced ALD has been used to deposit crystalline GaN,[25] Si[26] and BN.[27]

Unlike other technologies, the development of ALD has not evolved in a linear fashion. In fact, ALD was independently invented twice in the 20th century. The first time ALD was invented was in the 1960s by Soviet Union scientists Professors Aleskovskii and Kolt'sov.[18] They called the technology 'molecular layering. The modern field of ALD as we know it today has developed from the initial inventions of Dr. Tuomo Suntola and his colleagues in Finland. Suntola, along with Jorma Antson, Sven Lindfors and Arto Pakkala developed polycrystalline ZnS ALD films for flat panel displays based on thin film electroluminescence (TFEL).[19] In 1974, Suntola and Antson filed the first international patent on the technology.[20] Suntola claimed that he learned about the earlier iteration of the technology developed by the Soviet scientists in 1990.[21] Suntola and colleagues originally called this deposition process 'atomic layer epitaxy' or ALE. The process was slowly rebranded ALD, as the deposition of amorphous, not epitaxial, films became more prevalent. The term ALD was cemented when it was used to name the first AVS ALD conference in 2001, chaired by Steven M. George.[22] Through

the 1980s ALD was primarily marketed for TFEL displays. TFEL displays were widely used in signs and computer monitors in the 1980s and early 1990s. Today TFEL technology has largely been replaced by other displays with more color depth, though it is still used for some specialized cases, such as transport applications where extreme conditions exist.

In the 1990s the field started to diversify and expand. The first example of ALD for DRAM was reported in 1998 and ALD was widely adopted by the semiconductor industry in the early 2000s for metal oxide transistors.[22] In 2007 hafnium-based ALD was added to Intel's fabrication line for the creation of metal oxide field effect transistors.[23] The field has grown exponentially in recent years. As of January of 2018, 11,000 papers on ALD have been published by about 21,500 scientists.[23]

Molecular layer deposition (MLD) is a technique to deposit organic polymer or hybrid organic-inorganic thin films with great precision. It was developed as an analog of ALD and greatly increased the possibilities for controllably depositing pin-hole free conformal thin films. MLD was invented in 1991 by Tetsuzo Yoshimura and colleagues in Japan.[11] They demonstrated the thin film deposition of two different aromatic polyimides via MLD. This process uses the same approach as ALD, with sequential self-limiting surface reactions with gaseous precursors. Like ALD, MLD often uses two precursors and consists of a binary reaction sequence. However, instead of depositing atomic layers, as in ALD, MLD deposits molecular layers.

Like ALD, MLD offers precise film thickness control and can conformally coat high aspect ratio structures. MLD also offers a high level of composition control and can be used to deposit nanolaminates and other unique thin film structures that cannot be deposited using other methods. Many MLD materials have been developed. Organic MLD materials include polyamides,[8–10] polyimides,[11,12] polyureas,[13] polyesters[14] and polyurethanes.[15] Hybrid organic-inorganic MLD processes have also been developed. Typically, these hybrid films are metal alkoxides, sometimes referred to as 'alucones.' They are deposited using an organic diol and a metal organic precursor. The length of the alkane chain and the number of functional groups in the organic precursor effects the mechanical properties of the resulting alucone film.[16] Super cycles can be used to deposit mixed ALD-MLD films with properties that can be tuned with the ratio of the film composition.

ALD and MLD have some drawbacks and they are not appropriate for every application. Importantly, they are costly processes. The reactors and equipment needed to deposit and characterize ALD and MLD films are costly both to purchase and maintain. Compared to other deposition techniques, ALD is generally a slower process and MLD is even slower. ALD deposition rates can be orders of magnitude slower than those of other deposition techniques. There can also be significant optimization times for the deposition of new materials, deposition on unique substrates, or deposition under new reactor conditions. Depending on the material to be deposited, heat sensitive

substrates can present challenges. There are also a limited number of materials that can be deposited with ALD and MLD. Materials are limited by the number of favorable reaction pathways possible and the availability of appropriate precursors. Precursors must be volatile, stable at elevated temperatures, and undergo favorable reactions on the substrate surface. Ideal precursors should also have smaller ligands in order to minimize steric hindrance of surface sites. These limitations have prevented the wider adoption of some ALD and MLD technologies.

In comparison to ALD, MLD does present some unique deposition challenges and material limitations. Foremost among these challenges is the availability of MLD precursors with sufficient vapor pressures, considering that reaction temperatures must be low enough to prevent thermal decomposition. Vapor pressures for organic precursors are often orders of magnitude lower than those of metal organic precursors. Low precursor vapor pressures can cause precursor condensation on the substrate or reactor walls, thereby preventing precursor separation and causing uncontrolled film growth. Another challenge in MLD is the possibility of homobifunctional organic precursors reacting twice with the surface, thereby causing the loss of surface sites.[17] The possibility of double reactions increases with the length of the alkyl chain in the organic precursor, limiting the polymer structure. Finally, MLD of organic thin films is limited to polymers that can be deposited via condensation polymerization. Despite

these limitations, polymer and hybrid organic-inorganic MLD films have been developed for a wide range of applications, as will be discussed in later in this chapter.

1.2 Other Thin Film Deposition Techniques

Because ALD and MLD are costlier and more time-consuming than other deposition methods, it is important to consider the particular needs of a system when selecting a thin film deposition technique for a particular application. There are several ways to deposit a thin film. Besides ALD, some of the more common thin film deposition techniques are chemical vapor deposition (CVD), physical vapor deposition (PVD), and chemical solution deposition (CSD) and spin coating. Each of these techniques has its merits and is particularly suited for certain applications.

CVD describes a broad range of techniques that deposit thin films via chemical reactions of vapor phase precursors with a surface. In fact, ALD is often considered a sub-category of CVD. Besides ALD, there are many other sub-categories of CVD that have been developed to deposit different thin film materials. These sub-categories are distinguished by deposition pressure, temperature and excitation method. One or more precursors can be used, and they can be dosed concurrently or sequentially. Precursors can react with the surface or decompose on the surface. CVD is used to deposit metals, inorganic materials and polymers, for diverse applications including in semiconductor fabrication, optical fibers, solar energy and protective coatings. CVD thin films are

generally homogeneous and have a uniform thickness. They can be deposited with high deposition rates and short processing times. In exchange for higher growth rates, CVD is less controlled and less precise than ALD. Reaction of precursor molecules in the gas phase can result in granular thin films with higher surface roughness. Moreover, CVD onto high aspect ratio structures is often less conformal than ALD. CVD is therefore most suited for the deposition of uniform thin films onto flat substrates, where thickness precision is not needed, or the desired film thickness is on the scale of μm.

PVD describes any method to deposit thin films via condensation of the vaporized form of a solid. Several vaporization methods are used, including sputtering, thermal evaporation and electron beam evaporation. In sputtering deposition, a target is bombarded with energetic particles, causing the release of target atoms from the solid state via a momentum transfer. Energetic particles can be ions or atoms and are often excited by plasma or ion beam. Unlike other PVD methods, sputtering can be used when the material to be deposited has a high melting point. However, sputtered films often contain impurities and have a rougher morphology. Thermal evaporative PVD uses heat to vaporize the target solid. Generally, thermal evaporative PVD describes the deposition of amorphous films at high deposition rates under low vacuum, 10^{-2} Torr. Molecular beam epitaxy (MBE) is a sub-category of thermal evaporative PVD that deposits highly crystalline films. MBE uses effusion cells to direct a 'beam' of vaporized solid to the substrate, where the vapor has low interparticle collisions and long mean

free paths. MBE must be conducted under high vacuum, 10^{-8} – 10^{-12} Torr. MBE is often used to deposit crystalline GaAs for semiconductor applications. Thermal evaporative PVD methods can be simple or complex and can be used to deposit amorphous or crystalline materials. Electron beam evaporative PVD uses electron bombardment to vaporize a solid for deposition. Electron beam evaporation uses high vacuum, 10^{-6} Torr, and an electron accelerating voltage between 3 and 40 kV. Electron beam PVD has better thermal efficiency than thermal processes and can be used to deposit thermally-sensitive materials. The drawbacks of this method are 1) the emission of X-rays and secondary electrons which can damage substrates or reactor components and 2) nonuniform evaporation due to the degradation of the electron gun filament. Broadly, PVD methods offer the ability to deposit thin films of almost any inorganic material with very fast deposition rates, up to several hundred μm per minute. However, these deposition methods, called "line-of-site" methods, can only coat surfaces directly in line with the target source uniformly, and non-uniformity due to shadowing effects can occur. Moreover, PVD of multi-element thin films presents challenges. PVD methods are therefore best suited for the deposition of inorganic thin films onto flat substrates with thicknesses on the order of hundreds of μm.

CSD describes any technique used to deposit a thin film using a chemical precursor solution. CSD methods include the sol-gel process, metal-organic decomposition (MOD), spin-coating, and electroplating. The sol-gel process deposits

oxide-based ceramic thin films via a two-step hydrolysis and condensation reaction. Precursors with weak ligands, such as halides or nitrates, are hydrolyzed and condensed to form a colloidal nanoparticle suspension, the 'sol'. This suspension is further poly-condensed to form a polymeric gel. The gel can be dried to produce a dense thin film. MOD is a simple process to make a ceramic thin film in which metal-organic precursors dissolved in solvent are solution deposited and then heat treated to remove the solvent and decompose the precursor. MOD is suitable for the deposition of single component ceramics and it offers very little control over film thickness. Spin coating is a solution-based deposition technique that offers some control over the thickness of the film. In spin coating, a small amount of coating material dispersed in a volatile solvent is applied to the center of the substrate. The substrate is spun to disperse the coating solution with centrifugal force. The concentration and viscosity of the solution, and the rotation speed of the substrate effect the thickness of the coating. Spin coating is used to deposit photoresist thin films for lithography. The major advantages of CSD are that they don't use vacuum, allowing for lower costs and less energy consumption, and thermally-sensitive materials can be used. The main disadvantage of CSD is the use of large amounts of solvent, precluding the use of solvent-sensitive substrates and presenting the challenge of large amounts of solvent waste.

1.3 Applications of ALD and MLD Thin Films

Though there is a large range of alternative thin film deposition methods available, ALD and MLD have proven themselves particularly useful in the advancement of miniaturization in several fields. Ongoing research and development have focused on ALD and MLD in such fields as semiconductor fabrication, optical coatings, sensors, energy production, energy storage, and biomedicine.

By far the greatest strides in the development of ALD processes have been driven by the needs of the semiconductor industry. ALD coatings have enabled the continual miniaturization of both transistors and capacitors. ALD processes, first introduced into the manufacturing of field-effect transistors (FETs) in 2007,[23] have enabled the industry to meet the projections put forth by Moore's law. Moore's law, which is of course not a scientific law at all, is a projection for the industry based on observations put forth by Gordon Moore, the founder of Intel, who found that the number of transistors on a single chip doubles every two years. ALD processes are used to deposit highly insulating metal oxides, such as hafnium oxide, used as gate dielectrics in metal oxide semiconductor field-effect transistors (MOSFETs).[28,29] ALD and MLD thin films are also used to deposit diffusion barriers and backend interconnects.[30,31] A dynamic random-access memory (DRAM) cell consists of a MOSFET paired with a capacitor. Miniaturization of these memory devices and others have been enabled by ALD or MLD.[28,32] Because they can enable the deposition of novel high-purity thin films on high

aspect ratio structures, ALD and MLD have greatly advanced the semiconductor industry.

ALD and MLD have also furthered the development of new energy production methods, especially in the fields of fuel cells and solar energy. ALD has been used for the deposition of active materials and as protective or passivation barriers in both fuel cells and solar energy devices. In the area of fuel cells, ALD has been used to deposit catalysts, such as platinum nanoparticles in proton exchange membrane fuel cells (PEMFCs);[33] solid electrolyte, such as yttria-stabilized zirconia in solid oxide fuel cells (SOFCs);[34] and protective coatings, such as TiO_2[35] or Al_2O_3[36] thin films on catalyst particles to prevent sintering. ALD has enabled the development of thin film photovoltaic devices, where it has been used to deposit, for example, a Cu_2ZnSnS_4 absorber material.[6] ALD has also been used for band-structure engineering,[37,38] surface passivation[39] and protective coatings[40,41] in solar cells.

ALD and MLD have also furthered the development of better energy storage devices. As portable electronic devices become more prevalent, and electric vehicles become more popular, better energy storage strategies are needed. While some emerging battery systems seem promising, lithium-ion batteries are still at the forefront of energy storage technology today. Still, there is an increasing demand for higher energy, longer lasting, and safer batteries. There has been a push to increase the surface-to-volume ratios of electrode materials in order to facilitate better Li^+ diffusion and

electron transport. Increased surface area also increases the likelihood of unfavorable side reactions, which can negatively affect cycling lifetime and safety. In 2010 Jung et al. discovered that a thin Al_2O_3 ALD protective coating on the cathode of lithium-ion batteries can significantly increase battery cycling stability.[42] The ALD coating acts as an 'artificial SEI' that facilitates the creation of a stable interface between the electrode and electrolyte. ALD is uniquely suited for this purpose because 1) it can conformally coat the microstructural cathode material and 2) it can deposit a very thin, Å-scale coatings to avoid a large increase in interfacial resistance. More recently, MLD thin films have been implemented as coatings on silicon anodes for next-generation lithium-ion batteries. Silicon anodes have a capacity that is roughly twice as high as graphite, which is the anode material used in today's batteries. The shortcoming of silicon anodes is that they undergo large volume changes upon lithiation and delithiation, which causes a loss of electrical connectivity and capacity over a number of cycles. Hybrid organic-inorganic MLD alkoxide coatings, with higher elasticity than ALD coatings,[16] were used to mechanically stabilize the volume expansion and enabled longer cycling stability.[43] There has also been progress in the development of active ALD thin films for solid-state lithium-ion batteries. Solid-state batteries are appealing because they avoid the use of hazardous and flammable solvents and are therefore safer than conventional liquid cells. However, significant challenges arise from the degradation of solid electrolytes, the decreased conductivity and the increased surface resistance in these cells. ALD has

been used to deposit thin films of solid electrolyte, such as $Li_7La_3Zr_2O_{12}$ (LLZO), that can enable 3D solid state battery architectures for enhanced rate capability and energy density.[5] Moreover, ALD Al_2O_3 coatings have been used to reduce the interfacial resistance between solid electrolyte and lithium by enhancing wetting of the lithium metal on the garnet surface.[44]

In this dissertation I describe three different examples of ALD or MLD thin films and their applications. In Chapter 3, I describe the development of a thin film polyamide MLD coating for a high energy silicon anode for lithium-ion batteries that enables stable electrochemical cycling. In Chapter 4, I describe the development of a thin film sodium manganese oxide coating on the cathode of a capacitive deionization (CDI) device to enhance the capacity and efficiency of water desalination. In Chapter 5, I describe the development of new yttrium-based ALD chemistries that may have applications as protective coatings for plasma chambers used to fabricate semiconductor devices.

1.4 References

(1) Grubbs, R. K.; Steinmetz, N. J.; George, S. M. *J. Vac. Sci. Technol. B Microelectron. Nanom. Struct.* **2004**, *22* (4), 1811.

(2) Kessels, W. M. M.; Knoops, H. C. M.; Dielissen, S. A. F.; Mackus, A. J. M.; van de Sanden, M. C. M. *Appl. Phys. Lett.* **2009**, *95* (1), 13114.

(3) George, S. M.; Ott, A. W.; Klaus, J. W. *J. Phys. Chem.* **1996**, *100* (31), 13121–13131.

(4) Ferguson, J. .; Weimer, A. .; George, S. . *Thin Solid Films* **2002**, *413* (1–2), 16–25.

(5) Kazyak, E.; Chen, K.-H.; Wood, K. N.; Davis, A. L.; Thompson, T.; Bielinski, A. R.; Sanchez, A. J.; Wang, X.; Wang, C.; Sakamoto, J.; Dasgupta, N. P. *Chem. Mater.* **2017**, *29* (8), 3785–3792.

(6) Thimsen, E.; Riha, S. C.; Baryshev, S. V.; Martinson, A. B. F.; Elam, J. W.; Pellin, M. J. *Chem. Mater.* **2012**, *24* (16), 3188–3196.

(7) Kukli, K.; Kemell, M.; Castán, H.; Dueñas, S.; Seemen, H.; Rähn, M.; Link, J.; Stern, R.; Heikkilä, M. J.; Ritala, M.; Leskelä, M. *ECS J. Solid State Sci. Technol.* **2018**, *7* (5), P287–P294.

(8) Shao, H.-I.; Umemoto, S.; Kikutani, T.; Okui, N. *Polymer (Guildf).* **1997**, *38* (2), 459–462.

(9) Kim, A.; Filler, M. A.; Kim, S.; Bent, S. F. *J. Am. Chem. Soc.* **2005**, *127* (16), 6123–6132.

(10) Adamczyk, N. M.; Dameron, A. A.; George, S. M. *Langmuir* **2008**, *24* (5), 2081–2089.

(11) Yoshimura, T.; Tatsuura, S.; Sotoyama, W. *Appl. Phys. Lett.* **1991**, *59* (4), 482–484.

(12) Putkonen, M.; Harjuoja, J.; Sajavaara, T.; Niinistö, L. *J. Mater. Chem.* **2007**, *17* (7), 664–669.

(13) Loscutoff, P. W.; Zhou, H.; Clendenning, S. B.; Bent, S. F. *ACS Nano* **2010**, *4* (1), 331–341.

(14) Ivanova, T. V.; Maydannik, P. S.; Cameron, D. C. *J. Vac. Sci. Technol. A Vacuum, Surfaces, Film.* **2012**, *30* (1), 01A121.

(15) Lee, J. S.; Lee, Y.-J.; Tae, E. L.; Park, Y. S.; Yoon, K. B. *Science* **2003**, *301* (5634), 818–821.

(16) George, S. M.; Lee, B. H.; Yoon, B.; Abdulagatov, A. I.; Hall, R. A. *J. Nanosci. Nanotechnol.* **2011**, *11* (9), 7948–7955.

(17) George, S. M.; Yoon, B.; Dameron, A. A. *Acc. Chem. Res.* **2009**, *42* (4), 498–508.

(18) Aleskovskii, V. B.; Kol'tsov, S. I. In *Abst. Sci. Tech. Conf.* Goskhimizdat: Leningrad, 1965; p 67 (in Russian).

(19) Suntola, T.; Antson, J.; Pakkala, A.; Lindfors, S. In *SID International Symposium*; Digest of Technical Papers: San Diego, 1980; p 108.

(20) Suntola, T.; Antson, J. Method for Producing Compound Thin Films. US4058430A, 1977.

(21) Puurunen, R. L. *Chem. Vap. Depos.* **2014**, *20* (10-11–12), 332–344.

(22) Parsons, G. N.; Elam, J. W.; George, S. M.; Haukka, S.; Jeon, H.; Kessels, E.; Leskelä, M.; Poodt, P.; Ritala, M.; Rossnagel, S. M. *Cit. J. Vac. Sci. Technol. A* **2013**, *31*, 50818.

(23) Alvaro, E.; Yanguas-Gil, A. *PLoS One* **2018**, *13* (1), e0189137.

(24) Dendooven, J.; Deduytsche, D.; Musschoot, J.; Vanmeirhaeghe, R. L.; Detavernier, C. *J. Electrochem. Soc.* **2010**, *157* (4), G111.

(25) Sprenger, J. K.; Cavanagh, A. S.; Sun, H.; Wahl, K. J.; Roshko, A.; George, S. M. *Chem. Mater.* **2016**, *28* (15), 5282–5294.

(26) Sprenger, J. K.; Sun, H.; Cavanagh, A. S.; George, S. M. *J. Vac. Sci. Technol. A Vacuum, Surfaces, Film.* **2018**, *36* (1), 01A118.

(27) Sprenger, J. K.; Sun, H.; Cavanagh, A. S.; Roshko, A.; Blanchard, P. T.; George, S. M. *J. Phys. Chem. C* **2018**, *122* (17), 9455–9464.

(28) Sneh, O.; Clark-Phelps, R. B.; Londergan, A. R.; Winkler, J.; Seidel, T. E. *Thin Solid Films* **2002**, *402* (1–2), 248–261.

(29) Lee, B.; Kirkpatrick, C.; Choi, Y.-H.; Yang, X.; Wang, Y.; Yang, X.; Huang, A.; Misra, V. *ECS Transactions* **2011,** *41*, 445–450.

(30) George, S. M. *Chem. Rev.* **2010**, *110* (1), 111–131.

(31) Bent, S.; Loscutoff, P. W.; Clendenning, S. *MRS Proc.* **2010**, *1249*, 1249-F02-3.

(32) Cha, S. H.; Park, A.; Lee, K. H.; Im, S.; Lee, B. H.; Sung, M. M. *Org. Electron.* **2010**, *11* (1), 159–163.

(33) Liu, C.; Wang, C.-C.; Kei, C.-C.; Hsueh, Y.-C.; Perng, T.-P. *Small* **2009**, *5* (13), 1535–1538.

(34) Brahim, C.; Ringuedé, A.; Cassir, M.; Putkonen, M.; Niinistö, L. *Appl. Surf. Sci.* **2007**, *253* (8), 3962–3968.

(35) Biener, M. M.; Biener, J.; Wichmann, A.; Wittstock, A.; Baumann, T. F.; Bäumer, M.; Hamza, A. V. *Nano Lett.* **2011**, *11* (8), 3085–3090.

(36) Lu, J.; Elam, J. W.; Stair, P. C. *Acc. Chem. Res.* **2013**, *46* (8), 1806–1815.

(37) Törndahl, T.; Platzer-Björkman, C.; Kessler, J.; Edoff, M. *Prog. Photovoltaics Res. Appl.* **2007**, *15* (3), 225–235.

(38) Correa Baena, J. P.; Steier, L.; Tress, W.; Saliba, M.; Neutzner, S.; Matsui, T.; Giordano, F.; Jacobsson, T. J.; Srimath Kandada, A. R.; Zakeeruddin, S. M.; Petrozza, A.; Abate, A.; Nazeeruddin, M. K.; Grätzel, M.; Hagfeldt, A. *Energy Environ. Sci.* **2015**, *8* (10), 2928–2934.

(39) Schmidt, J.; Merkle, A.; Brendel, R.; Hoex, B.; de Sanden, M. C. M. van; Kessels, W. M. M. *Prog. Photovoltaics Res. Appl.* **2008**, *16* (6), 461–466.

(40) Kim, B. J.; Kim, D. H.; Lee, Y.-Y.; Shin, H.-W.; Han, G. S.; Hong, J. S.; Mahmood, K.; Ahn, T. K.; Joo, Y.-C.; Hong, K. S.; Park, N.-G.; Lee, S.; Jung, H. S. *Energy Environ. Sci.* **2015**, *8* (3), 916–921.

(41) Dong, X.; Fang, X.; Lv, M.; Lin, B.; Zhang, S.; Ding, J.; Yuan, N. *J. Mater. Chem. A*

2015, *3* (10), 5360–5367.

(42) Jung, Y. S.; Cavanagh, A. S.; Dillon, A. C.; Groner, M. D.; George, S. M.; Lee, S.-H. *J. Electrochem. Soc.* **2010**, *157* (1), A75.

(43) Piper, D. M.; Travis, J. J.; Young, M.; Son, S.-B.; Kim, S. C.; Oh, K. H.; George, S. M.; Ban, C.; Lee, S.-H. *Adv. Mater.* **2014**, *26* (10), 1596–1601.

(44) Han, X.; Gong, Y.; Fu, K.; He, X.; Hitz, G. T.; Dai, J.; Pearse, A.; Liu, B.; Wang, H.; Rubloff, G.; et al. *Nat. Mater.* **2016**, *16* (5), 572–579.

2. Surface Analysis Techniques

2.1 Introduction

This chapter describes the major techniques in this dissertation used to characterize the thin film materials of focus in the following chapters. Detailed descriptions of the parameters and methodologies for the instrumentation in each chapter are included within that chapter. The purpose of this chapter is to give a general overview of the underlying principles behind the most common thin film characterization techniques. Namely, this chapter will describe quartz crystal microbalance (QCM), spectroscopic ellipsometry (SE), X-ray reflectivity (XRR), X-ray diffraction (XRD) and X-ray photoelectron spectroscopy (XPS). These surface analysis techniques are used to measure material composition, film thickness, crystal structure, and surface roughness.

2.2 Quartz Crystal Microbalance

QCM is a technique that enables in situ mass change measurements during thin film deposition. This technique uses the resonant frequency of piezoelectric crystalline quartz to measure mass changes at its surface. The technique was first described as a means to measure mass changes due to a surface film by M. Onoe in 1957,[1] and was elucidated further as a quantitative technique by G. Sauerbray in 1959.[2] QCM can be

used to measure the relative mass changes as each half-reaction occurs at the crystal surface, depositing a thin film. In situ mass changes can reveal information on growth rates, reaction mechanisms, and film thicknesses. The ability to monitor in situ mass changes is invaluable in developing new ALD or MLD chemistries.

Quartz is a material with unique properties that enables its use as a microbalance. Quartz crystal is piezoelectric, where it can convert mechanical energy into electrical energy and vice versa. The most prevalent crystal structure of quartz and the type used in QCM is α-quartz, which has a trigonal crystal structure. The unit cell of this crystal structure is non-centrosymmetric and nonpolar at rest. Upon mechanical stress, there is a change in polarization in the crystal as molecular dipoles are re-oriented. This polarization creates an electric field between the crystal faces. This mechanism is called the piezoelectric effect. As its name suggests, the reverse-piezoelectric effect has a reversed mechanism, where an electric potential applied across a quartz crystal causes mechanical deformation. These effects can be used to induce oscillation of the crystal at a resonant frequency, generating a standing shear wave. The resonant frequency in quartz is exploited for several key applications today. For example, quartz is often used as the time-keeping mechanism within watches, where a small electric potential is applied to quartz to induce a resonant frequency oscillation that is then converted into one second beats with a tiny motorized circuit. The resonant frequency of quartz is also used to measure mass changes in QCM.

QCM measures precise mass changes by monitoring changes in its resonant frequency. Electrodes placed on either side of a quartz crystal are used to apply an alternating potential to the crystal, thereby causing resonant frequency oscillation. This resonant frequency is usually between 5 – 10 MHz and is dependent on the orientation of the crystal cut to the crystal axes. The typical crystal cut for QCM is AT. Molecules adsorbing to the surface of the crystal cause a decrease in resonant frequency. As more mass is added to the surface, the frequency shifts to lower values. Mass changes can be calculated with the Sauerbrey equation, as defined here:

$$\Delta f = -\frac{2f_0^2}{A\sqrt{\rho_q \mu_q}}\Delta m$$

Where f_0 is the resonant frequency (Hz), Δf is the frequency change (Hz), Δm is the mass change (g), A is the piezoelectrically active crystal area (cm^2), ρ_q is the density of quartz (2.648 g/cm^3), and μ_q is the shear modulus of quartz (for AT-cut crystal $\mu_q = 2.947 \times 10^{11}$ $g/(cm\ s^2)$. Because the changes in frequency are directly related to the mass of the adsorbed surface species, frequency changes can be used to calculate relative mass changes.

This powerful in situ analytical technique allows real-time data collection during thin film deposition. Shown in Figure 2.1 is a schematic of a typical ALD reactor with an in situ QCM installed. Indeed, QCM is sensitive enough to measure changes in mass down to 0.1 – 1 ng/cm^2, equivalent to single monolayer or sub-monolayer mass changes. With sub-monolayer sensitivity, QCM can be used to establish proposed mechanisms

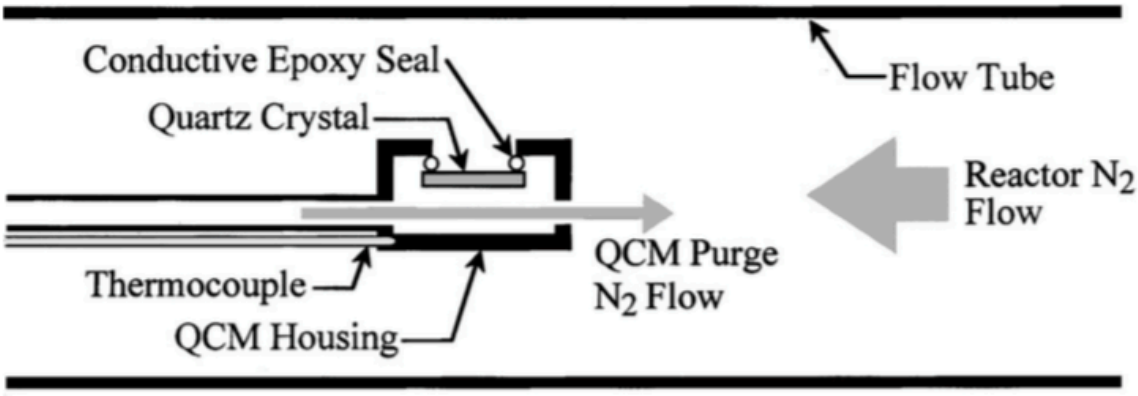

Figure 2.1 Cross-sectional schematic view of QCM and housing inside of an ALD reactor for in situ mass change measurements. *Reproduced from Elam, J. W.; Groner, M. D.; George, S. M. Rev. Sci. Instrum. 2002, 73 (8), 2981–2987.*

for surface reactions during thin film deposition. It can also be used to calculate a film thickness if the film density is known.

QCM is a powerful tool for monitoring very small mass changes in situ, but it does have some limitations. The high sensitivity of QCM is only possible when the adsorbing film is rigid. Viscoelasticity in the film causes the film and crystal oscillations to become decoupled, causing dissipation. As film thickness increases, these effects are exacerbated. Advanced technique for quantifying dissipative processes to calculate mass changes of viscoelastic films do exist, though they are outside the scope of this work. Besides viscoelastic damping effects, QCM is also very susceptible to temperature effects. AT-cut crystals are most often used for QCM because they are the least sensitive to temperature changes around room temperature. However, small changes in temperature can still be misinterpreted as mass changes. It is therefore extremely important to hold the temperature steady of the crystal steady when conducting QCM experiments. Finally, there is a limit to the amount of mass change that can be reliably detected with QCM. This upper limit of mass change is typically between 10-100 $\mu g/cm^2$.

2.3 Spectroscopic Ellipsometry

Spectroscopic ellipsometry (SE) is an optical instrumental technique primarily used to measure film thickness, roughness and refractive index. SE can also be used to

measure electrical conductivity, crystal quality and chemical composition of thin films. The technique was first demonstrated by Paul Drude in 1888, though the term was not coined until 1944.[3] SE measures film properties through the analysis of changes in polarization of a light source as it is reflected and refracted from a sample. Light incident to a sample surface is linearly polarized. Interactions with the sample change the phase and amplitude of the light and cause the reflected light to be elliptically polarized, as shown in Figure 2.2. The changes observed in the reflected light can be used to elucidate properties of the sample. This non-destructive technique is widely used to characterize thin films deposited with ALD and MLD.

SE measures changes in the amplitude (ψ) and phase difference (Δ) of light as it is reflected from an interface to gain sample information. Δ is defined as

$$\Delta = \delta_1 - \delta_2$$

where δ_1 is the phase difference between the parallel component and the perpendicular component of the incoming wave and δ_2 is the phase difference between the parallel component and the perpendicular component of the outgoing wave. ψ is defined as

$$\tan\psi = \frac{|R^p|}{|R^s|}$$

where $|R^p|$ and $|R^s|$ are the total reflection coefficients for multiple interfaces. These coefficients describe the ratios of the outgoing wave amplitude to the incoming wave amplitude for the components of light that are polarized to the plane of incidence (p)

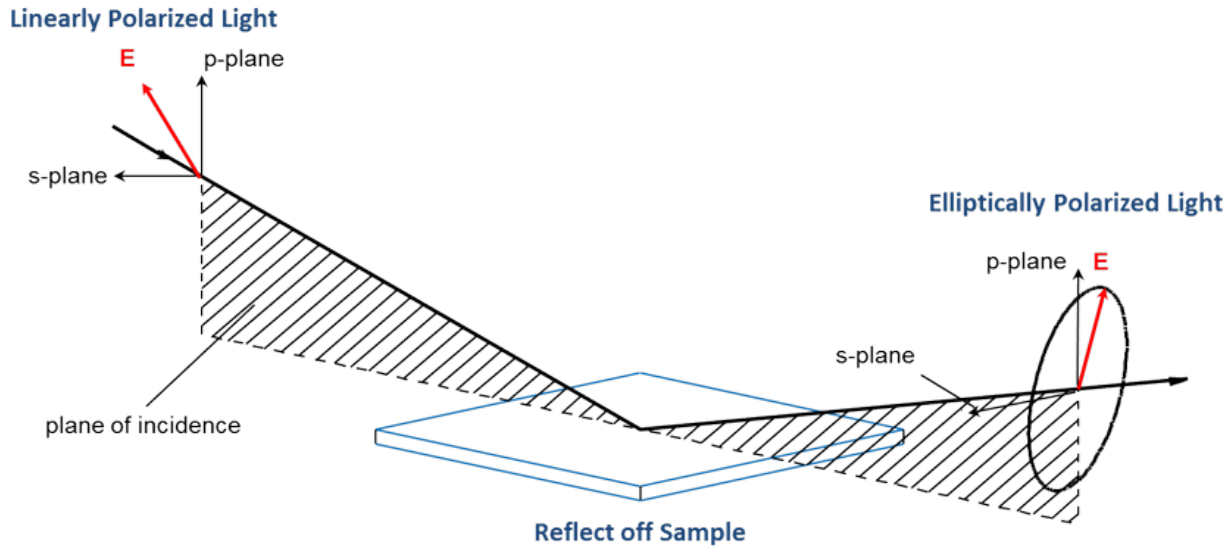

Figure 2.2 Depiction of the framework used for ellipsometry showing the relevant polarization planes. *Reproduced from "What is Ellipsometry?" - J.A. Woollam https://www.jawoollam.com/resources/ellipsometry-tutorial/what-is-ellipsometry (accessed Dec 22, 2019).*

and polarized perpendicular to the plane of incidence (s), respectively. The fundamental equation of ellipsometry is

$$\tan\psi\, e^{i\Delta} = \frac{R^p}{R^s}$$

where the total reflection coefficients are defined as

$$R^p = \frac{r_{12}^p + r_{23}^p \exp(-i\,2\beta)}{1 + r_{12}^p\, r_{23}^p \exp(-i\,2\beta)}$$

$$R^s = \frac{r_{12}^s + r_{23}^s \exp(-i\,2\beta)}{1 + r_{12}^s\, r_{23}^s \exp(-i\,2\beta)}$$

β is the film phase thickness and r values are the Fresnel reflection coefficients for a particular interface. β is defined as

$$\beta = 2\pi \left(\frac{d}{\lambda}\right) \tilde{N}_2 \cos\phi_2$$

where d is the film thickness, λ is the wavelength of light, Ñ is the complex index of refraction of the material being sampled and ϕ_2 is the angle of refraction in the material being sampled. The Fresnel coefficients are delineated by their superscripts, which define their planes of incidence, and their subscripts, which define their interfaces between two different material layers and air, as shown in Figure 2.3. Fresnel coefficients are defined as

$$r_{12}^p = \frac{\tilde{N}_2 \cos\phi_1 - \tilde{N}_1 \cos\phi_2}{\tilde{N}_2 \cos\phi_1 + \tilde{N}_1 \cos\phi_2}$$

$$r_{12}^s = \frac{\tilde{N}_2 \cos\phi_1 - \tilde{N}_1 \cos\phi_2}{\tilde{N}_2 \cos\phi_1 + \tilde{N}_1 \cos\phi_2}$$

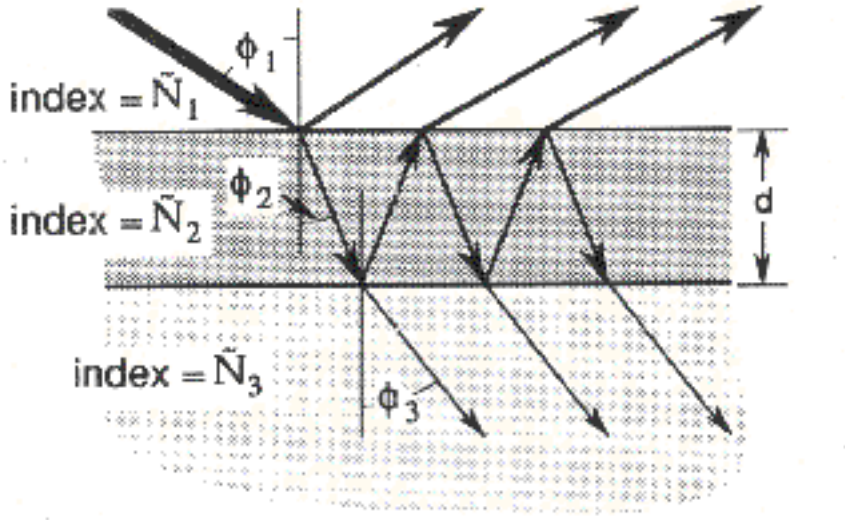

Figure 2.3 Depiction of the surface and interface upon which light interacts in ellipsometry. *Reproduced from Tompkins, H. G. A User's Guide to Ellipsometry; Elsevier, 1993.*

where $\tilde{N}$ is the complex index of refraction, ϕ_1 is the angle of incidence and ϕ_2 is the angle of refraction. $\tilde{N}$ is defined as

$$\tilde{N} = n - ik$$

where n is the index of refraction and k is the extinction coefficient. In dielectric materials, k = 0. Values of ϕ are described by Snell's law,

$$\tilde{N}_1 \sin \phi_1 = \tilde{N}_2 \sin \phi_2$$

Altogether, these terms and equations describe the behavior of light as it interacts with an interface and are used to determine the film thickness and refractive index of thin films with ellipsometry.

There are several benefits to using SE for thin film analysis. Because it is a non-destructive technique, it can be paired with a deposition reactor to measure in situ real-time film growth. SE is sensitive enough to measure film thicknesses in the sub-nanometer range and can also be used to measure multilayer films. Additionally, samples can be measured relatively quickly and easily.

SE techniques also have several limitations. One important limitation of this technique is that the spot size is relatively large, so samples must be several square millimeters in size for analysis. Additionally, substrates must be optically flat. Furthermore, SE is limited to measuring films with thicknesses up to the micron-scale, where interference oscillations become harder to resolve. Finally, absorbing films such as metals are further constrained to thicknesses up to ~100 nm.

2.4 X-Ray Diffraction and X-Ray Reflection

X-ray diffraction (XRD) and reflection (XRR) are nondestructive characterization techniques primarily used for measuring crystal structure and film thickness, respectively. Both of these techniques use a monochromatic X-ray source and are often coupled within the same instrument. Additionally, both techniques use photon interference phenomena for film analysis. In this work, a grazing-incidence configuration was used to target analysis of thin films. By orienting the incident beam so that it hits the sample at an angle close to the critical angle, the beam's optical path in the thin film is increased, and therefore allows for higher sensitivity. Grazing-incidence configurations are appropriate for measuring thin films in the range of 20 – 100 nm. Because these techniques are appropriate for measuring these thicknesses, and because of their ability to measure both structure and thickness, grazing incidence XRD and XRR are widely used analytical techniques for the study of ALD and MLD films.

XRD enables the measurement of the structural characteristics of thin films. It can elucidate crystallinity, crystal structure, crystal domain size, texture, and strain distortions within the crystal structure. Diffraction of a single crystal using X-rays was first discovered in 1912 by Paul Peter Ewald and Max von Laue.[4] However, it wasn't until 1979 that W. C. Marra, P. Eisenberger and A. Y. Cho invented grazing incidence XRD for surface and interface analysis.[5] Compared to electron diffraction, grazing

incidence XRD has better angle resolution and better accuracy, though a much larger sampling spot size and lower intensity.

The diffraction pattern that provides the basis for this technique is formed through constructive and destructive interference with the crystal structure of the thin film. Constructive interference occurs according to the Bragg equation:

$$2d \sin \theta = n\lambda$$

where d is the distance between atomic planes in the crystal, θ is the angle of the incident light in relation to the sample surface, n is a positive integer and λ is the wavelength of the incident light. As θ is scanned at a fixed wavelength, diffraction peaks occur when the Bragg condition is satisfied, according to Figure 2.4. The magnitude of d can be related to the miller indices and the unit cell lattice constants of the crystal structure. The diffraction peaks can be used to determine crystal structures because each mineral has a unique set of d-spacings. Variations in peak intensity from a reference spectrum may result from crystallites aligning in a particular orientation, also known as texture, from the size of the crystal grains, or from nonuniform strain. Crystal grain size can be determined from the line broadening of a peak using the Scherrer Equation:

$$\tau = \frac{K\lambda}{\beta \cos \theta}$$

where K is a shape factor, β is the full width of the peak at half of its maximum minus any inherent instrumental broadening, and τ is the crystallite size. Uniform strain

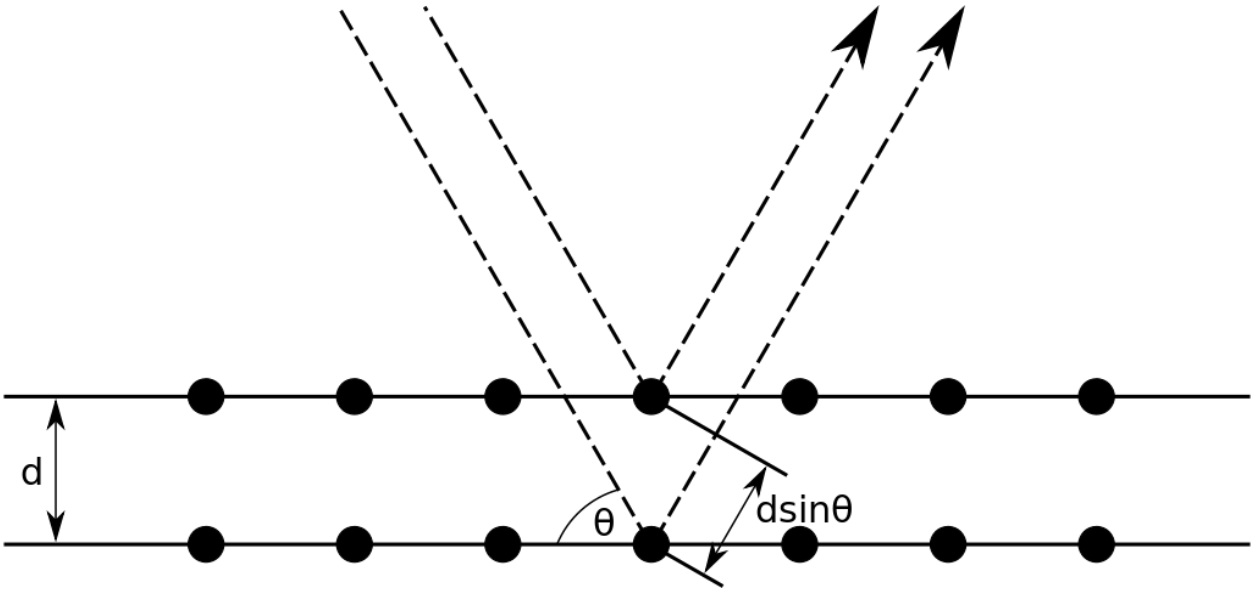

Figure 2.4 A representation of constructive interference satisfying the Bragg condition in a crystalline material.

distortions can be qualitatively measured by shifts in the d-spacing. XRR enables the measurement of film thickness, density, and interfacial roughness of single films or multilayers. XRR elucidates thin film properties by detecting specular reflections from flat surfaces as the angle of X-ray incidence is scanned across a small range of very grazing incident angles. This technique was first used for studying surface coatings in 1954 by Lyman G. Parratt for studying copper-coated glass.[6] Today it is widely used for characterizing thin films and is often considered more accurate than SE, which relies on modelling for analysis.

In its simplest form, XRR measures changes in the reflections of X-rays from interfaces due to interference. It then fits this data to determine film properties. In the X-ray region, the complex index of refraction (n) is often less than one. It is defined as

$$n = 1 - \delta - i\beta$$

where δ describes dispersion and β describes absorption. These values are usually in the range of 10^{-4} to 10^{-8} and are defined as

$$\delta = \frac{\rho_e r_e \lambda^2}{2\pi}$$

$$\beta = \frac{\mu\lambda}{4\pi}$$

where ρ_e is the electron density, λ is the wavelength of the X-ray, μ is the linear absorption coefficient for energies far from the X-ray region and r_e is the classical electron radius. The critical angle (θ_c) defined as

$$\theta_c = \sqrt{2\delta}$$

is defined as the angle below which all photons undergo total external reflection. Determination of the critical angle gives the mass density of the thin film. Above the critical angle (θ_c) some photons reflect at the surface and some refract into the thin film, reflecting at the second interface. Due to interference of reflections at multiple interfaces, oscillations known as Kiessig fringes are observed. Film thickness can be determined by comparing the angles of intensity maxima in relation to the critical angle and the wavelength of the X-ray, as follows

$$\theta_m^2 - \theta_c^2 = m^2 \frac{\lambda^2}{4d^2}$$

where m is the oscillation peak order and d is the film thickness. Plotting θ_m^2 vs m^2 gives a slope that can be used to estimate film thickness and an intercept equal to θ_c. The slope of the decay of oscillation with increasing m gives surface roughness.

Grazing incidence XRR and XRD are powerful tools that can be paired within the same instrument to characterize the key properties of thin films. However, both techniques also have several limitations. First, and likely most limiting, samples must be optically flat and have a roughness of less than 5 nm. Additionally, the spot size for these techniques is quite large, usually 2 to 5 mm. The sensitivity range of the instrument is typically between 0.1 and 1000 nm. Finally, for XRR analysis of multilayer films, a high contrast in electron density is needed for proper analysis. Despite these limitations, these techniques are widely used for their ease of use and are well suited to characterizing thin films deposited via ALD, MLD and other methods.

2.5 X-ray Photoelectron Spectroscopy

X-ray photoelectron spectroscopy (XPS) is a surface analysis technique for determining composition and chemical state of surfaces. The basic principle behind this technique is the photelectric effect, whereby electrons are emitted from a surface upon exposure to incident light. The photoelectric effect was first discovered by Heinrich Hertz in 1887. This effect was extended to surface analysis by Kai Siegbahn and others in 1967,[7] for which he was one of the winners of the Nobel prize in physics in 1981. XPS uses a monochromatic X-ray source to emit photoelectrons with kinetic energies that are distinct to the elements from which they came. This technique is a powerful tool for determining the electronic structures of surfaces.

There are three steps to photoelectron emission that help define XPS. Step one is the optical excitation of a photoelectron. The photon energy for XPS is typically around 1000 eV, most often from a Mg K-alpha or Al K-alpha source, with 1254 and 1487 eV, respectively. In comparison to ultraviolet photoelectron spectroscopy (UPS), the low energy photons of XPS sample photoelectrons from deep core states of atoms. The second step of photoelectron emission is transport of the photoelectron to the surface. Also called the electron escape depth, the electron mean free path determines how far an electron with a given kinetic energy will travel prior to undergoing an inelastic collision within a solid material. The mean free path is typically between 0.3 and 3 nm and is dependent on the element. This value also determines the practical sampling

depth limit for non-destructive analysis. The third step of photoelectron emission is escape to vacuum. This step is dependent on the work function, the minimal amount of thermodynamic work required to remove an electron from a solid to vacuum. Altogether, photoemitted electrons are emitted with a kinetic energy (E_K) dependent on the incident photon energy ($h\nu$), the binding energy of the electron (E_B), and the work function (ϕ), as follows

$$E_K = h\nu - E_B - \phi$$

XPS detects E_K of photoemitted electrons to determine E_B values, which are distinct for each element. Relative intensities are also detected, as they are directly related to the concentration of that element in the sample. XPS spectra can be used to elucidate the occupied density of states. To that end, oxidation states can be determined by measuring peak shifts due to small changes in binding energies. Therefore, XPS can measure what elements are present in a sample, their concentrations and what their oxidation states are.

XPS has benefits and limitations that define its range of use. It can detect elemental composition down to 0.01 – 0.1 atomic percent and has a small spot size of 1 – 10 μm. It can be used as a non-destructive technique for analysis at a depth of up to 8-10 nm into the sample and can be paired with ion sputtering for further depth profiling. Drawbacks include the need for ultrahigh vacuum, and the possibility of skewing of quantitative results due to preferential sputtering or charging effects. Additionally, XPS

is not well suited for characterization of organic samples, and it cannot detect hydrogen or helium. Despite these limitations, XPS is well-suited for the characterization of thin films and was widely used in the following chapters.

2.6 References

(1) Onoe, M. *Proceddings Inst. Radio Eng.* **1957**, *45* (5), 694.

(2) Sauerbrey, G. *Zeitschrift für Phys.* **1959**, *155* (2), 206–222.

(3) Collins, R. W.; Kim, Y. *Anal. Chem.* **1990**, *62* (17), 887–890.

(4) Bethe, H. E.; Hildebrandt, G. *Biogr. Mem. Fellows R. Soc.* **1988**, *34*, 134–176.

(5) Marra, W. C.; Eisenberger, P.; Cho, A. Y. *J. Appl. Phys.* **1979**, *50* (11), 6927–6933.

(6) Parratt, L. G. *Phys. Rev.* **1954**, *95* (2), 359–369.

(7) Siegbahn, K.; Nordling, C.; Fahlman, A.; Nordberg, R.; Hamrin, K.; Hedman, J.; Johansson, G.; Bergmark, T.; Karlsson, S.-E.; Lindgren, I.; Lindgren, B. *Nov. acta Regiae Soc. Sci. Ups. Ser. IV* **1967**, *20*.

3. Structural Enhancement of a Silicon Anode by Ultrathin Polyamide Coating for High Energy Lithium-Ion Batteries

Jasmine M. Wallas,[1] Brian C. Welch,[2] Yikai Wang,[3] Simon E. Hafner,[2,4] Jun Liu,[4]

Taeho Yoon,[4] Yang-Tse Cheng,[3] Steven M. George,[1] Chunmei Ban[4]

[1]Department of Chemistry, University of Colorado, Boulder, Colorado 80309

[2]Department of Mechanical Engineering, University of Colorado, Boulder, Colorado 80309

[3]Department of Chemical and Materials Engineering, University of Kentucky, Lexington, Kentucky 40506

[4]National Renewable Energy Laboratory, Golden, Colorado 80401

3.1 Introduction

There is an ever-increasing demand for higher power lithium-ion batteries. This demand has fueled research into higher energy density electrode materials, such as silicon. Silicon is a high energy density, low cost anode material. Compared to the conventional graphite anode used in lithium-ion batteries (372 mAh g^{-1}), silicon has an almost tenfold higher theoretical energy density (3579 mAh g^{-1}). However, silicon suffers from a ~ 300 % volume expansion upon lithiation and an unstable solid-electrolyte interphase (SEI), leading to poor galvanostatic cycling stability. Because of silicon's favorable properties, much recent research has focused on addressing its inherent cycling instability.

One strategy to mitigate the detrimental effects of volume expansion uses functional polymer binders that can enhance the mechanical integrity of the electrode.

Polyvinylidene fluoride (PVDF) is the conventional polymer binder used in these electrodes. However, this binder is unable to accommodate the large volume changes in a silicon anode upon cycling. Recent work has identified alternative binders such as carboxymethyl cellulose (CMC) and polyacrylic acid (PAA) that improve electrochemical performance. [1,2] The -OH and -COOH groups in these two binders interact favorably with the silicon surface.[3–5] That said, additional improvements to these alternative binders are necessary. PAA undergoes a reduction reaction to form an anhydride at elevated temperatures.[6–8] In vacuum, this reaction begins at ~ 150 ˚C.[6] In the presence of lithium-ion battery electrolyte, this reaction begins ~ 55 ˚C, where the reaction is catalyzed by the decomposition products of $LiPF_6$.[7] The formation of the anhydride is a source of concern in this system because it causes poor mechanical properties and poor electrochemical cycling.[7,8]

Another strategy to enhance the mechanical integrity of the silicon anode uses surface coatings. Much research has focused on hybrid organic-inorganic coatings deposited with molecular layer deposition (MLD). These aluminum alkoxide or "alucone" coatings are flexible, mechanically robust, and improve the cycling stability of a silicon anode.[9,10] However, there are concerns that these coatings can react with Li^+ causing Li^+ depletion in the cell.[11] There is also concern that conventional MLD is a time-consuming and difficult process and the low vapor pressure of the organic precursors can create challenges.

In order to address issues that arose from previous efforts to stabilize Si with MLD, we used an all-organic aromatic polyamide coating material. Aromatic polyamides are known for their excellent chemical and thermal stability, so they are suitable for the harsh, corrosive environment of a battery cell.[12] Additionally, aromatic polyamides have high tensile strength and wear resistance.[13] Polyamides have been used in lithium-ion batteries as cathode coatings,[14] binders,[15] and separators.[16] The polyamide coating was able to restore favorable mechanical properties in the silicon electrode that are lost when PAA degrades. The coating was deposited using a spatial MLD design. In spatial MLD, the substrate moves between zones where each precursor is continuously dosed, and precursors are separated by space. Using a spatial design, we reduced MLD deposition time from several hours to minutes. By using an all-organic polyamide material and depositing it using a spatial design, we were able to bring silicon anode technology closer to viability.

3.2 Experimental Methods

3.2A Electrode Fabrication

Silicon composite anodes were prepared via slurry casting of Si (Alfa Aesar, plasma synthesized, ≤ 50 nm), carbon black (Super P®, Timcal), and PAA (M_v ~ 450,000, Sigma Aldrich) with a weight ratio of 60, 20, and 20 % respectively, in 1-methyl-2-pyrrolidinone (NMP) (anhydrous, 99.5 %, Sigma Aldrich). The mixture was coated onto

copper foil and dried at 70 ˚C in air. Electrode sheets were either used as is, heat treated at 150 ˚C, or heat treated at 150 ˚C and coated with an MLD film. Electrodes were punched to 14 mm diameter and dried at 95 ˚C overnight in a vacuum oven prior to coin cell assembly.

3.2B MLD Coating

MLD was used to deposit thin film coatings on silicon anodes. Deposition was performed in a custom-built spatial MLD system enclosed within a convection oven. The operation[17] and design[18] of this rotary drum system were previously described. The nitrogen purge gas (99.998 %, Airgas) separating precursor dosing zones was flowed at 1000 sccm. The convection oven encasing the entire system allowed uniform heating to the targeted deposition temperature of 150 ˚C. Once loaded into the reactor, samples were heated overnight at the deposition temperature to reach thermal equilibrium with the system. Anode samples were mounted to the inner drum of the spatial MLD system using Kapton adhesive tape. Tape was applied to all sides of the anode samples to seal the backside and prevent deposition on the foil side of the samples. For thicknesses measurements, a reflective and flexible witness sample was added to each deposition. The witness was a PEN polymer film (75 μm thick) metalized with titanium (sputtered, 80nm thick (ROWO Coating). Precursors for two separate MLD chemistries were mounted onto the system. One set of precursors was trimethylaluminum (TMA) (97 %, Sigma Aldrich) and glycerol (99.5 % Sigma-Aldrich) to produce a hybrid organic-

inorganic aluminum alkoxide (alucone). The other set of precursors was m-phenylenediamine (mPD) (99 %, Sigma Aldrich) and trimesoyl chloride (TMC) (98 % Sigma-Aldrich) to produce an all-organic aromatic polyamide. The TMA resided outside the oven enclosure at room temperature and the other precursors resided within the convection oven of the system. Each precursor was connected to the system by two bellows globe valves on either side of bellows needle valve for metering flow. Precursor exposure time was defined by the rotation speed of the inner drum upon which the samples resided as it moved through precursor dosing zones. The two rotation speeds used in this work, 0.5 rpm and 5 rpm, correspond to exposure times of 6 and 0.6 seconds.[19] MLD film thickness was measured on the witness PEN sample with spectroscopic ellipsometry (SE) (M-2000, J. A. Woollam Co, Inc.) SE measurements were performed over a spectral range of 240 nm to 1685 nm with a 50, 60 and 70° incident angles. Data was modeled with CompleteEASE v.4.55 (J. A. Woollam Co., Inc.). A Cauchy model was used to measure alucone films. Polyamide films were modelled with two Gaussian oscillator curves with an anisotropic index difference in the z-axis.

3.2C Electrochemical Cycling

Standard 2032 half-coin cells with Li metal foil as counter and reference electrode were used. Cells were assembled in an Ar-filled glovebox. The electrolyte was 1.5 M $LiPF_6$ in ethylene carbonate, diethyl carbonate and fluorethylene carbonate at a weight ratio of 5, 70, and 25 % respectively. The separator was Celgard. Electrochemical tests

were conducted at room temperature using an Arbin 2000 and a Maccor 4000 battery test station. For each condition, cycling data was plotted as an average of three cells with standard errors.

3.2D Fourier Transform Infrared Spectroscopy (FTIR)

Attenuated total reflectance (ATR) FTIR (Nicolet 6700, Thermo Scientific) spectra were collected with a liquid nitrogen cooled MCT/A detector. Spectra were averaged over 200 scans with a scan resolution of ~ 1 cm^{-1}. MLD films for analysis were deposited on copper foil.

3.2E Mechanical Testing

Nanoindentation tests were conducted by using a Nanoindenter G200 (Agilent) inside an argon-filled glovebox. A depth-controlled mode was used with an indentation strain rate of 0.05 s^{-1}, a maximum depth of 1200 nm, and a 10 second hold at the maximum depth. Because the maximum depth was less than one tenth of the total electrode thickness, the substrate effect can be neglected. Before nanoindentation tests, thermal drift was calibrated to be less than 0.5 nm s^{-1}. Thermal drift calibrations (100 seconds) were conducted after unloading. The elastic modulus and hardness were determined based on the Oliver-Pharr method.[20] Nanoindentation tests under wet conditions were carried out with a liquid cell. The technical details of nanoindentation measurements under wet conditions were previously described.[21] During the test, the indenter was immersed in the electrolyte. Therefore, the surface tension of the

electrolyte does not influence the nanoindentation result. Electrolyte was replaced every 40 minutes to avoid any precipitation of ethylene carbonate and $LiPF_6$ that might influence measurements. Reported values are averages from at least ten measurements and error bars are standard deviations.

Scratch tests were conducted with a conical indenter (cone angle 60° and tip radius 5 μm) using a NanoTest Vantage system (Micro Materials, U.K.). A pre-scan was conducted with a constant load of 0.1 mN to probe the roughness of the scratch trace and calibrate scratch depth profiles. During scratch tests, a normal load was applied after 50 μm scanning (at the load of 0.1 mN) with a loading rate of 0.5 mN/s. The maximum load (F_{max}), scratch distance, and the scanning veolocity are 120 mN, 3000 μm, and 10 μm /s, respectively. The scratch continued with F_{max} after it reached a distance of 2450 μm. We conducted 5 scratch tests for each sample to guarantee the reproducibility of the results.

3.2F STEM-EDS

TEM samples were prepared with a scratching method, *i.e.*, using the Cu TEM grid to scratch the electrode. TEM observations were performed on an FEI Tecnai F20 TEM equipped with energy-dispersive X-ray spectrometry (EDS) at an acceleration voltage of 200 kV. For the cycled electrode, TEM sample preparation and TEM sample loading were conducted in an Ar-filled glovebox. A Gatan-vaccum-transfer TEM holder was used to avoid moisture and air during the sample transfer.

3.3 Results and Discussion

The reduction of PAA is a well-known reaction that occurs at elevated temperatures. Reduction occurs when carboxylic acid groups in the polymer undergo a condensation reaction to form polyacrylic anhydride and release H_2O, according to the following reaction:

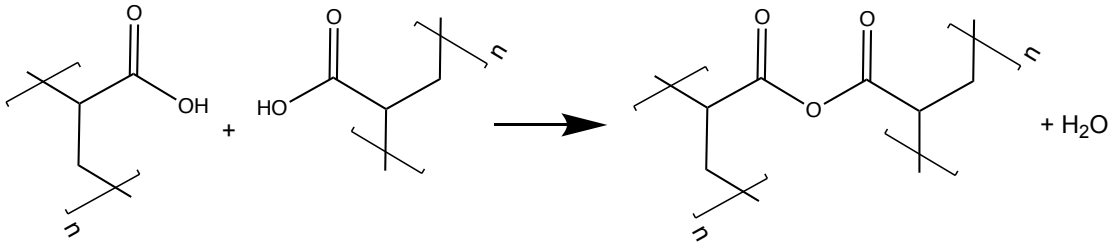

In LIB electrodes, the PAA binder can react form this anhydride, negatively affecting battery performance.[7,8] This reaction reduces the number of carboxylic acid groups that can interact favorably with the hydroxyl groups on the silicon surface, and thereby decreases electrode adhesion forces. A decrease in electrode adhesion can lead to the electrochemical isolation of silicon, causing capacity fade. The anhydride reaction also causes polymer cross-linking, which decreases the elasticity of the binder and may reduce volume expansion compatibility. Additionally, the water released upon anhydride formation can react with the electrolyte to form HF.

Though this reaction usually occurs at elevated temperatures, it can also be catalyzed at lower temperatures by the decomposition products of battery electrolyte. Under vacuum this reaction occurs at temperatures ≥ 100˚C.[6] However, when immersed in battery electrolyte, this reaction can occur at temperatures as low as 55 ˚C.[7] The formation of the anhydride can be monitored with FTIR. Figure 3.1 shows FTIR spectra of silicon composite electrodes, composed of silicon nanoparticles, PAA and carbon black, dried under vacuum at different temperatures. Bands at ~1710 and ~1410 cm^{-1} indicate free carboxylic acid groups and bands ~1618 and 1455 cm^{-1} indicate hydrogen bonded carboxylic dimers, all of which are characteristic of PAA. These peaks are prominent in the electrodes dried at 70 and 95 ˚C, and diminished in the electrode dried at 150 ˚C. In the electrode dried at 150 ˚C, the carboxylic anhydride peak is prominent, indicated by peaks at ~1800 and ~1012 cm^{-1}. Compared to electrodes dried at 90 ˚C, electrodes dried at 150 ˚C show reduced galvanostatic cycling performance. Tests comparing cycling of electrodes after drying at 95 and 150 ˚C are shown in Figure 3.2.

In this work, a thin aromatic polyamide coating was used to enhance the structural integrity of the silicon composite electrode and counteract the negative effects of anhydride formation. The MLD coating was deposited via sequential, self-limiting surface reactions with the precursors m-phenylenediamine (mPD) and trimesoyl chloride (TMC). A spatial MLD reactor design was used in these depositions. A detailed report on the spatial reactor used in these depositions was previously reported.[17] The

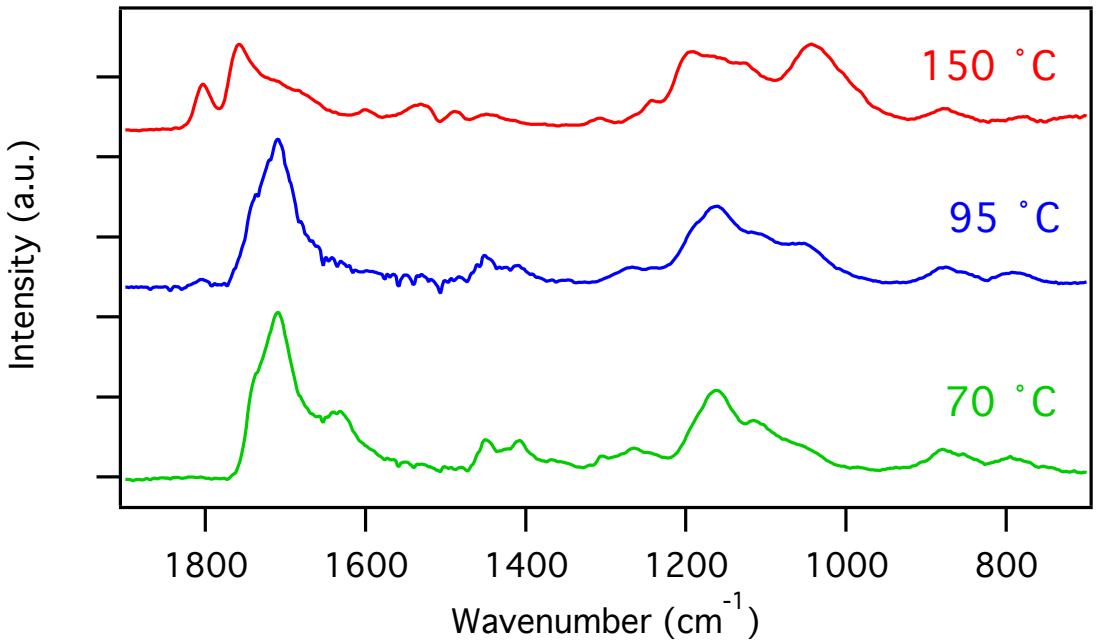

Figure 3.1 FTIR spectra indicating the temperature evolution of PAA in a silicon composite electrode. PAA is indicated by the peaks at 1710, 1618 and 1455 cm-1. Polyacrylic anhydride, indicated by peaks at 1800 and 1012 cm-1, is present when heated to 150 ˚C.

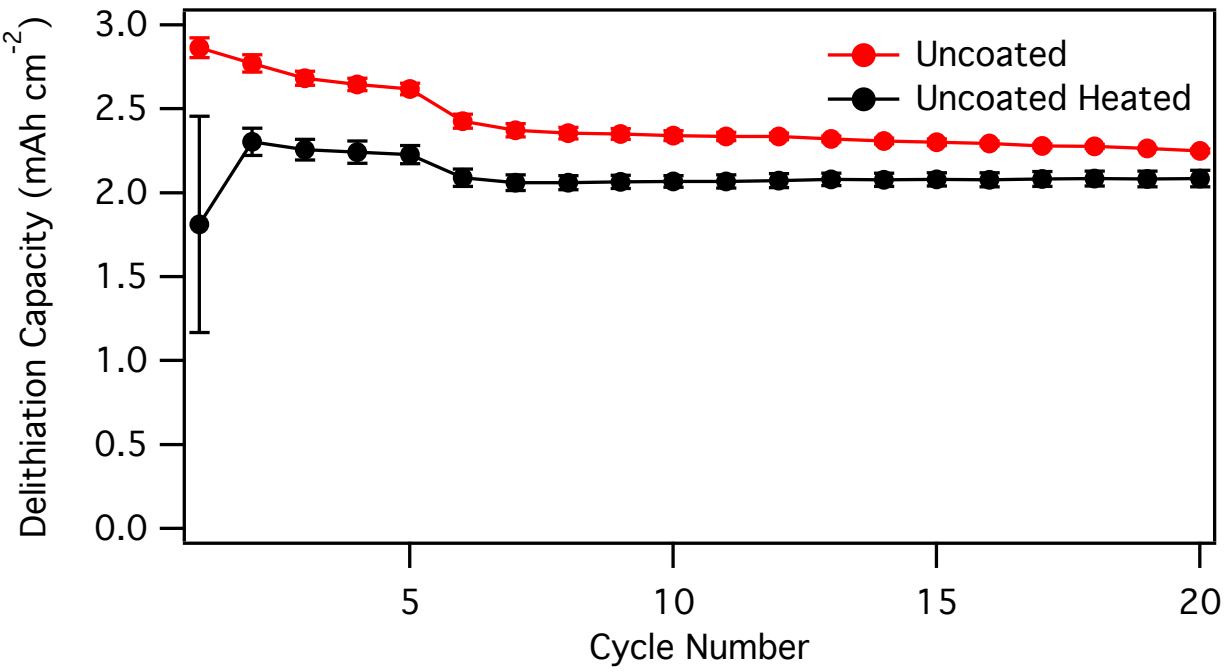

Figure 3.2 Electrochemical cycling of uncoated electrodes after drying at 95 and 150 ˚C. The first five cycles used a 0.04 C rate and the following cycles used a 0.1 C rate. The voltage was cycled between 0.010 and 1.000 V vs Li/Li+.

coating was deposited directly onto the as-prepared electrodes. Because of the nanoscale features and high aspect ratio in the electrodes, long precursor exposure times were needed to deposit a conformal coating.[19,22] Long exposure times present a challenge in the design of spatial ALD or MLD reactors. Approximate precursor exposure times in this system were studied using the well-known MLD chemistry, alucone, deposited with the precursors trimethylaluminum and glycerol. A description of galvanostatic cycling of alucone coated electrodes deposited with different exposure times is included in the SI (Figure 3.3). Those tests indicated that the best electrochemical performance was realized with the longest exposure times studied, 6 seconds. The best polyamide MLD coating, with a thickness of 0.5 nm, was deposited with 6 second exposure times.

The polyamide MLD coating has some favorable properties as a silicon electrode coating. Aromatic polyamides are generally considered chemically stable. To illustrate, a 380 nm MLD coating on Cu was soaked in electrolyte for 24 hours. After soaking, the coating appeared unchanged. No significant mass change was observed after soaking. A large mass increase in the coating would be expected if it were to react strongly with Li^+. Indeed, the FTIR spectra of this sample remained unchanged after soaking, suggesting that there was no appreciable chemical change in the material (Figure 3.4). Aromatic polyamides are also generally considered insoluble in organic solvents. The insolubility of the MLD coating increases the structural integrity of the electrode when immersed in

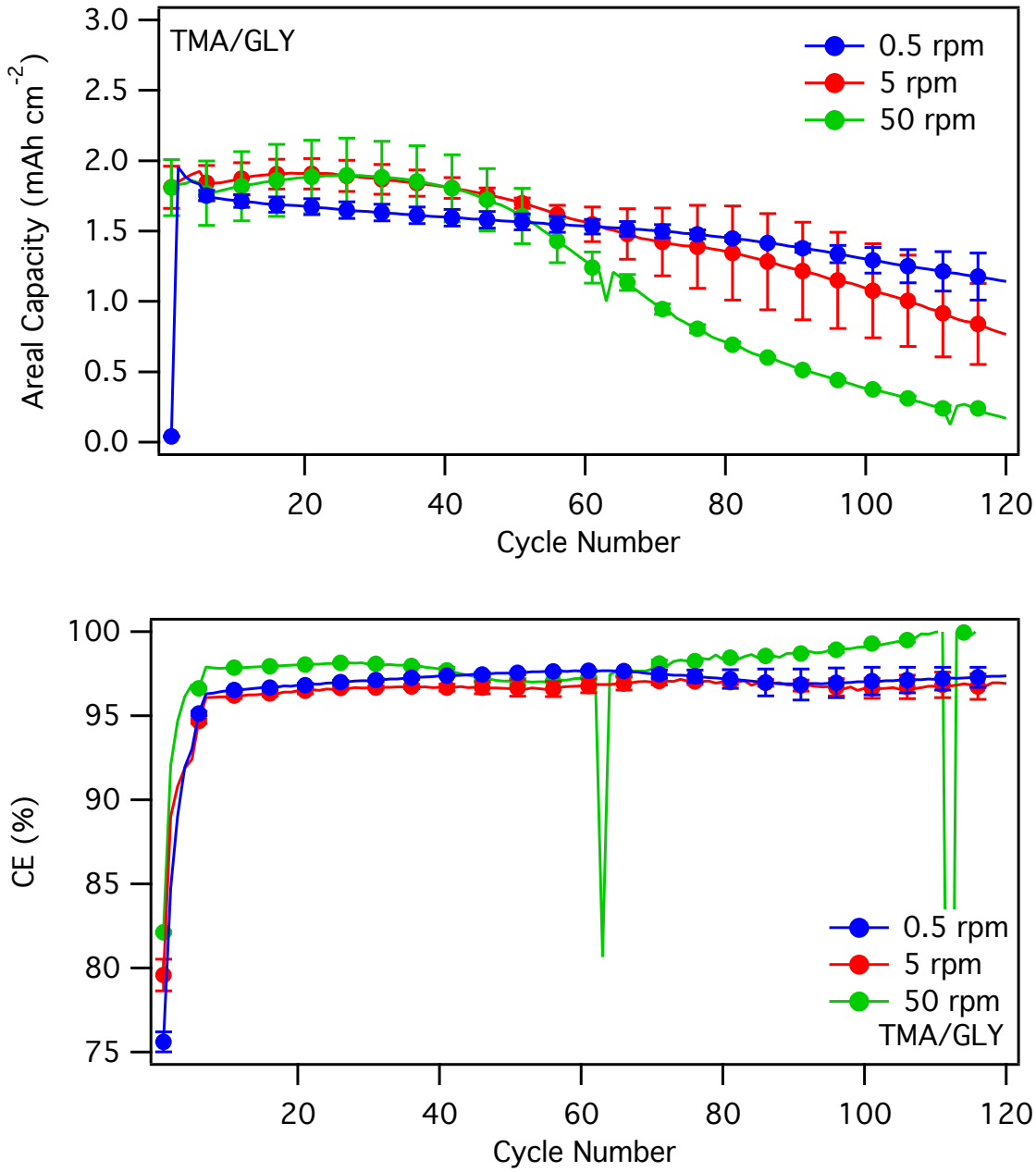

Figure 3.3 Electrochemical cycling of silicon composite electrodes with 10 nm alucone coatings deposited with three different precursor exposure times: 0.06, 0.6 and 6 s via spatial MLD. Capacity retention is extended with longer exposure times.

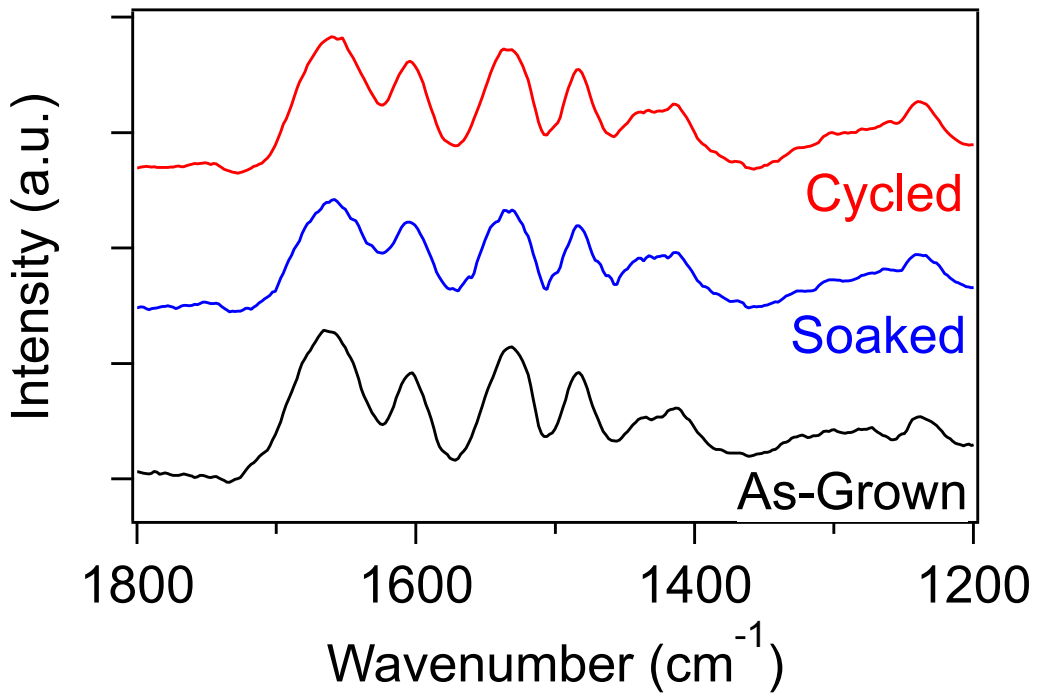

Figure 3.4 FTIR spectra of an as-grown 353 nm polyamide MLD coating on Cu, the same coating after soaking in electrolyte for 24 hours, and the same coating after five galvanostatic discharge charge cycles at 10 μA.

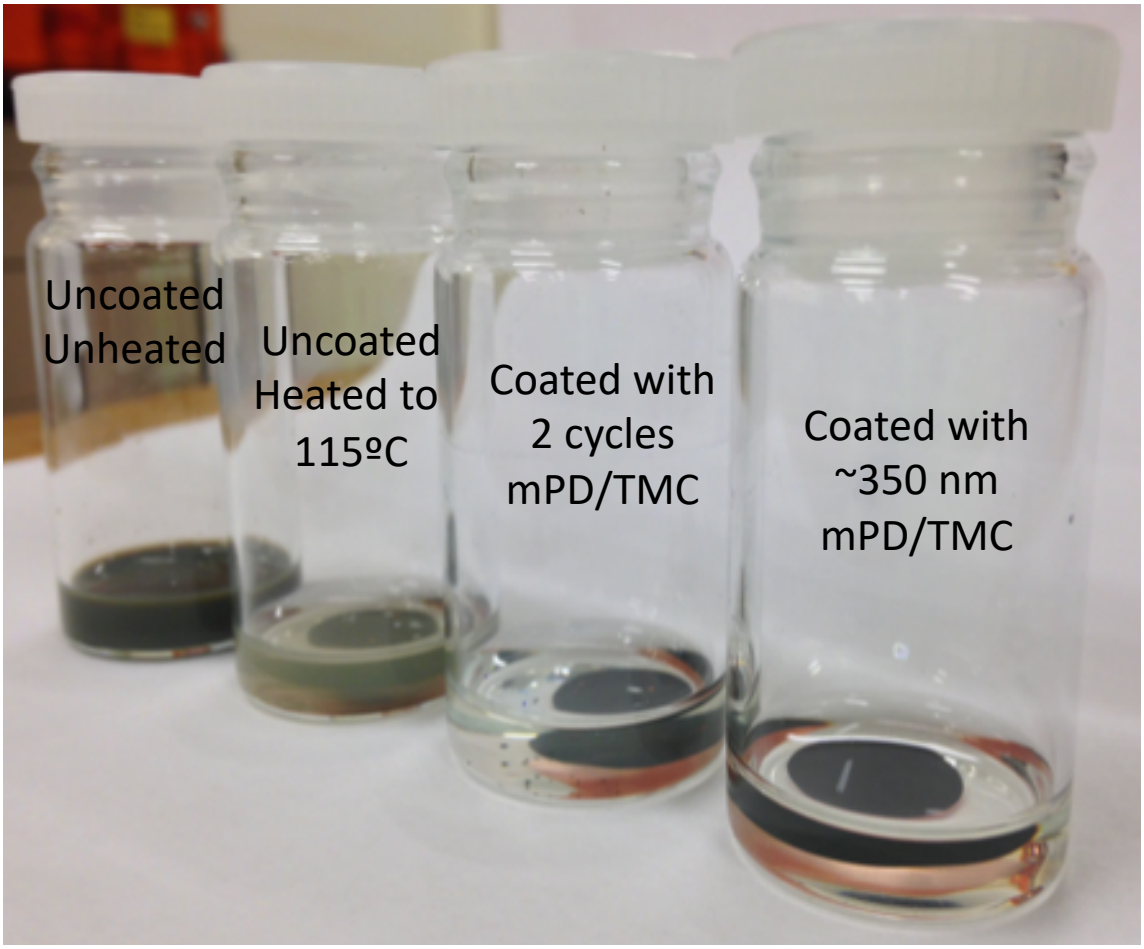

Figure 3.5 Electrodes immersed in NMP solvent for two days and then sonicated. The pristine electrode dissolves, an uncoated electrode heated to 115 ˚C partially dissolves, and electrodes coated with 0.5 nm or 353 nm of polyamide shows little to no dissolution.

organic solvent. Figure 3.5 shows electrodes soaked in NMP solvent for 48 hours, then sonicated for 2 minutes. The pristine electrode completely dissolved in the solvent. The electrode that was dried at 150 ˚C, and therefore contained polyacrylic anhydride, had some solubility in the solvent. In comparison, an electrode coated with 0.5 nm of MLD appeared the most stable and was largely insoluble.

Polyamides also have favorable mechanical properties. Mechanical testing, shown in Figure 3.6, indicates that some of the negative effects of anhydride formation can be mitigated by coating the electrode with a very thin MLD coating. Nanoindentation tests, shown in Figure 3.6A, were performed on electrodes in wet conditions, soaked in electrolyte to better mimic mechanical properties within the battery.[21] Compared to an electrode dried at 70 ˚C, an electrode dried at 150 ˚C had a lower elastic modulus and higher hardness. The elastic modulus was reduced by 62 %, from 2.28 ± 0.47 to 1.42 ± 0.29. The MLD coating increased the elastic modulus of the electrode dried at 150 ˚C by 345 %, to 4.90 ± 1.01. The coating also increased the hardness by 50 %, from 0.08 ± 0.01 to 0.12 ± 0.03. The improved mechanical properties likely contribute to the improved electrochemical cycling stability of the MLD-coated electrodes described below.

We conducted scratch tests on the electrodes to investigate the influence of the MLD coating on the mechanical integrity of Si electrodes. As shown in Figure 3.6B, the

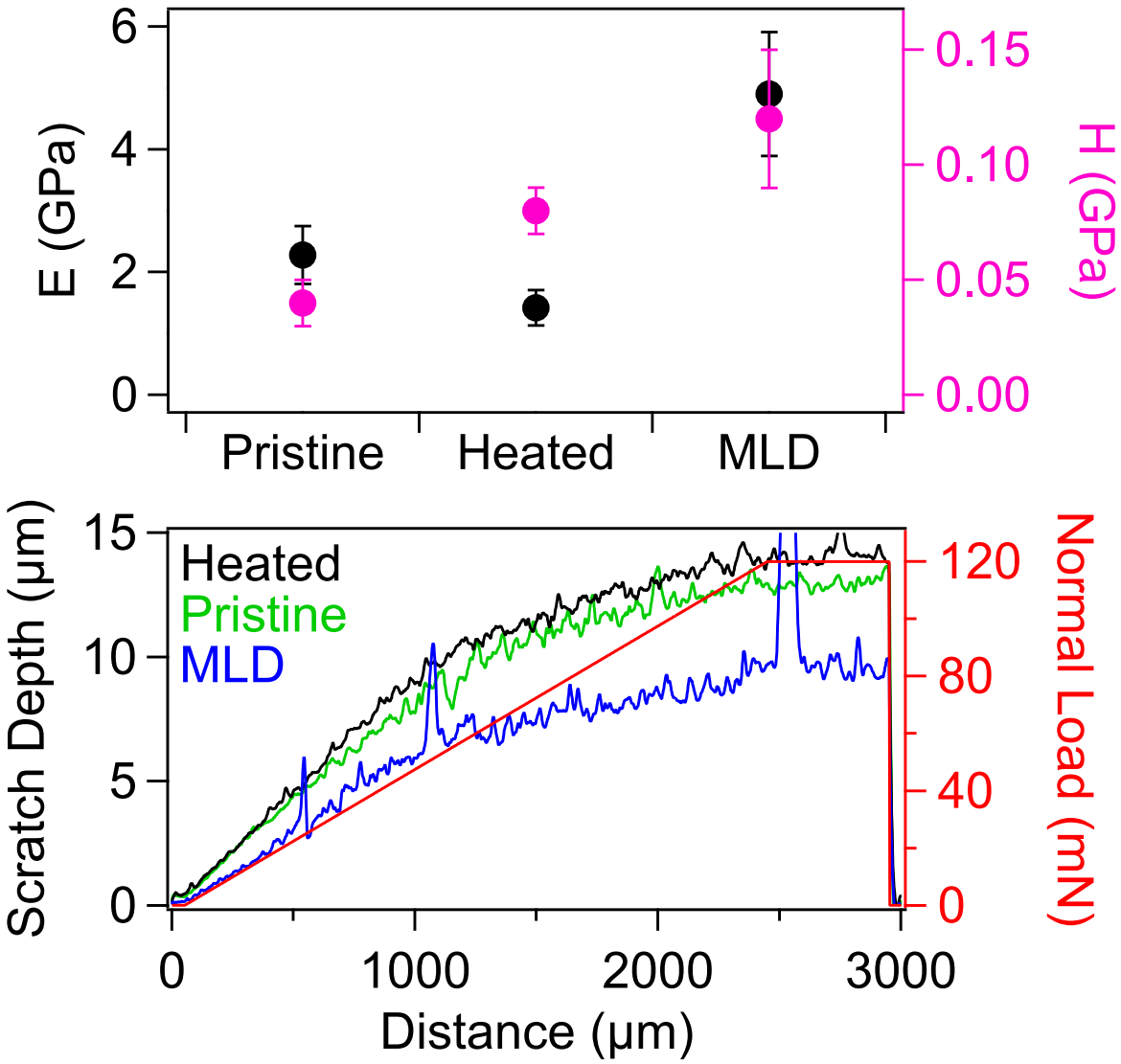

Figure 3.6 Mechanical testing of silicon composite electrodes. A) Elastic modulus and hardness values from nanoindentation of electrodes soaked in electrolyte. B) Scratch testing indicates increased adhesion within the electrode when coated with polyamide.

MLD coated electrode had a smaller scratch depth and scratch width under the same normal load and distance as compared to the uncoated electrode. The scratch resistance of the MLD coated electrode indicates that it has a larger load-bearing capacity than the uncoated electrode. A considerable amount of the uncoated electrode delaminated over the length of the scratch, while the MLD-coated electrode had less delamination (Figure 3.7). Based on these results, it is reasonable to infer that MLD strengthens and improves the cohesion of the composite electrodes. Improved adhesion inhibits the mechanical degradation of Si electrodes during electrochemical cycling.

Enhancement in electrochemical performance of polyamide MLD-coated silicon anodes was probed with galvanostatic cycling, as shown in Figure 3.8. Tests were conducted using a half-cell configuration with lithium metal as the counter and reference electrode. All electrodes were heated at 150 ˚C overnight and therefore contained polyacrylic anhydride. Electrochemical cycling performance of an uncoated, pristine electrode was compared with MLD-coated electrodes with three different coating thicknesses. The three MLD coating thicknesses were 0.5, 3 and 15 nm, as measured with spectroscopic ellipsometry on Ti-coated PEN witness samples that were included in each deposition. Note that the 3 and 15 nm coatings were deposited with a 0.6 second exposure time, while the 0.5 nm coating was deposited with a 6 second exposure time. The coatings deposited with shorter exposure times may be less conformal than those deposited with longer exposure times. For the first five cycles,

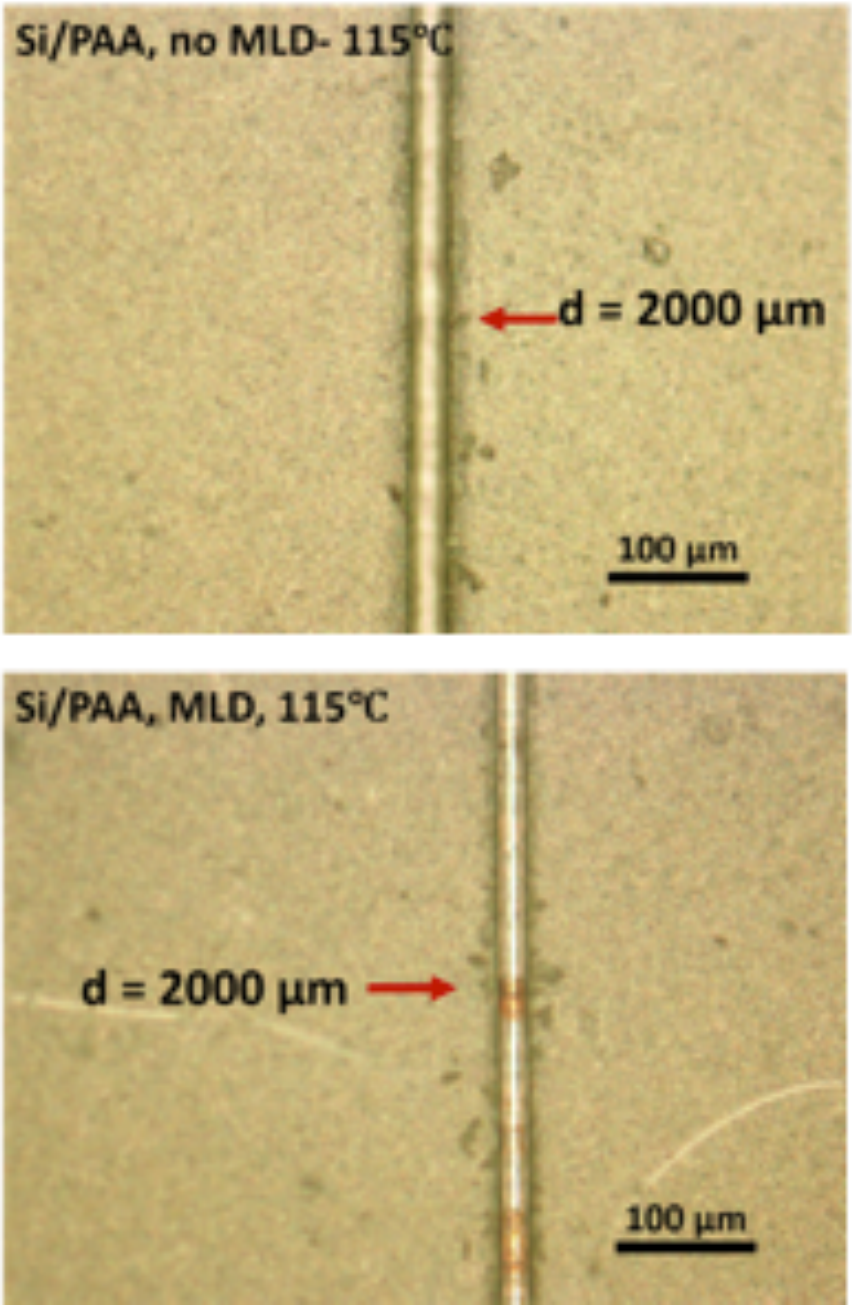

Figure 3.7 Scratch tests of A) a pristine electrode heated to 115 ˚C and B) an electrode with a 0.5 nm polyamide coating deposited at 115 ˚C.

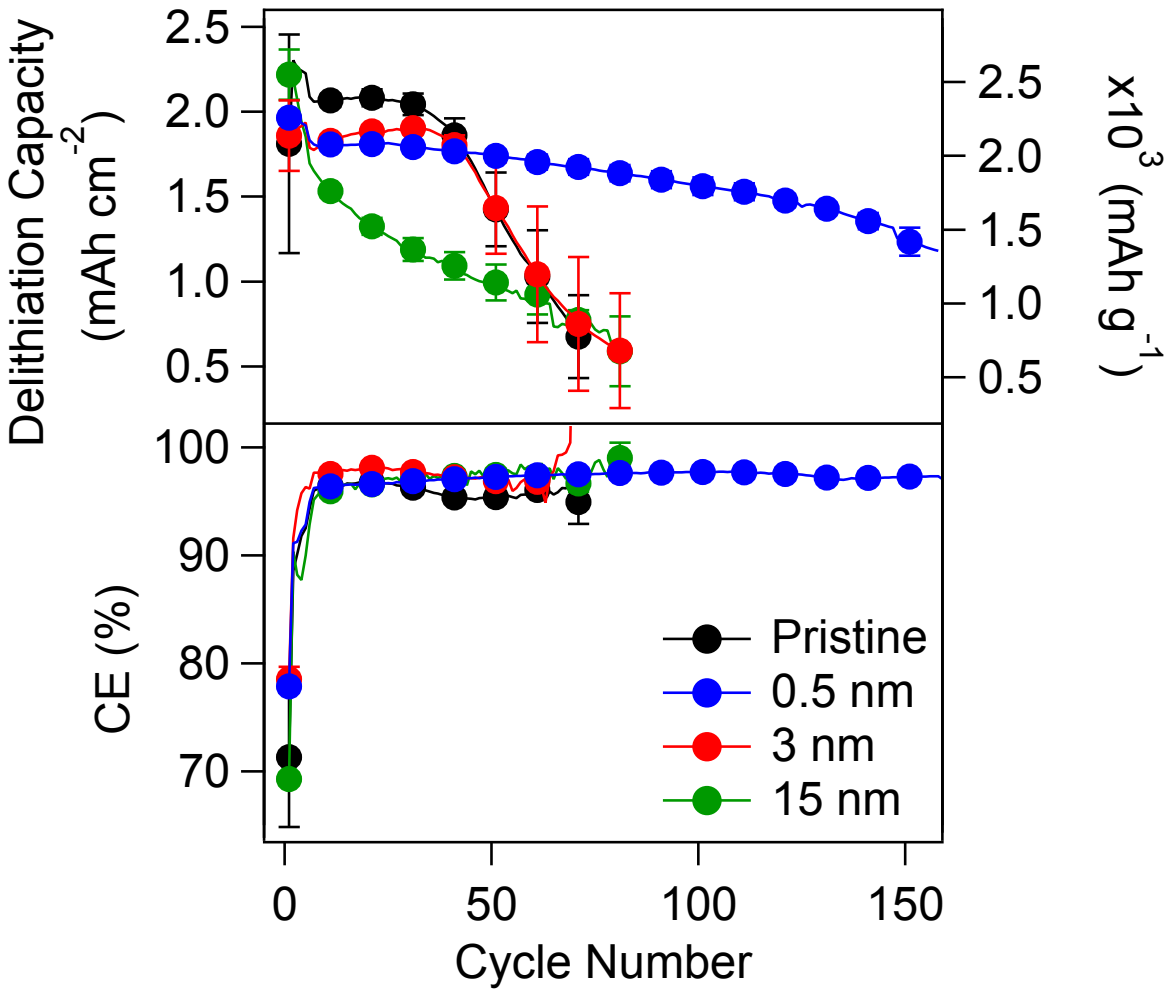

Figure 3.8 Electrochemical cycling of pristine silicon composite electrodes compared to those coated with 0.5, 3, and 15 nm of polyamide. Capacity retention is extended with a thin 0.5 nm polyamide coating and reduced with a thick 15 nm polyamide coating.

current was drive at a C/25 rate (143 mA/g), and the following cycles used a C/10 rate (358 mA/g). Electrodes were cycled between 0.010 and 1.000 V against a lithium-metal counter electrode, with a 10-minute voltage hold at 0.010 V and a 30-minute voltage hold at 1.000V.

Galvanostatic cycling indicated a marked increase in performance when the electrode was coated with 0.5 nm of MLD. The pristine electrodes cycled stably until cycle ~ 50, after which there was rapid capacity fade. The electrodes coated with 3 nm of MLD showed similar cycling behavior to the uncoated electrode. The electrodes coated with 15 nm of MLD showed steady capacity fade beginning in the initial cycles. The electrodes coated with 0.5 nm of MLD demonstrate stable cycling for 158 cycles, with a capacity > 1300 mAh/g. Between cycles 6 and 100, these cells cycled stably at ~ 1.6 mAh cm^{-2}. At cycle 100, these cells retained 80 % of their initial average capacity. The electrodes coated with 0.5 nm of MLD also maintained higher coulombic efficiencies (CE) as compared to the pristine electrodes. Initial CE was low in the coated and uncoated electrodes and is likely a result of SEI formation.[23] The 0.5 nm coated electrodes cycled with ~ 97 % efficiency between cycle 10 and 158.

Figure 3.9 shows representative voltage profiles and dQ/dV plots from the galvanostatic cycling tests. The voltage profiles in Figure 3.9A showed a small decrease in voltage with cycling for both pristine and 0.5 nm MLD coated electrodes in the first 10 cycles. By cycle 50 the voltage faded considerably in the pristine electrodes. In

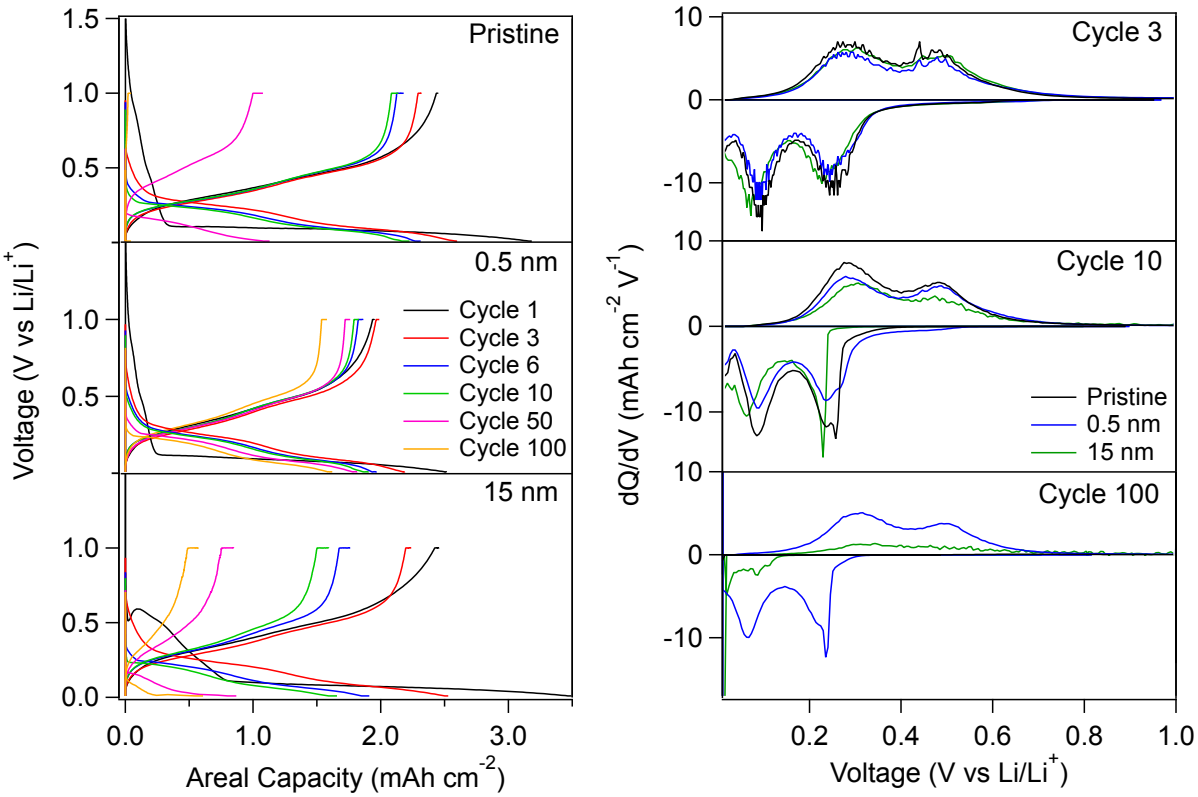

Figure 3.9 A) Voltage profiles and B) dQ/dV plots of representative cells from the cycling data in Figure 8. Voltage fade and lithiation overpotential are mitigated by the 0.5 nm MLD coating, and enhanced by the 15 nm MLD coating.

comparison, the electrodes coated with 15 nm of MLD showed considerable capacity and voltage fade with cycling. The dQ/dV plots in Figure 3.9B indicate increasing lithiation overpotential with cycling. Comparing cycle 10 to cycle 3, the onset of lithiation occurs 20, 50 and 90 mV later for the 0.5 nm coated, pristine, and 15 nm coated electrodes, respectively. At cycle 100, while the lithiation onset is 50 mV later than cycle 3 for the 0.5 nm coated electrodes, the cells in the other conditions have reached failure. The increased overpotential seen in all three conditions is likely a product of increased charge transfer resistance due to continual SEI formation. However, the thin 0.5 nm MLD coating appears to mitigate overpotential effects with extended cycling as compared to the pristine electrode. In comparison, the thick 15 nm MLD coating appears to increase overpotential effects, indicating that the thickness of the coating is the key factor to cycling stability.

Initial lithiation of pristine and 0.5 nm coated electrodes show similar voltage profiles in Figure 3.9A. Both electrodes show a relatively flat voltage plateau ~ 0.1 V, consistent with the first lithiation of silicon particles at room temperature.[24] In contrast, the 15 nm coated electrodes show starkly different behavior in initial lithiation. The electrodes with thick MLD coatings have an inflection point at ~ 0.5 V. These thickly coated electrodes also show a sloping voltage profile between ~ 0.6 and ~ 0.1 V in the first lithiation, resulting in a large irreversible capacity. The voltage dip at this point may indicate a kinetically limited step in the initial lithiation reaction, which has been

seen in other systems.[25,26] The sloping voltage and large irreversible capacity suggest that the thick coating may act as a barrier to Li^+ diffusion, and that a thick SEI layer is formed.[27–29] These attributes suggest that the formation of a very thin polyamide MLD layer is key to electrochemical stability.

The poor cycling performance of the electrodes with thick MLD coatings illustrate the necessity of controlling the thickness of the coating. Because polyamide is non-conductive, thicker coatings may significantly increase the resistance in the cell. Indeed, there is clear evidence that MLD coatings can increase cell resistance.[30] While the thicker MLD coating in this study had a large, detrimental effect on electrochemical performance, the thinner MLD coating extended cycling capacity and reduced voltage fade. It is possible that the added resistance from the MLD coating is minimized when the coating is very thin.

Figures 3.10 and 3.11 show the HAADF-STEM-EDS elemental mapping of silicon nanoparticles extracted from a 15 nm coated electrode before and after galvanostatic cycling, respectively. Before cycling, silicon particles are uniform, spherical and ~ 50 nm in diameter. The STEM-HAADF image shows that the spherical Si particles, with a strong bright contrast, are surrounded by a thin layer with a weak gray contrast. Since the contrast of the HAADF image is approximately proportional to the square of the atomic number, the less-bright-contrast thin layer is composed of lighter elements. The composition of the thin layer was confirmed with EDS analysis. Elemental mapping

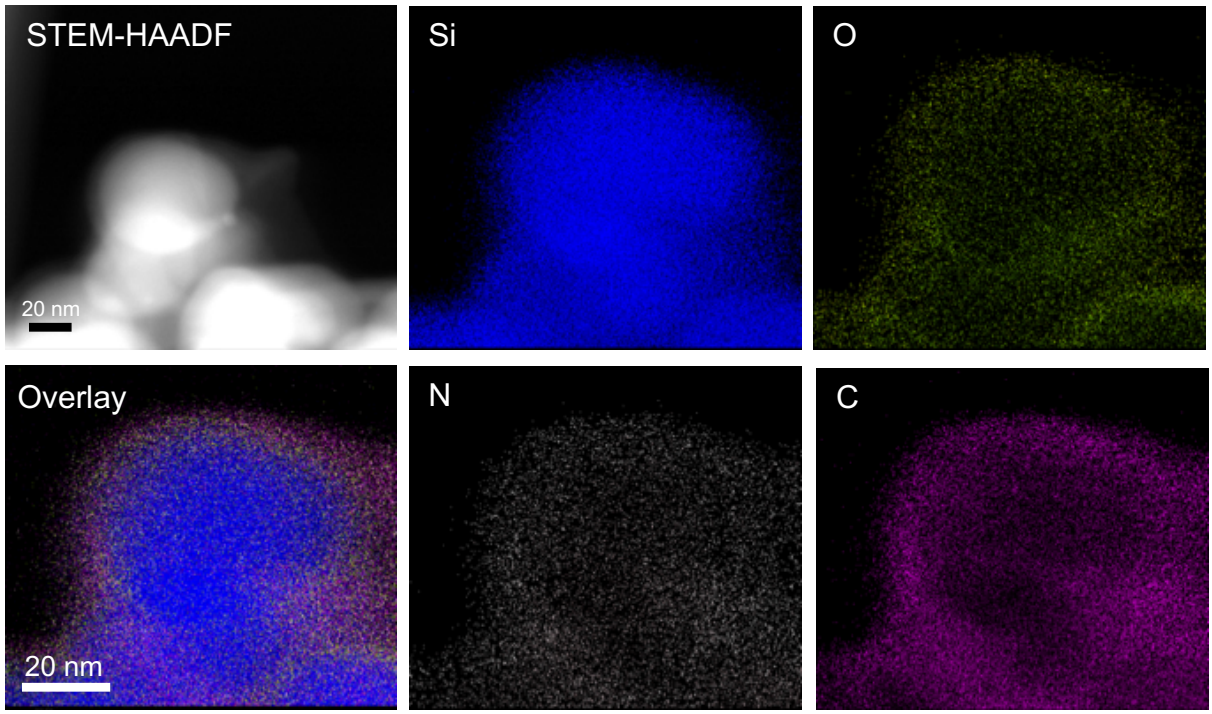

Figure 3.10 STEM-HAADF-EDS of silicon nanoparticles extracted from a silicon composite electrode coated with 15 nm of polyamide showing a uniform coating. The N signal is solely from the polyamide coating.

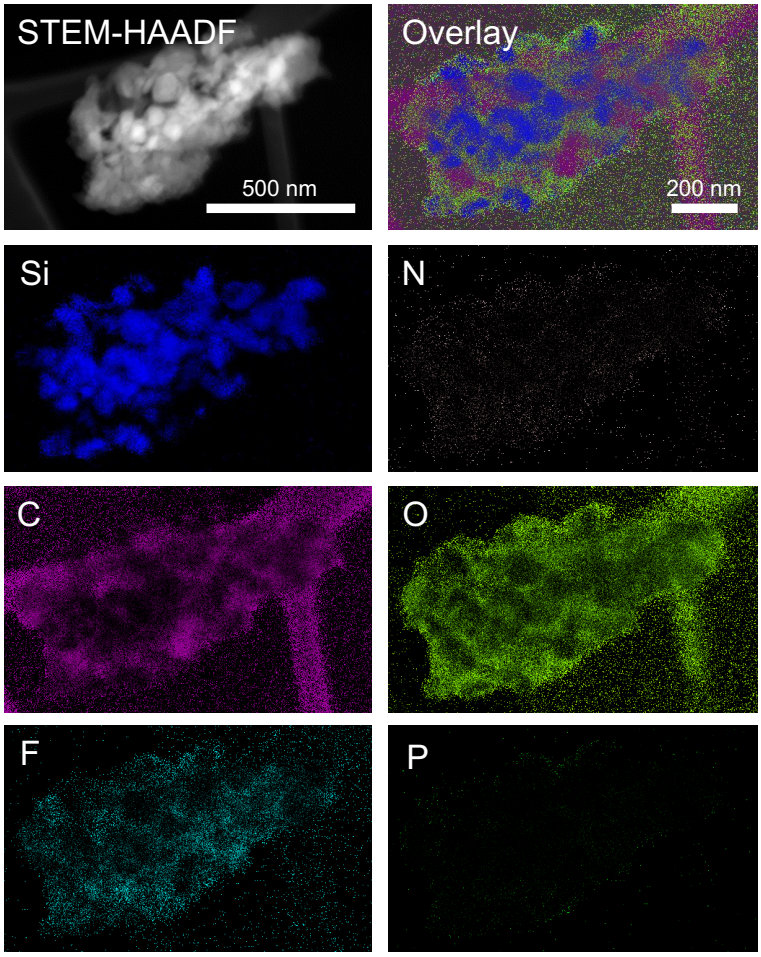

Figure 3.11 STEM-HAADF-EDS of silicon nanoparticles extracted from a silicon composite electrode coated with 15 nm of polyamide after galvanostatic cycling. Though the silicon particles no longer appear uniform, the polyamide coating is still present.

shows the presence of silicon, oxygen, nitrogen, and carbon. The oxygen signal may be from the native oxide on silicon or from the carboxylic acid groups in PAA. The carbon signal may be from carbon black or PAA. Only the nitrogen signal is solely indicative of the presence of the MLD coating. Elemental mapping in Figure 3.10 shows that the coating is evenly dispersed and conformally coated over the entire silicon particle. After cycling, additional elemental signals are present as a result of exposure to the electrolyte and formation of an SEI, as shown in Figure 3.11. The additional elements present are phosphorous and fluorine. The silicon undergoes a morphology change from spherical nanoparticles to irregularly shaped particles after cycling. Elemental mapping reveals the continued presence of a nitrogen signal from the MLD coating on the cycled particles. Though the nitrogen signal is attenuated, likely a result of the formation of the SEI, the nitrogen signal appears to continue to overlap with the surface of the silicon particle. The STEM results indicate that the MLD coating maintains intimate contact with the silicon particles as the electrode is cycled.

3.4 Conclusion

The polyamide MLD coating developed in this work was able to counteract the detrimental effects on cycling performance caused by the degradation of the PAA binder. The reduction of PAA to form polyacrylic anhydride lowers the elasticity of the electrode and reduces its cycling performance. This reaction can occur during the

electrode drying process prior to cell assembly or during cell cycling. This work examined the effect of an ultrathin polyamide coating on electrodes with degraded PAA. We found that the coating imparted favorable mechanical properties to the electrode. We also found that the thickness of the coating was a key factor in cycling stability. While a 15 nm coating caused high overpotentials and rapid capacity fade, a 0.5 nm coating enabled stable cycling for 158 cycles with a capacity > 1300 mAh/g. The coating was deposited with a spatial MLD chamber, permitting fast deposition and a viable route to scale-up.

The MLD coating explored in this work differs from previous studies of MLD coatings in two ways: 1) this MLD coating is an all-organic polymer and does not contain any metals; and 2) this MLD coating is five times thinner than the alucone MLD coatings explored previously. The mechanism that allows this thin coating to impart stable cycling is likely related to its increased elasticity, low solubility and chemical resistance. Future work on this coating may use in situ techniques to examine the exact mechanisms that give this coating its favorable properties.

3.5 References

(1) Magasinski, A.; Zdyrko, B.; Kovalenko, I.; Hertzberg, B.; Burtovyy, R.; Huebner, C. F.; Fuller, T. F.; Luzinov, I.; Yushin, G. *ACS Appl. Mater. Interfaces* **2010**, *2* (11), 3004–3010.

(2) Li, J.; Lewis, R. B.; Dahn, J. R. *Electrochem. Solid-State Lett.* **2007**, *10* (2), A17.

(3) Hochgatterer, N. S.; Schweiger, M. R.; Koller, S.; Raimann, P. R.; Wöhrle, T.; Wurm, C.; Winter, M. *Electrochem. Solid-State Lett.* **2008**, *11* (5), A76–A80.

(4) Munao, D.; van Erven, J. W. M.; Valvo, M.; Garcia-Tamayo, E.; Kelder, E. M. *J. Power Sources* **2011**, *196* (16), 6695–6702.

(5) Jeena, M. T.; Lee, J.-I.; Kim, S. H.; Kim, C.; Kim, J.-Y.; Park, S.; Ryu, J.-H. *ACS Appl. Mater. Interfaces* **2014**, *6* (20), 18001–18007.

(6) McNeill, I. C.; Sadeghi, S. M. T. *Polym. Degrad. Stab.* **1990**, *29* (2), 233–246.

(7) Nguyen, C. C.; Yoon, T.; Seo, D. M.; Guduru, P.; Lucht, B. L. *ACS Appl. Mater. Interfaces* **2016**, *8* (19), 12211–12220.

(8) Hays, K. A.; Ruther, R. E.; Kukay, A. J.; Cao, P.; Saito, T.; Wood, D. L.; Li, J. *J. Power Sources* **2018**, *384*, 136–144.

(9) Son, S.-B.; Wang, Y.; Xu, J.; Li, X.; Groner, M.; Stokes, A.; Yang, Y.; Cheng, Y.-T.; Ban, C. *ACS Appl. Mater. Interfaces* **2017**, *9* (46), 40143–40150.

(10) Piper, D. M.; Travis, J. J.; Young, M.; Son, S.-B.; Kim, S. C.; Oh, K. H.; George, S. M.; Ban, C.; Lee, S.-H. *Adv. Mater.* **2014**, *26* (10), 1596–1601.

(11) Ma, Y.; Martinez de la Hoz, J. M.; Angarita, I.; Berrio-Sanchez, J. M.; Benitez, L.; Seminario, J. M.; Son, S.-B.; Lee, S.-H.; George, S. M.; Ban, C.; et al. *ACS Appl. Mater. Interfaces* **2015**, *7* (22), 11948–11955.

(12) García, J. M.; García, F. C.; Serna, F.; de la Peña, J. L. *Prog. Polym. Sci.* **2010**, *35* (5), 623–686.

(13) Tashiro, K.; Kobayashi, M.; Tadokoro, H. *Macromolecules* **1977**, *10* (2), 413–420.

(14) Yang, H.; Wang, Y.; Duh, J.-G. *ACS Sustain. Chem. Eng.* **2018**, *6* (10), 13302–13311.

(15) Choi, N.-S.; Yew, K. H.; Choi, W.-U.; Kim, S.-S. *J. Power Sources* **2008**, *177* (2), 590–

594.

(16) Chen, J.; Liu, Q.; Wang, B.; Li, F.; Jiang, H.; Liu, K.; Wang, Y.; Li, M.; Lu, Z.; Wang, D. *J. Electrochem. Soc.* **2017**, *164* (7), A1526–A1533.

(17) Higgs, D. J.; DuMont, J. W.; Sharma, K.; George, S. M. *J. Vac. Sci. Technol. A Vacuum, Surfaces, Film.* **2018**, *36* (1), 01A117.

(18) Sharma, K.; Hall, R. A.; George, S. M. *J. Vac. Sci. Technol. A Vacuum, Surfaces, Film.* **2015**, *33* (1), 01A132.

(19) Yersak, A. S.; Sharma, K.; Wallas, J. M.; Dameron, A. A.; Li, X.; Yang, Y.; Hurst, K. E.; Ban, C.; Tenent, R. C.; George, S. M. *J. Vac. Sci. Technol. A Vacuum, Surfaces, Film.* **2018**, *36* (1), 01A123.

(20) Oliver, W. C.; Pharr, G. M. *J. Mater. Res.* **1992**, *7* (06), 1564–1583.

(21) Wang, Y.; Zhang, Q.; Li, D.; Hu, J.; Xu, J.; Dang, D.; Xiao, X.; Cheng, Y.-T. *Adv. Energy Mater.* **2018**, *8* (10), 1702578.

(22) Elam, J. W.; Routkevitch, D.; Mardilovich, P. P.; George, S. M. *Chem. Mater.* **2003**, *15* (18), 3507–3517.

(23) Jin, Y.; Zhu, B.; Lu, Z.; Liu, N.; Zhu, J. *Adv. Energy Mater.* **2017**, *7* (23), 1700715.

(24) McDowell, M. T.; Lee, S. W.; Nix, W. D.; Cui, Y. *Adv. Mater.* **2013**, *25* (36), 4966–4985.

(25) Li, L.; Cabán-Acevedo, M.; Girard, S. N.; Jin, S. *Nanoscale* **2014**, *6* (4), 2112–2118.

(26) Girishkumar, G.; McCloskey, B.; Luntz, A. C.; Swanson, S.; Wilcke, W. *J. Phys. Chem. Lett.* **2010**, *1* (14), 2193–2203.

(27) Gao, B.; Sinha, S.; Fleming, L.; Zhou, O. *Adv. Mater.* **2001**, *13* (11), 816–819.

(28) Yao, Y.; Zhang, J.; Xue, L.; Huang, T.; Yu, A. *J. Power Sources* **2011**, *196* (23), 10240–10243.

(29) Wu, X.; Shi, Z.; Wang, C.; Jin, J. *J. Electroanal. Chem.* **2015**, *746*, 62–67.

(30) Molina Piper, D.; Lee, Y.; Son, S.-B.; Evans, T.; Lin, F.; Nordlund, D.; Xiao, X.; George, S. M.; Lee, S.-H.; Ban, C. *Nano Energy* **2016**, *22*, 202–210.

4. Efficient Capacitive Deionization Using Thin Film Sodium Manganese Oxide

Jasmine M. Wallas[1], Matthias J. Young[2,3,*], Huaxing Sun[1], and Steven M. George[1,4,*]

[1]*Department of Chemistry and Biochemistry, University of Colorado, Boulder, Colorado 80309*

[2]*Applied Chemicals and Materials Division, National Institute of Standards and Technology, Boulder, Colorado, 80305*

[3]*Energy Systems, Argonne National Laboratory, Argonne, Illinois, 60439, United States*

[4]*Department of Mechanical Engineering, University of Colorado, Boulder, Colorado 80309*

4.1 Introduction

Fresh drinking water is becoming increasingly scarce around the globe, intensifying the need for energy efficient desalination methods that could be powered with renewable sources.[1] The need for fresh drinking water tops the list of *50 Breakthroughs: Critical scientific and technological advances needed for sustainable global development* compiled by the Institute of Globally Transformative Technologies at Lawrence Berkeley National Lab.[2] Capacitive deionization (CDI) is a promising water desalination technique based on the reversible electrosorption of ions. Unlike other desalination techniques, CDI requires only a nominal voltage, and therefore could easily be coupled with solar power or other renewable energy sources.

During CDI operation, the electrical potential across two electrodes is cycled between two modes, a 'desalination' half cycle and a 'regeneration' half cycle. During the desalination half cycle of a traditional CDI cell an electrical potential is applied to the CDI cell, causing ion sorption to the electrodes and producing fresh water. During the regeneration half cycle of a traditional CDI cell the polarization is reduced or reversed and ions desorb from the electrodes, thereby regenerating the electrodes and producing brine. Conventionally, CDI electrodes are composed of inert carbon. In these carbon electrodes, energy is stored during the desalination step by ion sorption in the electric double layer (EDL), and some of this energy can be recovered during regeneration. This unique behavior lowers the overall net energy consumption of CDI, particularly for desalination of low salinity feed waters.[3]

To compete with commercial desalination technologies used for higher salinities (e.g. reverse osmosis), CDI costs must be reduced. At present CDI is viable at saltwater concentrations below ~ 0.05 M, well below the salinity levels of seawater.[3,4] Carbon electrodes currently used in CDI have low salt sorption capacity (SSC) (units in mg NaCl (g electrode)$^{-1}$), limited to the available surface area for EDL ion sorption. Low salt sorption capacity leads to larger devices with higher capital costs. Additionally, low salt sorption capacity materials require larger composite electrode thicknesses, which introduce ohmic and diffusion losses and limit the efficiency of conventional CDI.

By increasing the capacity of CDI electrode materials, smaller devices can be constructed using thinner electrodes, which will reduce capital costs and provide lower operating costs through greater energy efficiency. Consequently, hybrid CDI (HCDI) electrodes that incorporate ion intercalation materials commonly used in batteries and supercapacitors have been explored and have shown to improve performance.[5–7] These materials often have higher charge storage capacities (CSC) (with units of F g^{-1} or F cm^{-2}) than carbon electrodes, and exhibit low self-discharge rates.[8] The use of ion-selective intercalation materials is expected to increase charge efficiency (Λ = mol NaCl (mol e-)$^{-1}$) by reducing the energetic contribution of co-ion desorption during the charging half-cycle, and to increase the coulombic efficiency (η = mol $e_{regneration}$/mol $e_{desalination}$) due to the low self-discharging properties of these materials.

Manganese oxide, used as a reversible Na^+ intercalation material in Na-ion batteries,[9–11] is a promising candidate for increasing the SSC of HCDI electrodes. Recent studies have confirmed that the CSC of MnO_2 in aqueous Na^+ solutions is largely due to cation (i.e. Na^+) sorption and intercalation.[12–17] Several reports have investigated the incorporation of sodium manganese oxide (NMO) particles into HCDI electrodes, demonstrating modest improvements in SSC.[6,7,18–20] Using an NMO electrode, Lee et al. achieved the highest HCDI SSC at 31.2 $mg_{(salt)}/g_{(electrode)}$, more than twice that of the highest SSC reported for a conventional CDI system.[4,7] This increase in SSC was achieved by adding $Na_{0.44}MnO_2$ particles into the cell's carbon cathode. However, this

factor of two increase falls well short of the factor of ten improvement expected when comparing NMO CSC versus carbon CSC, suggesting that the advantages of NMO may not have been fully realized in these studies.[21,22]

Here we describe the study of Na^+ intercalation and charge storage in nanoscale thin films of NMO formed with a controlled two-step process – atomic layer deposition (ALD) of MnO, followed by electrochemical oxidation to form NMO – and provide an initial study of its potential application to enhance HCDI. This work expands on previous work from our group, where NMO was formed from MnO in $Na_2SO_{4(aq)}$.[13] Here, we electrochemically convert MnO to NMO in $NaCl_{(aq)}$ to mimic industrially relevant feed water for eventual simplified deployment in HCDI devices. By measuring the CSC versus thickness after conversion to NMO, we probe the depth to which MnO is oxidized to NMO in $NaCl_{(aq)}$. We use these results to produce HCDI cathodes with a starting MnO thickness tuned to produce the highest possible capacity.

We compare cycling performance of a conventional CDI configuration consisting of two carbon nanotube (CNT) electrodes and an HCDI configuration where the CNT cathode is coated with NMO, as described above, and the CNT anode is decorated with Ag nanoparticles. The desalination mechanism of this HCDI cell differs from traditional CDI and is shown in Figure 4.1. This work contrasts prior studies on HCDI electrodes that exclusively used particulate active material. The use of a conformal NMO thin-film coating is expected to enhance performance by increasing electrical connectivity[23] and

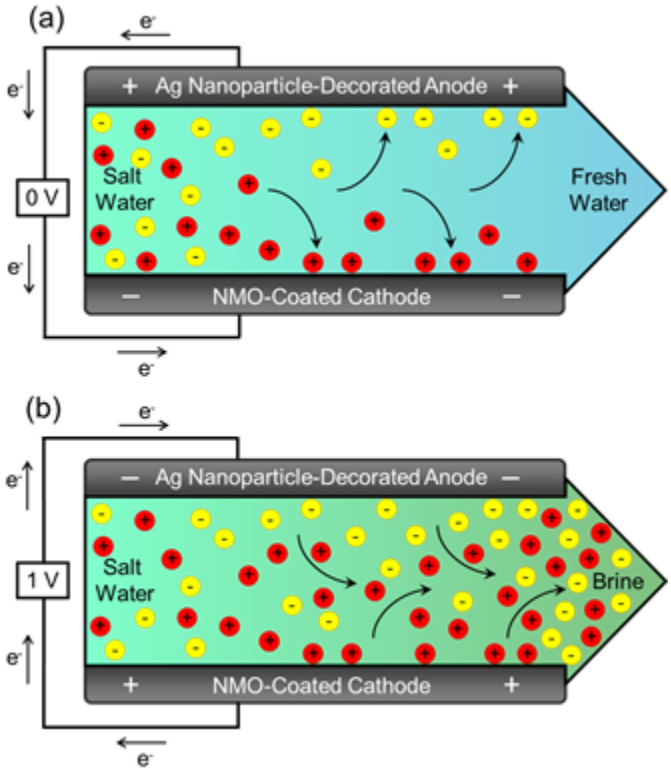

Figure 4.1 Schematic diagram of hybrid capacitive deionization (HCDI) with an NMO coated cathode and Ag nanoparticle decorated anode showing (a) desalination and (b) electrode regeneration.

decreasing the diffusion lengths required for Na^+ to access the NMO. This HCDI cell exhibits low net energy consumption and high charging efficiency (mol NaCl (mol e-)$^{-1}$). We explore the relationship between charge storage and salt sorption in NMO using EQCM to understand the high efficiency we observe.

4.2 Experimental Section

4.2A Electrode Fabrication

Electrodes for the conventional CDI test cell were composed of multi-walled hydroxylated carbon nanotubes (CNT-OH) (> 95%, 10-20 nm OD, > 200 m^2/g, Nanostructured and Amorphous Materials, Inc.) with a 20% by weight poly(vinyldene fluoride) (PVDF) (M_w ~ 530,000, Aldrich) binder on titanium (Ti) discs (99.6%, annealed, 0.5 mm, Goodfellow) cut to a 4 cm diameter with electron discharge machining before coating. Hydroxyl-functionalized CNTs were used to promote ALD nucleation, while binder mass loadings of 20% were used in the electrodes to support mechanical stability during volume expansion in NMO conversion[13] and Ag/AgCl reaction. Ti substrate was used for electrochemical testing due to its conductivity and corrosion resistance in $NaCl_{(aq)}$.[24]

A slurry composed of 8 mg/mL CNT-OH and 2 mg/mL PVDF in 1-methyl-2-pyrrolidinone (ACS reagent, ≥ 99.0%, Sigma-Aldrich) was coated onto a Ti disc at 25 μL/cm^2, corresponding to 0.2 mg/cm^2 CNT-OH. Films were heated to ~ 80°C overnight

to dry. The cathode in the HCDI cell was assembled in the same fashion as described above, and then coated using ALD deposition. The anode in the HCDI cell was supplemented with silver nanopowder (Ag NP) (< 100 nm particle size, PVP dispersant, 99.5% trace metals basis, Aldrich) to avoid capacity limitations while studying the NMO electrodes. A slurry of 78 mg/mL Ag NP, 20 mg/mL PVDF, and 2 mg/mL CNTs (7000 series, Nanocyl) was coated onto a Ti disc at 80 μL/cm^2. Assembled composite electrodes were allowed to wet in the electrolyte solution for ~ 8 hours before electrochemical testing in order to avoid progressive wetting effects.

4.2B Atomic Layer Deposition

Thin film metal oxide coatings were deposited onto silicon (Si, Silicon Valley Microelectronics), titanium (Ti, Sigma Aldrich, 0.25 mm, 99.7% trace metals basis), and hydroxylated carbon nanotubes (CNT-OH) electrode films using a custom-built hot-walled ALD reactor. Si samples were cut to 1″ × 1″. Ti samples were cut to 5/8″ diameter discs using electron discharge machining before coating. Si and Ti samples were rinsed with acetone (Fisher, Certified ACS) and methanol (EMD Millipore HPLC grade) and dried using a jet of ultra-high purity nitrogen (Airgas). Si and Ti samples were also cleaned in the reactor before ALD deposition using a water plasma at ~ 300 mTorr of water pressure for 30 s.

ALD onto Si, Ti, and EQCM crystal samples was performed in a viscous flow reaction configuration as described previously.[13,25] MnO was deposited by sequential

exposures of (A) bis(ethylcyclopentadienyl) manganese ($Mn(CpEt)_2$, >98%, Strem Chemicals) and (B) water (H_2O, B&J Brand HPLC Grade) at 150°C under 1 Torr of 120 sccm continuous argon (Ar) gas purge (Airgas, Prepurified). $Mn(CpEt)_2$ was dosed using a vapor-draw configuration where Ar flow was directed over the head-space of the bubbler. H_2O doses were tuned to ~200 mTorr above base pressure. Dosing was performed using a timing sequence of (0.5 s):(20 s):(0.5 s):(20 s) for one ALD cycle of (A):(Purge):(B):(Purge).

ALD onto high surface area CNT-OH electrode films was performed in a static flow reaction configuration without carrier gas flow during dosing. This deposition mode was selected for CNT-OH electrode films due to its higher precursor utilization and better conformality on high-aspect ratio substrates. The reactor temperature was lowered to 120°C to prevent $Mn(CpEt)_2$ decomposition during the longer reaction times. The reactor was pumped down to base pressure for 75 s before each dose. $Mn(CpEt)_2$ was dosed using a series of 10 microdoses following a (dose time):(static time):(purge time) timing sequence of (5 s):(70 s):(20 s) to reach a total combined exposure of ~4 Torr·s per cycle. The H_2O vapor pressure was sufficiently large such that only a single static dose of H_2O was required, which was tuned to ~1 Torr above base pressure with a (dose time):(static time):(purge time) timing sequence of (2 s):(70 s):(20 s). Between each precursor dose, 5 cycles of Argon purging was performed, each with a (static fill):(static hold):(evacuate):(viscous purge) timing sequence of (20 s):(5 s):(55 s):(50 s).

4.2C Thin Film Characterization

X-ray reflectivity (XRR) and grazing incidence X-ray diffraction (GIXRD, BEDE D-1 Diffractometer, Jordan Valley Semiconductors) was used to measure film thickness and density and crystallinity on Si using the Cu-Kα transition at 1.54 Å. XRR data was modelled with the BEDE REFs software package (Jordan Valley Semiconductors). The GIXRD angle of incidence was 0.3°, the step size was ≤ 0.05 arcseconds and the count time was ≥ 20 s.

Spectroscopic ellipsometry (SE) (M-2000, J.A. Woollam Co., Inc.) was used to measure ALD film thicknesses on Ti and corroborate XRR on Si samples. XRR could not be used on Ti due to the higher surface roughness on Ti substrates. SE measurements were performed over a spectral range of 240 nm to 1685 nm with a 75° incident angle. Data was modeled with CompleteEASE v.4.55 (J. A. Woollam Co., Inc.). A Kramers-Kronig consistent B-spline model was used for silicon and silicon oxide materials files for the Si samples with a native SiO_2 film. A Kramers-Kronig consistent B-spline model was also used for Ti. A Cody-Lorentz model was used for MnO ALD films, as described previously.[13]

4.2D Electrochemical Oxidation and Characterization

MnO ALD films grown on Ti discs were oxidized to NMO electrochemically (SP-300 Potentiostat, 2-channel, low current probes, BioLogic) in a custom-built 3-electrode cell equipped with a saturated Ag/AgCl reference and Pt coil counter electrode (BASi).

A surface area of 1.21 cm^2 of the ALD coated disc was exposed to electrolyte and defined the electrochemically active area. A 0.10 M NaCl (Alfa Aesar, 99.99%) electrolyte solution was purged >10 min with Ar and kept under continuous Ar purge during measurements.

MnO oxidation to NMO was performed following a procedure described previously.[13] Chronopotentiometry (CP) was used to apply 16.5 $\mu A/cm^2$ of oxidative current in 3 min cycles. Three cyclic voltammetry (CV) cycles between 0.9 V and 0 V vs. Ag/AgCl at 20 mV/s were used between each CP interval to monitor oxidation progress. Cycles of CP and CV were repeated until a steady state was reached. An increase in the CSC indicates conversion of the MnO film to NMO. Once oxidized, film capacity was measured with CV at a scan rate of 20 mV/s. Capacity, in units of Farads (F), was calculated from the integral of the current over the potential window of 0.9 V.

MnO ALD films grown on CNT-OH films on Ti discs were oxidized in a similar fashion. A Ti wire (0.5 mm diameter, annealed, 99.99%, Alfa Aesar) was temporarily spot welded to the back of the Ti disc for oxidation. Electrochemical oxidation was performed in a three-electrode setup in a 0.10 M NaCl electrolyte solution. Electrolyte was purged for >30 min with Ar gas before oxidation, and kept under continuous Ar gas purge throughout the course of the oxidation.

4.2E X-Ray Photoelectron Spectroscopy

Film composition was characterized with X-ray photoelectron spectroscopy (XPS). XPS was conducted using a PHI 5600 X-ray photoelectron spectrometer (RBD Instruments) with a monochromatic Al-Kα x-ray source at 1486.6 eV. Depth profiling was accomplished with 90s argon ion sputtering intervals between spectra acquisitions. Spectra were obtained using a pass energy of 29.35 eV, a step size of 0.25 eV, and Auto-Neutralization mode. AugerScan control program (RBD Instruments) was used to collect data, and CasaXPS software (Casa Software) was used to analyze XPS data.

4.2F Electrochemical Quartz Crystal Microbalance

Electrochemical quartz crystal microbalance (EQCM) was employed to evaluate mass changes due to ion sorption and intercalation during potential scans. MnO ALD films were deposited as described in sub-section B onto Pt-plated EQCM crystals (1" diameter, AT-cut quartz crystal wafer, Stanford Research Systems). Electrochemistry was conducted in a custom glass electrochemical cell attached to an EQCM crystal holder (Stanford Research Systems) with a Pt counter and saturated Ag/AgCl reference electrode in 0.10 M $NaCl_{(aq)}$ electrolyte.

EQCM resonator frequency was recorded with a QCM200 (Stanford Research Systems) using a BioLogic potentiostat and control software. Mass changes (Δm) were calculated from frequency changes (Δf) using the simplified Sauerbrey equation, $\Delta m = 56.6\ \mu g\ (cm^2\ Hz)^{-1} \times \Delta f \times A$, where A is the surface area of the QCM crystal exposed to

the electrolyte (1.37 cm^2). EQCM measurements were performed with capacitance compensation. The series resonant resistance was measured to be < 2 Ω in the NMO-coated EQCM experiments, indicating that dissipation effects are negligible for these films. [26,27]

4.2G Desalination Performance Tests

Desalination performance was evaluated with a custom HCDI cell, as shown in Figure 4.2. The HCDI cell is composed of two Ti disc (0.5 mm, 99.7%, annealed, Goodfellow) current collectors that were electron discharge machined to 4.0 cm diameter, thin CNT electrodes decorated with nanoscale materials, and a glass fiber separator (380 μm, EMD Millipore Glass Fiber Filter Grade AP20, Fisher Scientific). Tubing in and out of the cell was 1/16" ID PTFE. The HCDI cell was operated at a constant voltage, cycling between 0.0 and 1.0 V, with a cycle time of 30 minutes to allow sufficient time for salt sorption. The cell was operated in single-pass mode, with solution constantly flowing through the cell at a fixed rate. A long cycle length was used to ensure maximum desalination and regeneration values.

The cell was designed to detect the removal of small amounts of salt that arise from the sorption of ions into relatively small quantities of nanoscale material electrodes. Measurement of discrete changes in salt concentration was achieved by limiting the electrolyte volume of the cell and tubing, as depicted in Figure 4.2a, which prevents appreciable mixing between salt-depleted and salty electrolyte. We

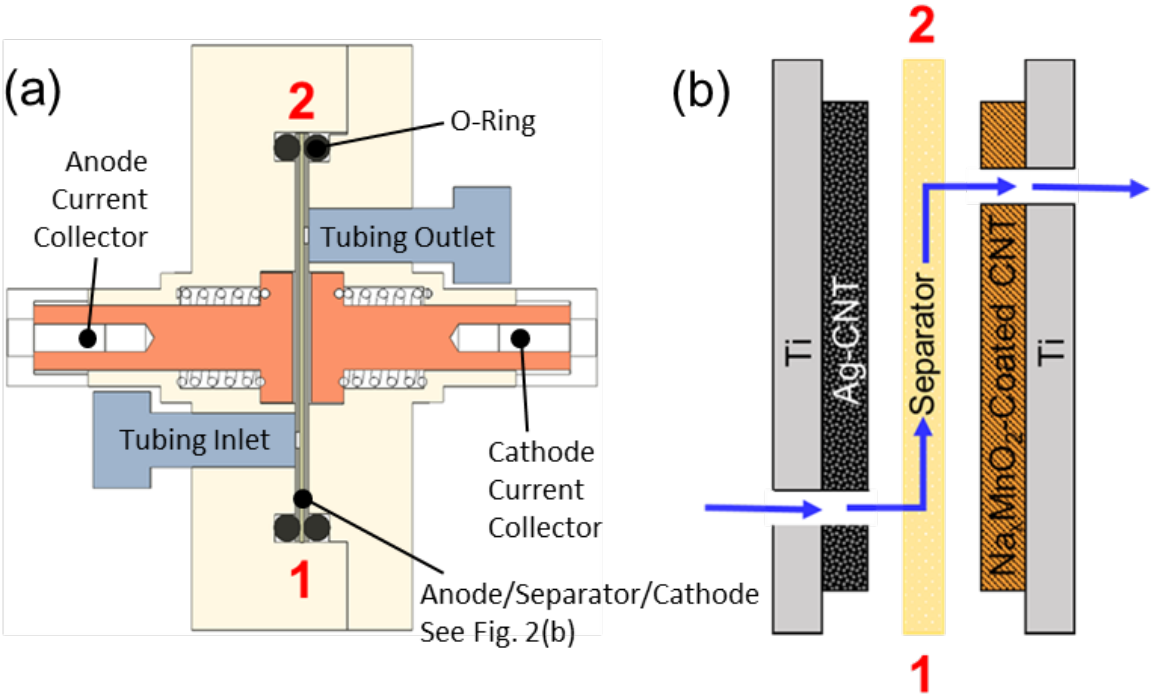

Figure 4.2 Depictions of hybrid capacitive deionization (HCDI) test cell. (a) Schematic cross-section of test cell. (b) Magnified schematic of electrode assembly, depicting the direction of water flow across the separator.

constrained the cell volume to 0.48 cm^3 to allow for desalination of multiple reservoir volumes based on estimates of SSC using NMO CSC data. The small electrolyte volume in the cell and tubing allowed us to measure desalination performance with smaller mass loadings of active material. Smaller mass loadings reduce the electrode thickness and minimize charge transfer resistance and diffusion effects, while maximizing electrode wetting. While most CDI test cells described in the literature use tens of mg/cm^2 of carbon material per electrode,[7,28,29] our cell is designed to require < 1 mg/cm^2 of carbon in each electrode. While this cell design is helpful for materials characterization and understanding, other cell designs are perhaps more practical for scale-up.[4,28,30]

In order to improve electrode/electrolyte contact, the HCDI cell was designed with a torturous electrolyte flow path. Each Ti disc was bored with a 1/16" diameter hole at 1 cm or 3 cm along the diameter for water feed through. These holes were placed opposite one another as depicted in Figure 4.2b, and electrolyte flow was directed through the opening in one Ti disc, across the separator, and out through the small opening on the opposite side of the cell in the second Ti disc. Flow was controlled with a Kent Scientific Genie Plus syringe pump with a 60 mL BD Luer-Lok syringe at a continuous flow rate of 0.200 mL/min. Both the pump and syringe flow rates are accurate to ± 1%, and the flow rate through the cell was manually verified by collecting

the effluent in a graduated cylinder. Electrolyte concentration was 0.10 M $NaCl_{(aq)}$ and was drawn from a larger electrolyte volume of 1 L to ensure isothermal operation.

A 1/16" diameter flow-through conductivity meter (Microelectrodes, Inc.), positioned downstream of the cell, was used to monitor the salinity of the effluent solution and evaluate desalination performance. This low-volume conductivity probe, housed inside of a rigid low-volume case, allowed for continuous monitoring of the effluent salt concentration. Potential-controlled electrochemical impedance spectroscopy (PEIS) was used to monitor the impedance across the conductivity meter on the BioLogic potentiostat. A sine amplitude of 10.0 mV at a fixed potential of 200 mV was used for PEIS measurements, and the conductivity was evaluated at a frequency of 50 kHz to determine salt concentration. PEIS measurement values were subsequently converted to NaCl concentrations using calibration data. PEIS measurements were calibrated before and after each run using NaCl concentrations of 0.01, 0.10, and 1.00 M.

4.3 Results and Discussion

The first part of this work aimed to characterize the formation of NMO when oxidizing MnO thin films in aqueous NaCl electrolyte. Flat substrates and a three-electrode setup were used to study NMO formation to reduce the contribution of EDL charge storage and better understand Na^+ sorption processes in NMO. In the second part of this work, desalination capacity and efficiency of an HCDI cell containing an

NMO-coated electrode were studied using the custom test cell (Figure 4.2). A high surface area NMO-coated CNT cathode was used in CDI tests to enhance the overall capacity. High surface area CNTs were chosen to enable reasonable desalination performance in the CDI cell and to provide sufficient surface area for MnO deposition. In the third part of this work, the relationship between charge storage and ion removal in NMO was further probed with EQCM.

4.3A NMO Formation

NMO film formation involved a two-step process of deposition and post-treatment, inspired by our previous work.[13] The growth rate of MnO ALD is 1.0 Å per deposition cycle on Ti in a viscous-flow configuration as measured by spectroscopic ellipsometry, and 2.1 Å per deposition cycle on silicon in a static configuration as measured by X-ray reflectivity (XRR). GIXRD of the as-deposited film reveals peaks consistent with crystalline MnO. GIXRD of the converted NMO film suggests an amorphous composition. A higher growth rate in the static configuration as compared to the viscous configuration has been reported for other ALD chemistries, and may be explained by sub-saturation of the surface reactions during viscous growth.[31–33] The higher growth rate may also be explained by a CVD component to the growth, given the extended exposure times as compared with prior work[25] and low activation energies for decomposition of metal-cyclopentadienyl precursors on the order of ~25-35 kcal/mol.[34]

MnO films were post-processed with electrochemical oxidation in $NaCl_{(aq)}$. $NaCl_{(aq)}$ is used here in anticipation of the eventual development of MnO films in HCDI devices with *in operando* conversion to NMO during desalination of seawater or inland watershed. Conversion to NMO results in a large increase in CSC and a change in the visual appearance of the sample from a reflective green color (due to thin film interference) to a matte orange-brown, as shown in the photographs of the sample in Figure 4.3. The conversion of MnO to NMO in $NaCl_{(aq)}$ is qualitatively consistent with conversion seen previously in $Na_2SO_{4(aq)}$.[13]

We observe significant increases in CSC of NMO over bare Ti and MnO. These increases are consistent with conversion in $Na_2SO_{4(aq)}$.[13] CSC values are derived from cyclic voltammetry (CV) sweeps at 20 mV/s, as shown in Figure 4.3. CSCs in NMO films are stable upon electrochemical cycling. A ~80 nm thick NMO film cycled 300 times between 0.0 and 0.9 V vs Ag/AgCl in 0.10 M $NaCl_{(aq)}$ did not experience any capacity fade (Figure 4.4). Instead, there was a 6% increase in CSC over extended CV cycling. CSC values reported below are average values calculated for the full potential range during oxidizing sweeps. CSC values are normalized to either top-down surface area of the electrode exposed to the electrolyte (1.21 cm^2) for areal capacitance, or mass of NMO calculated from MnO thickness and density from XRR and assuming complete conversion to NMO for specific mass capacitance.

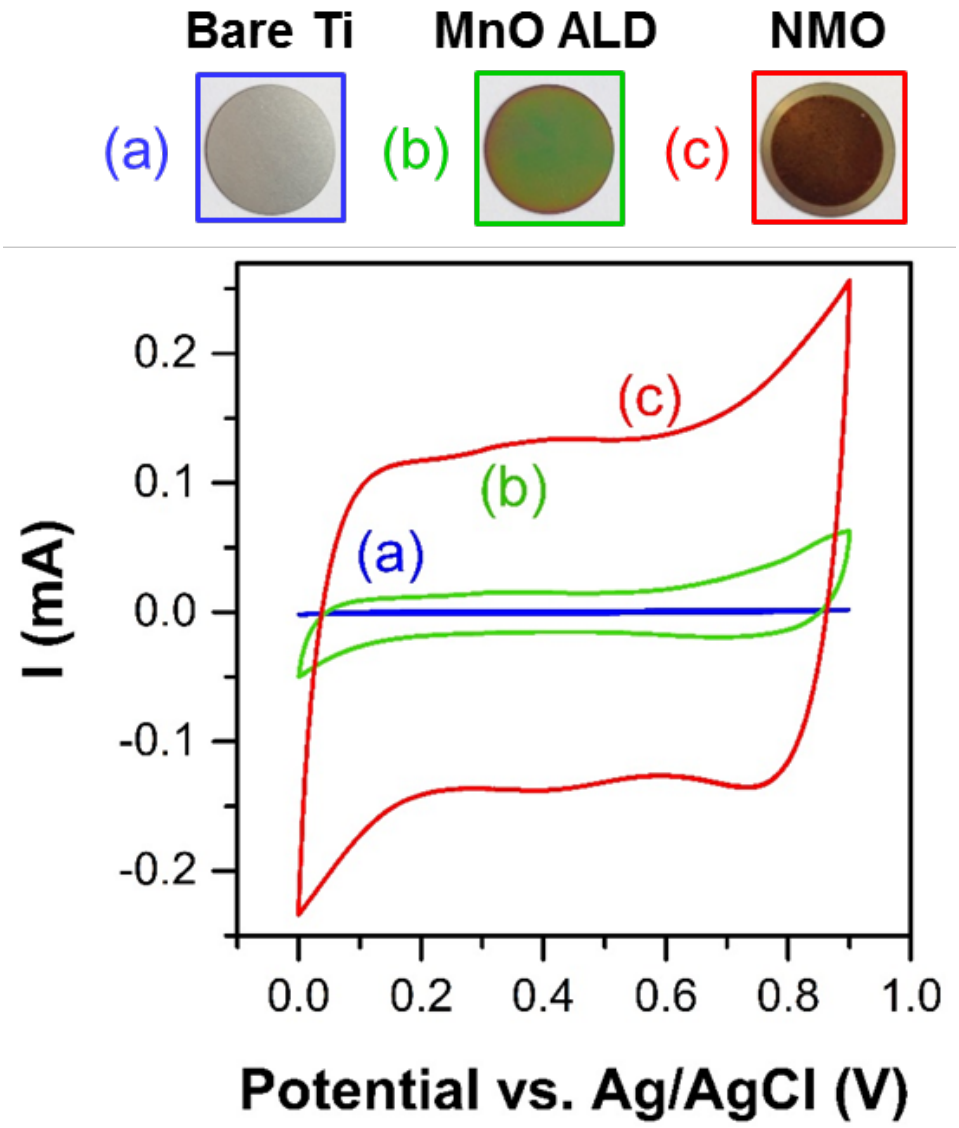

Figure 4.3 Cyclic voltammetry (CV) and corresponding photographs of (a) Ti substrate, (b) 500 ALD cycles of MnO and (c) oxidized NMO film.

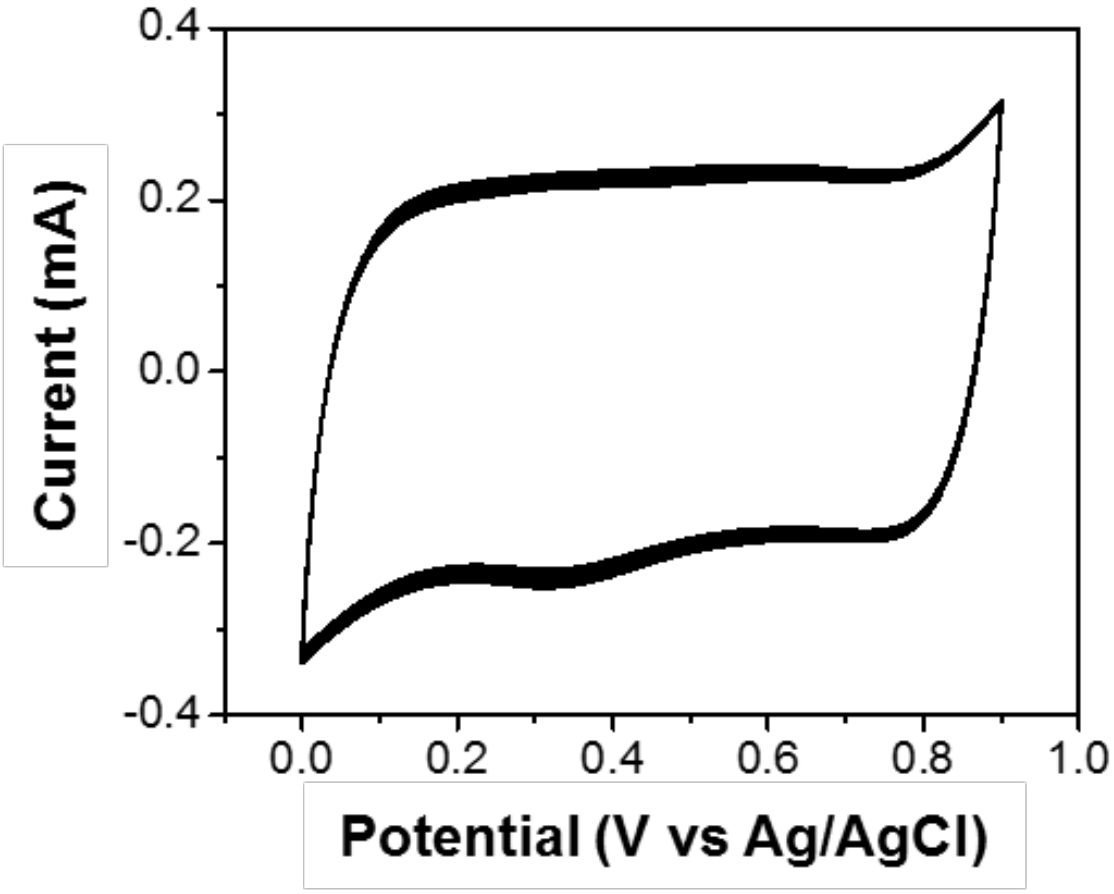

Figure 4.4 Stability of a NMO film (~80 nm) on Ti deposited with 800 ALD cycles over 300 cyclic voltammetry cycles. Cyclic voltammetry was measured at 20 mV/s in 0.10 M NaCl(aq) using a three-electrode setup.

Bare Ti has a small, reversible areal CSC of 0.032 ± 0.02 mF/cm^2. The areal CSC of Ti is attributed solely to charge storage in the EDL at the surface of the flat substrate. MnO coated Ti samples exhibit a somewhat higher CSC. While MnO is not expected to exhibit electrochemical charge storage, previous studies have shown that ALD MnO films form a thin surface layer of MnO_2.[25] The higher CSC of MnO-coated Ti samples may be attributed to this surface MnO_2. Following electrochemical conversion to NMO, these films have a much higher CSC. Compared to bare Ti, NMO coatings have a thickness-dependent increase in areal capacitance by a factor of up to 170. Given the consistency in behavior between conversion in $Na_2SO_{4(aq)}$ and $NaCl_{(aq)}$, the CSC increase shown in Figure 4.3 is likely due to Na^+-mediated charge storage in NMO.[12,13]

4.3B Verifying Na-Mediated Charge Storage

XPS depth-profiling was used to confirm the incorporation of Na into NMO formed in $NaCl_{(aq)}$. XPS shows Na incorporation at the surface and in the near-surface bulk of the NMO film, as depicted in Figure 4.5. Depth profiling reveals an O:Mn ratio > 1.5 through the entire thickness of an 81.7 nm film. The near-surface ~14 nm of the film has an O:Mn ratio of 2.1, whereas the ~68 nm bulk of the film has a slightly lower oxygen content ratio of 1.6. Similarly, the surface of the film has a higher Na content than the bulk. Shown in Figure 4.5b, the bulk of the film has a Na:Mn ratio of 0.06, while the near-surface ~14 nm has a higher Na content, and a maximum Na:Mn ratio of 0.17.

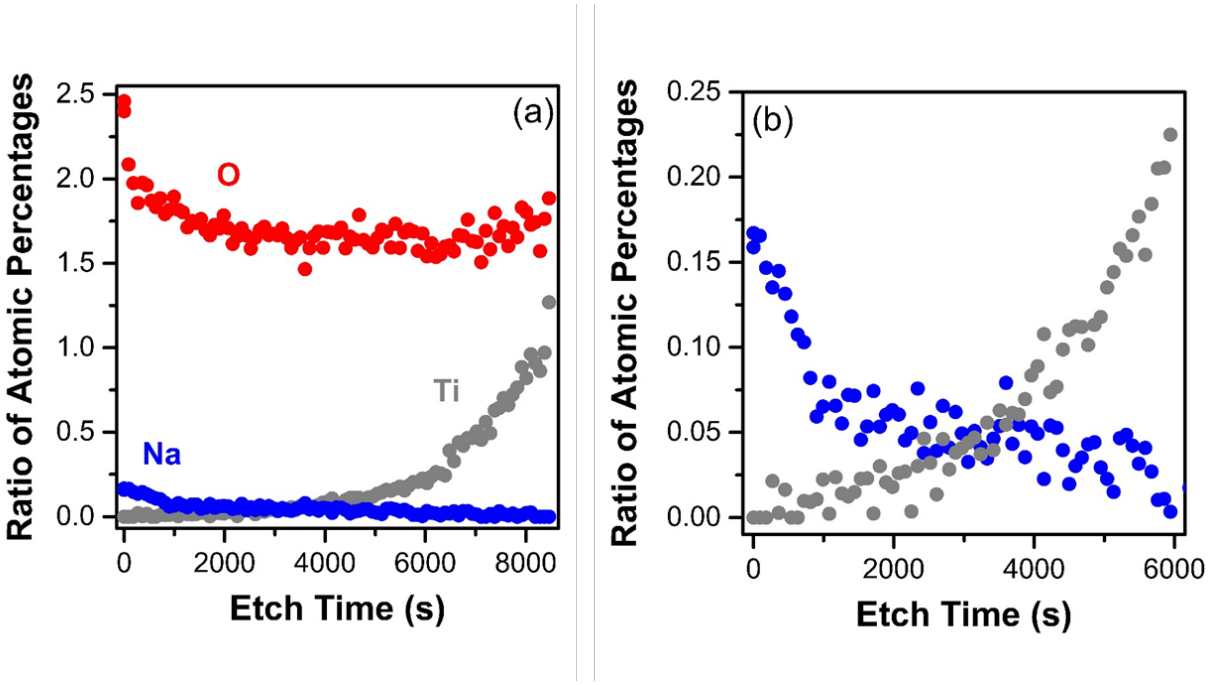

Figure 4.5 XPS depth profile of NMO reveals the composition of a NaxMnO2 film with an initial MnO ALD thickness of 817 Å. (a) Ratios of atomic percentages are given with respect to Mn. (b) A zoomed window of (a) highlighting the bulk Na concentration.

Together, XPS depth-profiling suggests a surface composition of $Na_{0.17}MnO_2$ and a bulk composition of $Na_{0.5}Mn_5O_8$.

Both surface and bulk compositions of our NMO films have a lower concentration of Na than the $Na_{0.44}MnO_2$ particles used in previous HCDI studies.[6,7,18–20] Additionally, O and Na concentrations in these films are lower than those of our previous work where electrochemical conversion was performed in $Na_2SO_{4(aq)}$. Films converted in Na_2SO_4 had a more uniform Na:Mn ratio of 0.25 and an O:Mn ratio of 2.[13] The discrepancy in elemental composition can be attributed to incomplete conversion of the film in the $NaCl_{(aq)}$ electrolyte used here. We suspect that $Cl^-_{(aq)}$ oxidation to $Cl_{2(g)}$ at 0.75 V vs. Ag/AgCl competes with oxidation of MnO to NMO at this pH during NMO formation. As shown in the following sections, incomplete conversion somewhat limits CSC of NMO oxidized in $NaCl_{(aq)}$ as compared to NMO oxidized in $Na_2SO_{4(aq)}$.[13] However, the presence of Na both at the surface and in the bulk of the NMO film support Na incorporation into the film during electrochemical oxidation in $NaCl_{(aq)}$ and suggest that, with some additional refinement, these NMO films could be effective for electrochemical removal of Na^+ in HCDI.

4.3C Optimizing NMO Film Thickness

To understand the depth to which charge storage occurs in NMO, we vary the thickness of the starting MnO film and evaluate the areal CSC of the resulting NMO films following electrochemical conversion in $NaCl_{(aq}$, as shown in Figure 4.6. The

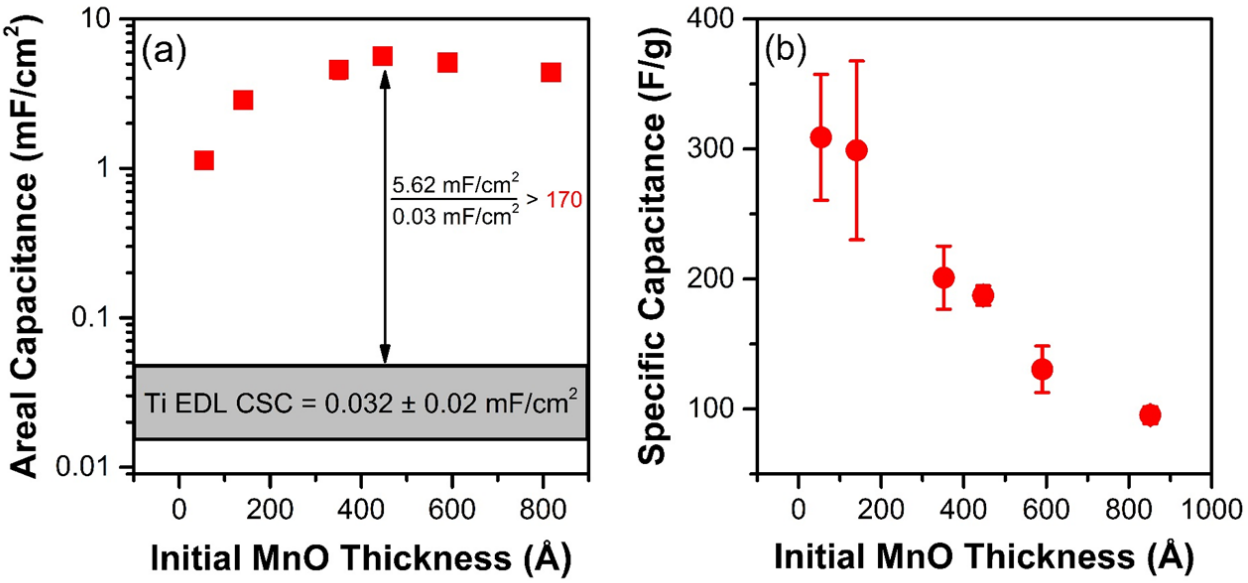

Figure 4.6 Capacitance measurements at a sweep rate of 20 mV/s of post-oxidized NMO films versus the starting film thickness of the pre-oxidized ALD MnO film normalized to (a) area of the film and (b) mass of the film.

ability to tune film thickness and thereby reduce unused bulk material also highlights the superiority of thin films over particulate NMO in these systems. As shown in Figure 4.6a, the areal CSC increases with the initial MnO film thickness, as more bulk material is available for charge storage. This behavior suggests that cation intercalation into the bulk of the film contributes little to the CSC. However, the areal CSC reaches an upper limit at an initial MnO thickness of 45 nm, after which thicker films do not provide additional charge storage.

The highest specific mass CSCs (F/g) are observed for the thinnest initial MnO ALD films, as shown in Figure 4.6b. Specific mass CSC values are normalized to a calculated mass of post-processed MnO_2, assuming complete conversion of MnO to MnO_2 and thickness of MnO ALD films as measured by spectroscopic ellipsometry. This is a conservative estimate considering the partial conversion observed by XPS in Figure 4.5. The highest specific mass CSC calculated was 309 ± 48 F/g at a sweep rate of 20 mV/s for films as thin as 5.4 nm. Specific mass CSC decreases with film thickness, indicating that the majority of charge storage occurs at or near the surface of the NMO film following conversion in $NaCl_{(aq)}$. The confinement of sodium insertion to the surface of these films is likely a product of the limited electrochemical conversion, as described above. More uniform charge storage throughout the thickness of the film may be achieved by converting films in $Na_2SO_{4(aq)}$, as previously described,[13] or by developing techniques for direct growth of NMO.

4.3D HCDI Using Thin-Film NMO

High surface area CNT electrodes were used for desalination testing. These electrodes ensure a large EDL and mimic the standard CDI cell configuration. We compare two configurations – a conventional CDI cell with symmetric CNT electrodes (CNT/CNT), and an HCDI cell with a NMO-coated CNT cathode and Ag-decorated CNT anode (NMO-CNT/Ag-CNT). The results of these tests are shown in Figure 4.7. The HCDI cathode was comprised of CNTs coated with 125 ALD cycles of MnO, electrochemically oxidized to NMO prior to cell assembly. The initial MnO coating was ~ 26 nm as measured by XRR on a silicon witness wafer. The 26 nm thickness is expected to provide both a large areal and specific CSC based on the results in Figure 4.6.

To study the effects of adding a high capacity material to the cathode for Na^+ insertion, as we have done here, the HCDI anode must have an equivalent capacity and rate for anion uptake during desalination experiments. A low capacity or kinetically slow anode will limit the cathode performance. To avoid imposing capacity or rate limits on the NMO-coated CNT cathode, an excess of Ag nanopowder was mixed into the CNT anode in the HCDI cell. Ag particles have been employed for Cl^- sorption electrodes in a number of earlier electrochemical studies.[5,6,35–37] Ag reacts with Cl^- ions under applied bias to form insoluble AgCl, according to

$$Ag_{(s)} + Cl^-_{(aq)} \rightarrow AgCl_{(s)} + e^-.$$

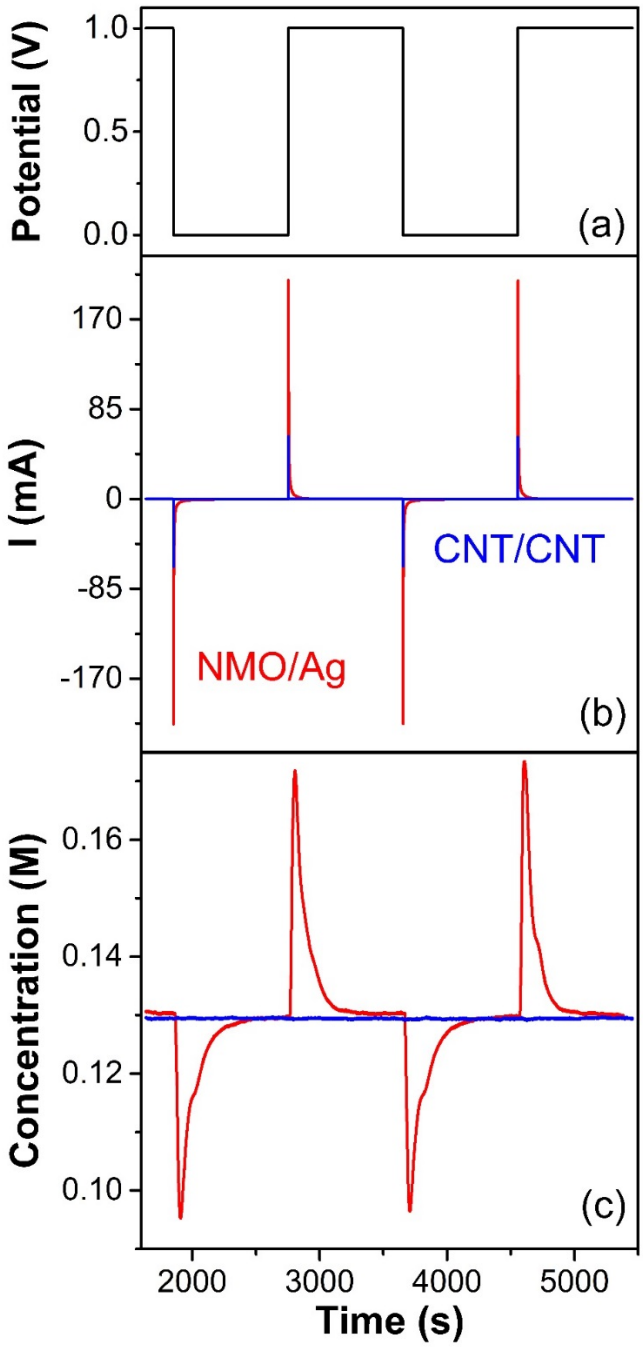

Figure 4.7 Plot of (a) potential, (b) current, and (c) effluent salt concentration versus time during electrochemical desalination for HCDI (NMO-CNT/Ag-CNT) and CDI (CNT/CNT) configurations.

We note that Ag is not a cost-effective HCDI anode material for scale-up. Additionally, AgCl formation has limited reversibility due to the increased electrical resistance of AgCl,[6] leading to a poor cycle lifetime. Despite its shortcomings, Ag is the most well-studied material for electrochemical anion incorporation in HCDI devices. We used Ag nanoparticles here to study NMO films as HCDI cathodes, and a molar excess was used to ensure that the cathode performance was not artificially limited.

Desalination tests were performed in a constant potential configuration. Potential was step-cycled between 0.0 and 1.0 V across the two-electrode cell. We note that the CDI and HCDI cells are expected to have different desalination profiles. In the CNT/CNT CDI configuration, desalination occurs during the 1.0 V half cycle and electrode regeneration occurs during the 0.0 V half cycle. However, in the NMO-CNT/Ag-CNT HCDI configuration, electrode regeneration occurs during the 1.0 V half cycle and desalination occurs during the 0.0 V half cycle, as depicted in Figure 4.1. During the 1.0 V half cycle, the nominal half reactions in the HCDI cell are

$$NaMn_4O_8 \longrightarrow Na^+_{(aq)} + e^- + Mn_4O_8$$

and

$$AgCl + e^- \longrightarrow Ag + Cl^-_{(aq)},$$

to yield the overall regeneration reaction

$$NaMn_4O_8 + AgCl \longrightarrow Mn_4O_8 + Ag + NaCl_{(aq)}.$$

During the 0.0 V half cycle, the nominal half reactions reverse to yield the overall desalination reaction

$$Mn_4O_8 + Ag + NaCl_{(aq)} \longrightarrow NaMn_4O_8 + AgCl.$$

For both cells, one cycle consisted of 1.0 V held for 15 minutes and 0.0 V held for 15 minutes for a total of 30 minutes per cycle. We note that cycle times were set to ensure sufficient time for complete desalination and regeneration for characterization purposes. Cycle times could be shortened in future operation to obtain precise rates of desalination. We report CSC and SSC values after eight charge-discharge conditioning cycles. At this point, salt sorption and desorption are within 4% variation, and are averaged over five cycles of desalination/regeneration. See Table 1 for salt sorption and charge transfer values for all five cycles. Electrode stability over hundreds of cycles is necessary for commercial desalination devices and is currently not achievable with the materials studied here under electrolyte flow, but is the subject of ongoing effort.

Table 1. Cycling Data of HCDI with NMO-CNT/Ag-CNT Cell

Cycle	Salt Sorption (mol NaCl x 10^{-5})	Salt Desorption (mol NaCl x 10^{-5})	Cathodic Charge (mol e- x 10^{-5})	Anodic Charge (mol e- x 10^{-5})
9	-1.57	1.61	-1.27	1.35
10	-1.67	1.70	-1.30	1.41
11	-1.62	1.63	-1.29	1.38
12	-1.51	1.48	-1.30	1.38
13	-1.59	1.53	-1.30	1.37

Consistent with results observed on flat electrodes, charge storage behavior is starkly different between the HCDI and CDI cells, as shown in Figure 4.7. During the 1.0 V half cycle, the CDI carbon electrode cell had an average capacity of 58.4 ± 0.9 mC. In contrast, the HCDI cell had an average capacity of 1.3380 ± 0.0200 C, a factor of ~23 increase in charge storage-capacity over the CDI cell. During the 0.0 V half-cycle, an even larger increase in charge storage over the CDI cell is observed. The CDI cell averages -21.3 ± 0.1 mC, while the HCDI cell averages -1.2459 ± 0.0123 C. The increase in charge storage during the 0.0 V half-cycle is 58 times greater in the HCDI cell than in the CDI cell. The advantage of the HCDI cell is also reflected in the coulombic efficiency of 93% for the HCDI cell versus 37% for the CDI cell over these five desalination cycles. The high coulombic efficiency of the HCDI cell suggests a reversible process with a low net energy consumption.

The stark increase in CSC in the HCDI cell is reflected by an increase in SSC, as seen in the concentration profile of the effluent solution during cycling in Figure 4.7. For the HCDI cell, we observe dramatic changes in the effluent salt concentration with transient decreases in salt concentration of > 0.03 M below the inlet salt concentration. In contrast, differences in salt concentration are below the detection limit of the conductivity meter for the CDI cell. In the HCDI cell, 0.93 ± 0.03 mg of salt was removed per cycle during the 0 V step.

We expect the CSC of the cathode to be ~250 F/g, based on the 26 nm thickness of the MnO coating on a silicon witness wafer and the specific capacity results in Figure 4.6b. For a 1V charging potential, this is equal to 69.4 mAh/g. Based on this CSC, the theoretical SSC of the NMO is 151 mg_{NaCl} $(g_{NMO})^{-1}$. With an anode of equivalent CSC to our NMO-based cathode, the normalized SSC would be ~ 75 mg g^{-1}, a value well above the highest reported HCDI SSC.[7] Assuming a conformal MnO film on the CNT-OH powder with 200 m^2/g surface area and 100% conversion to NMO, the mass of NMO in the HCDI cathode is estimated to be 87 mg. We expect the actual mass loading to be lower than this due to diffusion limitations of the gas phase precursors into the CDI electrodes, and mass loss during the electrochemical conversion to NMO. The average measured amount of salt removed in the HCDI cell was 0.93 ± 0.03 mg per cycle. Assuming an NMO mass of 87 mg yields an experimental SSC of 11 ± 0.3 mg_{NaCl} $(g_{NMO})^{-1}$. Normalizing experimental salt removal to the mass of both electrodes (a CDI convention) yields a SSC of 5.6 ± 0.2 mg_{NaCl} $(g_{total\ electrode})^{-1}$ for the HCDI cell, a value lower than the highest reported for an HCDI system (31.2 mg_{NaCl} $(g_{electrode})^{-1}$) and for a conventional CDI system (14.9 mg_{NaCl} $(g_{electrode})^{-1}$).[7,38] These relatively low values might be due to (1) incomplete coating of the CNT-OHs, (2) incomplete conversion to NMO, and (3) the large overpotential to regenerate Ag from AgCl. A higher SSC may be achieved with further optimization of the deposition and conversion processes, as well as the use of an easily regenerated high capacity anode.

Despite these low SSC values, our HCDI cell shows high charging efficiency (Λ) values. Λ (mol NaCl/mol e^-) values are conventionally below 100% in CDI literature. In our HCDI cell, we measure surprisingly high Λ values of 123 ± 5% for the 0 V half-cycle (desalination), and 115 ± 6% for the 1.0 V half-cycle (regeneration) over five cycles of charge/discharge. For comparison, the highest reported Λ value for a HCDI system using NMO is 82%, and for a CDI system is close to unity.[19,39] These anomalously high Λ values are reversible on both charge and discharge steps over multiple cycles.

We examined a range of common experimental artifacts and known physical phenomena which could potentially contribute to these high charging efficiencies, but these factors did not account for the charging behavior we observed. We considered, for instance, (1) reduced co-ion expulsion arising from high ion-selectivity of the electrode materials, (2) progressive wetting, (3) static charge build up in the electrodes before operation, (4) side reactions, for example to form Cl_2, and (5) decomposition of manganese oxide during cycling leading to flocculation and removal of ions.[3,40–43] However, none of these alternative effects or combinations thereof satisfactorily explain the behavior we observe.

Reduced co-ion expulsion could explain Λ approaching 100%,[3,4,44] but does not account for $\Lambda > 100\%$. Static charge build-up and progressive wetting are expected to dissipate during the pretreatment procedures we describe above (overnight soaking in electrolyte and seven forming cycles) and are not expected to remain during cycles 8-13

as we observe. Furthermore, irreversible processes like progressive wetting, static charge build-up, Cl_2 formation, or flocculant formation would be expected to result in $\Lambda > 100\%$ for only one half cycle (either charge or discharge) yielding low coulombic efficiencies, whereas we observe $\Lambda > 100\%$ for both charge and discharge cycles over five cycles with coulombic efficiencies of 93%. In an effort to understand this high efficiency, we employed EQCM, as discussed in the following, and *ab initio* modeling, as described elsewhere.[45]

4.3E The Relationship between Charge Storage and Ion Removal in NMO

EQCM was used to probe the contribution of reversible Na^+ sorption to the CSC of NMO. In EQCM, a quartz crystal serves as both mass sensor and working electrode. EQCM results for a ~ 40 nm thick NMO film in 0.10 M $NaCl_{(aq)}$ electrolyte are shown in Figure 4.8 during CV operation. These results reveal a mass loss associated with an anodic current, as potential is swept from 0 to 0.9 V vs Ag/AgCl, and a mass gain associated with a cathodic current, as potential is reversed and swept from 0.9 to 0 V vs Ag/AgCl. This behavior is qualitatively consistent with cation insertion into the NMO film as identified above with XPS and HCDI testing, and is also consistent with previous work from our group on electrochemical Na^+ insertion in NMO.[13] We note that the only ions in solution are Na^+ and Cl^- and the experiments were carried out at a circumneutral pH. Therefore, we expect that the cation mediated charge storage we observe arises from Na^+.

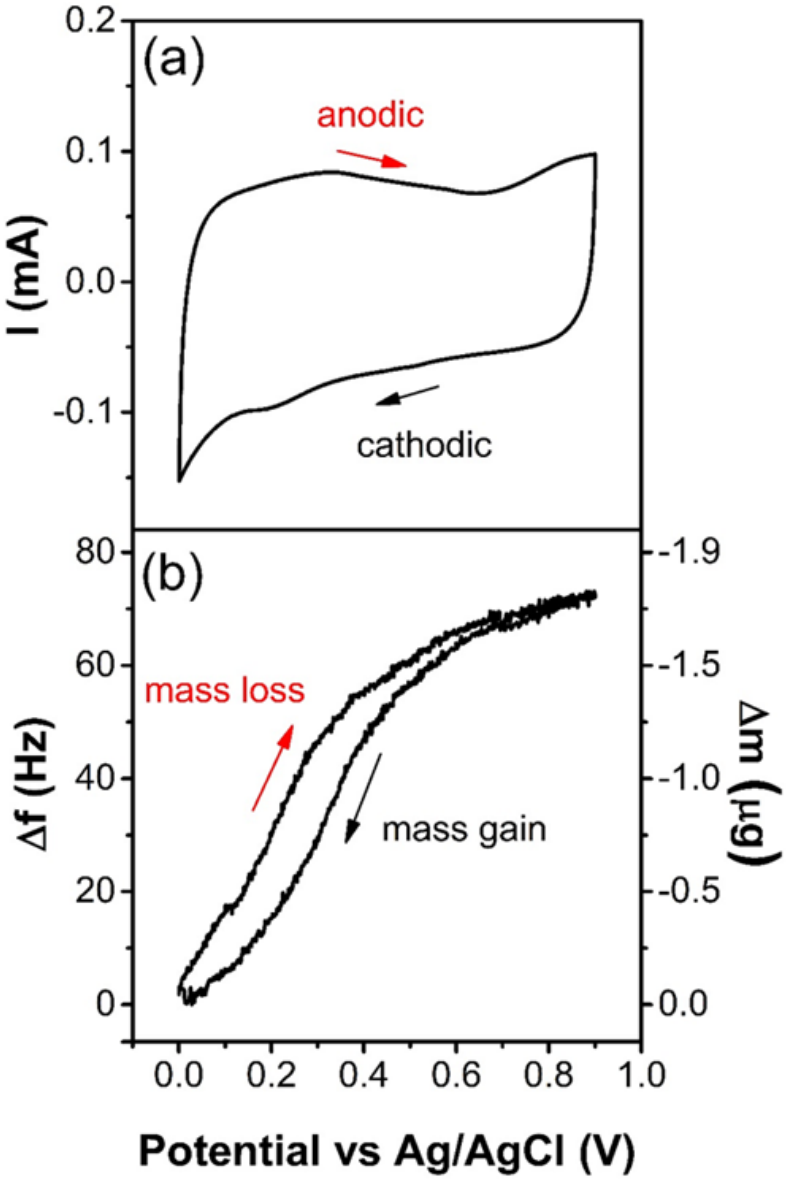

Figure 4.8 (a) CV measured during EQCM of 400 ALD cycles of MnO oxidized to NMO, performed at 20 mV/s in 0.1 M NaCl, (b) EQCM frequency shifts indicate a reversible mass gain as the potential sweeps negatively and a mass loss as the potential sweeps back positively.

We further evaluated our EQCM data to quantitatively compare the changes in mass and charge during CV measurements. Mass changes were calculated from shifts in the EQCM resonance frequency. Charge was calculated from the integral under the CV curve. The total charge transferred, Q, while sweeping over a potential range, ΔV, is calculated as $Q = CSC \times \Delta V$, where $\Delta V = 0.9$ V. A mass-to-charge ratio is calculated by taking the mass change on the oxidizing sweep from Figure 4.8b divided by the charge transferred during the oxidizing sweep in Figure 4.8a. For stoichiometric incorporation of Na^+, with one electron transferred per ion sorbed the normalized mass-to-charge ratio measured by EQCM is expected to correspond to the molar mass of Na^+ (23 g/(mol e^-)). However, we measure larger mass-to-charge ratios. Over the entire 0.9 V cycling window we measure an average mass-to-charge ratio of 49 g (mol e^-)$^{-1}$.

In Figure 4.8a we observe a relatively constant current of ~ 0.08 mA over the full potential range from 0 – 0.9 V vs. Ag/AgCl. However, we observe two distinct regions in the EQCM plot in Figure 4.8b. From 0.0 – 0.4 V vs Ag/AgCl, we observe a slope of 3.0 μg/V in Figure 4.8b, corresponding to a mass-to-charge ratio of 68 g (mol e^-)$^{-1}$. In contrast, from 0.5 – 0.9 V vs Ag/AgCl, we observe a slope of 0.8 μg/V in Figure 4.8b, corresponding to a lower mass-to-charge ratio of 17 g (mol e^-)$^{-1}$.

In our prior work, we attributed measured EQCM mass-to-charge ratios exceeding 23 g/(mol e^-) in NMO to non-ideal Sauerbrey behavior arising from viscoelastic dissipation in the NMO films.[13] However, the anomalously high

desalination charging efficiency measured for these NMO electrodes during HCDI testing, as detailed below, caused us to reevaluate this assumption and identify an alternative explanation — namely electron decoupled ion transfer (EDIT) in NMO. To help understand what gives rise to the two distinct regions of the slope measured by EQCM in Figure 4.8b we used *ab initio* modeling. Further details and results of modeling this system are presented in Wallas, J. M et al. *J. Electrochem. Soc.* **2018**, 165, A2330-A23339.

When coupled with these *ab initio* predictions, the EQCM results presented in Figure 4.8 suggest that the EDIT mechanism may be occurring in NMO. In Figure 4.8, we cycle the potential from 0-0.9 V vs. Ag/AgCl and measure an average mass-to-charge ratio of 49 g $(\text{mol } e^-)^{-1}$ by EQCM, corresponding to 2.1 Na^+/e^-. Over a narrower potential window of 0 – 0.4 V vs. Ag/AgCl this mass-to-charge ratio is even higher, corresponding to 3.0 Na^+/e^-. In comparison, an uncoated EQCM electrode exhibits sub-stoichiometric sorption of 0.5 Na^+/e^- (Figure 4.9), which we attribute to the formation of the EDL.

For the NMO electrode, over this potential range we expect to observe the superposition of (1) the formation of the EDL at the surface of the NMO and CNTs, (2) conventional faradaic intercalation of Na^+ into bulk NMO, (3) the EDIT mechanism in near-surface NMO. For conventional faradaic intercalation, a mass-to-charge ratio of 23 g $(\text{mol } e^-)^{-1}$, or 1 Na^+/e^- is expected. The value of 2.1 Na^+/e^- we measure by EQCM

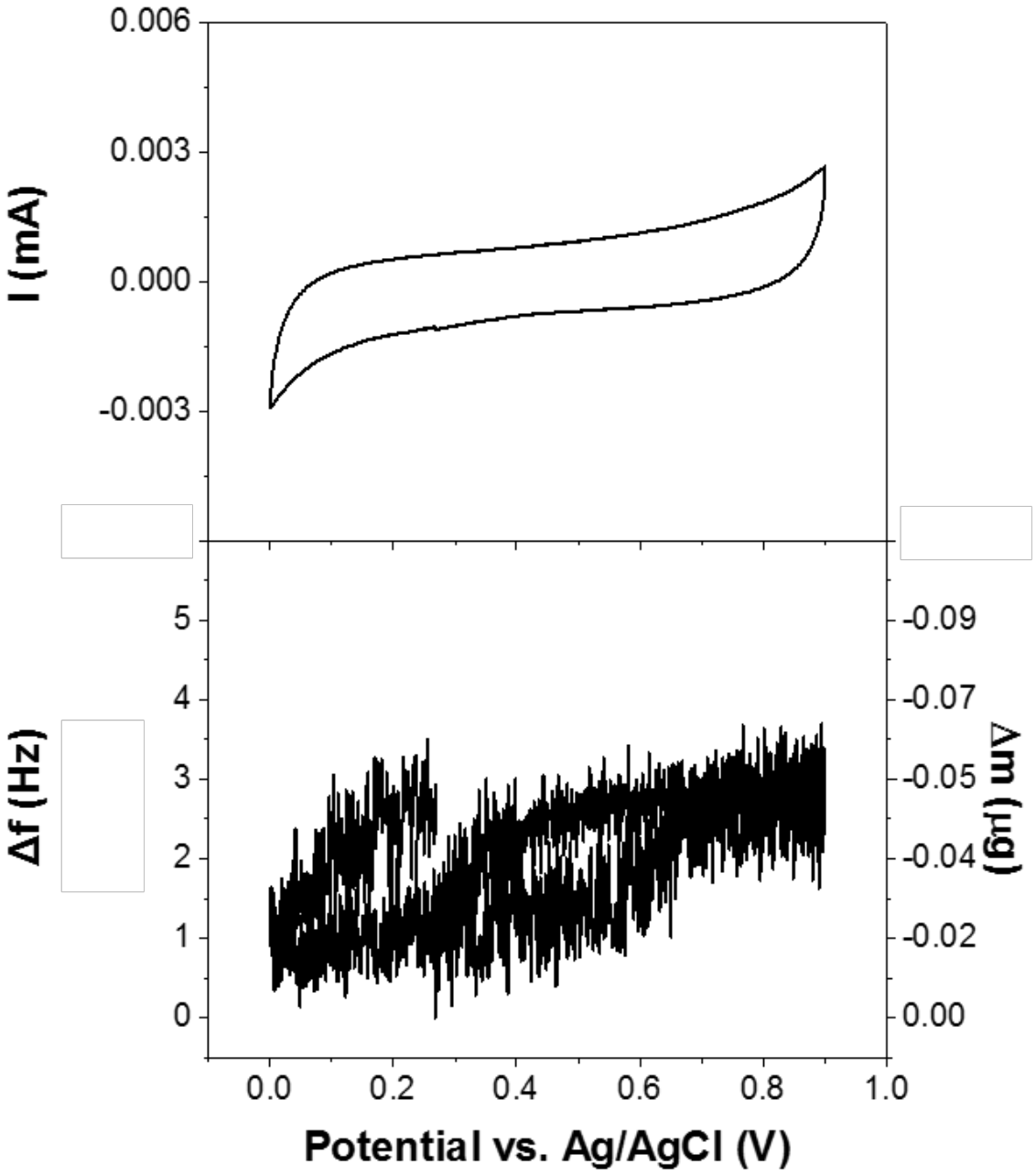

Figure 4.9 Cyclic voltammetry of an uncoated EQCM electrode at a scan rate of 5mV/s in 0.10 M NaCl(aq) using a three-electrode setup.

suggests that EDIT may contribute in the potential range of 0 – 0.9 V vs. Ag/AgCl in our system. In the potential range where EDIT is predicted to dominate (0.2 – 0.4 V vs. Ag/AgCl), we observe the largest mass-to-charge ratio, corresponding to 3.0 Na^+/e^-. The *ab initio* description of EDIT provides an explanation for the EQCM results and the high HCDI efficiency we observe.

The EDIT mechanism, and corresponding values of $\Lambda > 100\%$ that we observe are surprising. In CDI literature, Λ is assumed to have a theoretical maximum of 100%, and co-ion desorption is assumed to give rise to values consistently < 100%.[44,46,47] However, by our understanding, the limit of $\Lambda \leq 100\%$ is not rooted in a thermodynamic barrier, but in an assumption of charge balance.

We note that the EDIT mechanism we propose is predicted to be restricted to the surface of NMO and is expected to have a limited contribution in bulk NMO. Because our work uses thin films of NMO, there is an increased contribution from EDIT over other experimental studies using larger-size NMO particles. EDIT may also help explain larger-than-stoichiometric mass-to-charge ratios which have been noted in other nanoscale materials during electrochemical operation, including thin-film MnO_2[13] and nanoporous carbon.[48,49] In these prior studies, charge balance was assumed apriori, and anomalous mass-to-charge ratios were attributed to solvent or dissipation effects. Here, we were able to more directly probe the origin of these effects with simultaneous electrochemical measurements and effluent salt concentration measurements in a flow

configuration. This measurement capability allowed us to identify behavior consistent with EDIT.

The EDIT behavior our data supports may bring into question the apriori assumption of local charge balance for cation insertion electrochemistry in a larger sense. Charge self-regulation in transition metal semiconductors[50–53] is expected to be able to stabilize electronic and/or ionic charge in host structures, giving rise to EDIT behavior. Ultimately, our work suggests that the ion and electron transfer should be examined independently in transition-metal semiconductors. Our work also calls for further study of transition metal semiconductor electrochemistry in a range of electrochemical applications to evaluate the possibility of decoupled electron and ion transfer.

In the current work, we demonstrate a valuable set of experimental tools for understanding these effects. However, further experimental tools should be developed to independently probe mass and charge changes in electrode materials and electrolytes during electrochemical cycling. By harnessing and enhancing the EDIT effect with improved cycling stability, we expect to achieve new levels of efficiency and rate in electrochemical desalination.

4.4 Conclusions

In this work we demonstrate the successful conversion of thin-film MnO to electrochemically active NMO in $NaCl_{(aq)}$. XPS results indicate that conversion to NMO in $NaCl_{(aq)}$ is limited to the near-surface. Despite this, NMO films formed in $NaCl_{(aq)}$ exhibit charge storage capacities up to 170 times higher than uncoated electrodes. We observe the highest specific mass capacitances for the thinnest films, with values of ~300 F/g measured for 5.4 and 14.0 nm films. The highest areal capacitance of 5.62 mF/cm^2 was measured for a 44.8 nm film thickness. These results suggest that, with further optimization, HCDI devices could be deployed with electrodes coated with 5-50 nm MnO films, which can be converted *in operando* in water containing NaCl to form NMO for enhanced desalination performance.

We also report on an initial study of the desalination performance of thin film NMO. We study early cycling data of an HCDI cell comprised of a NMO-coated CNT cathode and an Ag nanoparticle-decorated CNT anode. We compare this HCDI cell to a CDI cell comprised of symmetric CNT electrodes that model conventional CDI operation. The HCDI configuration exhibits a >20-fold increase in charge storage and dramatically improves desalination performance compared to the symmetric CDI configuration. We also observe an anomalously high charging efficiency (mol NaCl (mol e-)$^{-1}$) of up to 123 ± 5%, which cannot be explained by experimental artifacts or known physical phenomena. This charging efficiency of $\Lambda > 100\%$ is unprecedented, and if validated,

harnessed and refined for use in full-scale HCDI devices, promises to enable new levels of energy efficient desalination.

Additionally, EQCM results support the high charging efficiency we measure in desalination tests. Over the potential range of 0 – 0.9 V vs. Ag/AgCl, EQCM data suggests the removal of 2.1 Na^+/e^-, with as many as 3.0 Na^+/e^- removed over the range of 0 – 0.4 V vs. Ag/AgCl. This behavior is corroborated by *ab initio* computational results described elsewhere,[45] capturing a phenomenon we term electron-decoupled ion transfer, or "EDIT." EDIT is predicted to occur at the surface of NMO, and is enhanced in the thin-film NMO coatings used in this work. The EDIT mechanism challenges the common assumption of local charge balance in HCDI electrodes. If the EDIT mechanism proves correct, then this mechanism could enable unforeseen levels of energy efficiency in HCDI. We suggest that this mechanism may also be at play in other ion-insertion electrode materials, and that new materials could be designed to enhance this effect for improved HCDI efficiency.

4.5 References

(1) Jury, W. A.; Vaux, H. *Proc. Natl. Acad. Sci. U. S. A.* **2005**, *102* (44), 15715–15720.

(2) LIGTT. *50 Breakthroughs: Critical scientific and technological advances needed for sustainable global development*; LBNL Institute for Globally Transformative Technologies: Berkeley, CA, 2014.

(3) Porada, S.; Zhao, R.; van der Wal, A.; Presser, V.; Biesheuvel, P. M. *Prog. Mater. Sci.* **2013**, *58* (8), 1388–1442.

(4) Suss, M. E.; Porada, S.; Sun, X.; Biesheuvel, P. M.; Yoon, J.; Presser, V.; Biesheuvel, M.; Yoon, J.; Presser, V. *Energy Environ. Sci.* **2015**, *8* (8), 2296–2319.

(5) La Mantia, F.; Pasta, M.; Deshazer, H. D.; Logan, B. E.; Cui, Y. *Nano Lett.* **2011**, *11* (4), 1810–1813.

(6) Pasta, M.; Wessells, C. D.; Cui, Y.; La Mantia, F. *Nano Lett.* **2012**, *12* (2), 839–843.

(7) Lee, J.; Kim, S.; Kim, C.; Yoon, J. *Energy Environ. Sci.* **2014**, *7* (11), 3683–3689.

(8) Conway, B. E. *J. Electrochem. Soc.* **1991**, *138* (6), 1539–1548.

(9) Cao, Y.; Xiao, L.; Wang, W.; Choi, D.; Nie, Z.; Yu, J.; Saraf, L. V.; Yang, Z.; Liu, J. *Adv. Mater.* **2011**, *23* (28), 3155–3160.

(10) Van Nghia, N.; Ou, P.-W.; Hung, I.-M. *Electrochim. Acta* **2015**, *161*, 63–71.

(11) Guo, S.; Yu, H.; Jian, Z.; Liu, P.; Zhu, Y.; Guo, X.; Chen, M.; Ishida, M.; Zhou, H. *ChemSusChem* **2014**, *7* (8), 2115–2119.

(12) Young, M. J.; Holder, A. M.; George, S. M.; Musgrave, C. B. *Chem. Mater.* **2015**, *27* (4), 1172–1180.

(13) Young, M. J.; Neuber, M.; Cavanagh, A. C.; Sun, H.; Musgrave, C. B.; George, S. M. *J. Electrochem. Soc.* **2015**, *162* (14), A2753–A2761.

(14) Mai, L.; Li, H.; Zhao, Y.; Xu, L.; Xu, X.; Luo, Y.; Zhang, Z.; Ke, W.; Niu, C.; Zhang, Q. *Sci. Rep.* **2013**, *3*, 1718.

(15) Simon, P.; Gogotsi, Y. *Nat. Mater.* **2008**, *7* (11), 845–854.

(16) Yuan, Y.; Zhan, C.; He, K.; Chen, H.; Yao, W.; Sharifi-Asl, S.; Song, B.; Yang, Z.;

Nie, A.; Luo, X.; Wang, H.; Wood, S. M.; Amine, K.; Islam, M. S.; Lu, J.; Shahbazian-Yassar, R. *Nat. Commun.* **2016**, *7*, 13374.

(17) Chen, D.; Ding, D.; Li, X.; Waller, G. H.; Xiong, X.; El-Sayed, M. A.; Liu, M. *Chem. Mater.* **2015**, *27* (19), 6608–6619.

(18) Smith, K. C.; Dmello, R. *J. Electrochem. Soc.* **2016**, *163* (3), A530–A539.

(19) Yang, J.; Zou, L.; Song, H.; Hao, Z. *Desalination* **2011**, *276* (1–3), 199–206.

(20) Yang, J.; Zou, L.; Song, H. *Desalination* **2012**, *286*, 108–114.

(21) Toupin, M.; Brousse, T.; Bélanger, D. *Chem. Mater.* **2004**, *16* (16), 3184–3190.

(22) Yan, W.; Kim, J. Y.; Xing, W.; Donavan, K. C.; Ayvazian, T.; Penner, R. M. *Chem. Mater.* **2012**, *24* (12), 2382–2390.

(23) Jung, Y. S.; Cavanagh, A. S.; Riley, L. A.; Kang, S.-H.; Dillon, A. C.; Groner, M. D.; George, S. M.; Lee, S.-H. *Adv. Mater.* **2010**, *22* (19), 2172–2176.

(24) *Seawater Corrosion Handbook*; Schumacher, M., Ed.; Noyes Data Corporation: Park Ridge, New Jersey, 1979.

(25) Burton, B. B.; Fabreguette, F. H.; George, S. M. *Thin Solid Films* **2009**, *517* (19), 5658–5665.

(26) Martin, S. J.; Granstaff, V. E.; Frye, G. C. *Anal. Chem.* **1991**, *63* (20), 2272–2281.

(27) Martin, S. J.; Spates, J. J.; Wessendorf, K. O.; Schneider, T. W.; Huber, R. J. *Anal. Chem.* **1997**, *69* (11), 2050–2054.

(28) Porada, S.; Bryjak, M.; van der Wal, A.; Biesheuvel, P. M. *Electrochim. Acta* **2012**, *75*, 148–156.

(29) Porada, S.; Borchardt, L.; Oschatz, M.; Bryjak, M.; Atchison, J. S.; Keesman, K. J.; Kaskel, S.; Biesheuvel, P. M.; Presser, V. *Energy Environ. Sci.* **2013**, *6* (12), 3700–3712.

(30) Yang, S.; Jeon, S.; Kim, H.; Choi, J.; Yeo, J.; Park, H.; Kim, D. K. *ACS Sustain. Chem. Eng.* **2016**, *4* (8), 4174–4180.

(31) Cavanagh, A. S.; Wilson, C. A.; Weimer, A. W.; George, S. M. *Nanotechnology* **2009**, *20* (25), 255602.

(32) Ferguson, J. .; Weimer, A. .; George, S. . *Thin Solid Films* **2000**, *371* (1), 95–104.

(33) McCormick, J. A.; Cloutier, B. L.; Weimer, A. W.; George, S. M. *J. Vac. Sci. Technol. A Vacuum, Surfaces, Film.* **2007**, *25* (1), 67–74.

(34) Zydor, A.; Elliott, S. D. *J. Phys. Chem. A* **2010**, *114* (4), 1879–1886.

(35) Pasta, M.; Battistel, A.; La Mantia, F. *Energy Environ. Sci.* **2012**, *5* (11), 9487–9491.

(36) Lee, J.; Yu, S.-H.; Kim, C.; Sung, Y.-E.; Yoon, J. *Phys. Chem. Chem. Phys.* **2013**, *15* (20), 7690–7695.

(37) Kim, S.; Lee, J.; Kim, C.; Yoon, J. *Electrochim. Acta* **2016**, *203*, 265–271.

(38) Porada, S.; Weinstein, L.; Dash, R.; van der Wal, A.; Bryjak, M.; Gogotsi, Y.; Biesheuvel, P. M. *ACS Appl. Mater. Interfaces* **2012**, *4* (3), 1194–1199.

(39) Kim, T.; Dykstra, J. E.; Porada, S.; van der Wal, A.; Yoon, J.; Biesheuvel, P. M. *J. Colloid Interface Sci.* **2015**, *446*, 317–326.

(40) Rica, R. A.; Ziano, R.; Salerno, D.; Mantegazza, F.; Brogioli, D. *Phys. Rev. Lett.* **2012**, *109* (15), 156103.

(41) Franceschetti, D. R.; Macdonald, J. R. *J. Appl. Phys.* **1979**, *50* (1), 291–302.

(42) Murray, J. W. *J. Colloid Interface Sci.* **1974**, *46* (3), 357–371.

(43) Balistrieri, L. S.; Murray, J. W. *Geochim. Cosmochim. Acta* **1982**, *46* (6), 1041–1052.

(44) Avraham, E.; Bouhadana, Y.; Soffer, A.; Aurbach, D. *J. Electrochem. Soc.* **2009**, *156* (6), 95–99.

(45) Wallas, J. M.; Young, M. J.; Sun, H.; George, S. M. *J. Electrochem. Soc.* **2018**, *165* (10), A2330–A2339.

(46) Biesheuvel, P. M. *J. Colloid Interface Sci.* **2009**, *332* (1), 258–264.

(47) Zhao, R.; Biesheuvel, P. M.; Miedema, H.; Bruning, H.; van der Wal, A. *J. Phys. Chem. Lett.* **2010**, *1* (1), 205–210.

(48) Tsai, W.-Y.; Taberna, P.-L.; Simon, P. *J. Am. Chem. Soc.* **2014**, *136* (24), 8722–8728.

(49) Levi, M. D.; Levy, N.; Sigalov, S.; Salitra, G.; Aurbach, D.; Maier, J. *J. Am. Chem. Soc.* **2010**, *132* (38), 13220–13222.

(50) Haldane, F. D. M.; Anderson, P. W. *Phys. Rev. B* **1976**, *13* (6), 2553–2559.

(51) Wolverton, C.; Zunger, A. *Phys. Rev. Lett.* **1998**, *81* (3), 606–609.

(52) Raebiger, H.; Lany, S.; Zunger, A. *Nature* **2008**, *453* (7196), 763–766.

(53) Padilha, A. C. M. M.; Raebiger, H.; Rocha, A. R.; Dalpian, G. M. *Sci. Rep.* **2016**, *6*, 28871.

5. Atomic Layer Deposition of Yttrium Fluoride and Yttrium Oxyfluoride with Tunable Stoichiometry

Jasmine M. Wallas,[1] Jessica A. Murdzek,[1] Diane K. Lancaster,[1]

Andrew S. Cavanagh,[1] Xiaowei Wu,[2] Jennifer Sun,[2] and Steven M. George[1*]

[1]*Department of Chemistry, University of Colorado, Boulder, Colorado 80309*

[2]*Applied Materials, 1140 E Arques Avenue, Sunnyvale, California 94085*

5.1 Introduction

Fabrication of semiconductor devices relies on the use of reactive plasmas for several processes, such as dry etching and chamber cleaning. Over time, these plasmas react with chamber walls and components, changing their properties. These changes can affect plasma etch rates and uniformity over time, which in turn can affect wafer-to-wafer reproducibility.[1] The changes caused by reactive plasmas also affect the integrity of the chamber walls and components. As a result, plasma chambers can suffer from more frequent and longer maintenance downtimes, leading to higher operating costs.

Recently, yttrium-based materials have been studied as corrosion-resistant barriers against many of the reactive plasmas used in semiconductor processing. Y_2O_3 has been well studied as a protective coating against many reactive plasmas, such as CF_4, SF_6, Cl_2, $SiCl_4$, NF_3 and O_2 plasmas.[2–4] Compared with Al_2O_3 and AlF_3, Y_2O_3 shows superior resistance to etching. Recent studies have also shown that YF_3 and YOF have

excellent corrosion resistance against many reactive plasmas.[5] YF_3 and YOF may act as better corrosion-resistant protective coatings in plasma chambers using F-containing plasmas, while Y_2O_3 may act as a better protective coating against O-containing plasmas.

There are several conditions that must be met for yttrium-based coatings to act as superior corrosion-resistant barriers in plasma chambers. First, the coating process must deposit a film without line-of-sight transfer so that the entire interior of the chamber can be coated. Methods that use line-of-sight deposition, such as physical vapor deposition (PVD) would not be appropriate for this task. Second, the coating must be conformal and pin-hole free on the complex, high-aspect ratio components used in the chamber. Third, the coating must be thin so that any thermal-expansion mismatch between the coating and component material is mitigated. Atomic layer deposition (ALD) is a specialized coating process that can meet all of these needs.

ALD processes for some yttrium-based thin films have been developed. There are reports on a Y_2O_2S ALD system, a YF_3 ALD system and several on Y_2O_3 ALD systems. Y_2O_3 ALD systems have been developed with high growth rates, reasonable deposition temperatures, and low levels of impurities using several different precursor systems.[6–12] In contrast, there is only one report on YF_3 ALD.[13] This YF_3 system used the precursors tris(2,2,6,6-tetramethyl-3,5-heptanedione) yttrium and TiF_4. Though this YF_3 ALD had a high growth rate (1.1 – 1.7 Å/cycle) and a wide temperature range (175 – 323

°C), the films it produced also had high surface roughness and contained O, C, and Ti impurities. The metal impurity present in the YF_3 thin films deposited with this ALD system make this approach unsuitable for use in semiconductor processing.

In this study, ALD thin films of YF_3 and YO_xF_y with tunable stoichiometry were developed. Tris(butylcyclopentadienyl) yttrium [$Y(CpBt)_3$] was used as the yttrium precursor. H_2O and HF-pyridine were used as the oxygen and fluorine precursors, respectively. The films deposited in this study had high densities, low surface roughness, and low levels of impurities. Typically, a simple nanolaminate approach is used to deposit ALD films containing more than two precursors.[14] We found that it was not possible to use this approach to grow YO_xF_y films because of 1) the favorability of the fluorine exchange reaction between HF and Y_2O_3, and 2) the depth of diffusion of F into Y_2O_3. In this study, YO_xF_y films were deposited using a super-cycle approach, combining intervals of Y_2O_3 deposition with periodic HF exposures. Using this approach, we were able to deposit several distinct YO_xF_y films.

5.2 Experimental Methods

Depositions were performed in a custom-built hot-walled viscous flow reactor. Ar (Airgas, prepurified) was used as the carrier gas at a total flow rate of 445 sccm. Two mass flow controllers (Type 1179A, MKS) were used to control this flow rate. Two separate precursor dosing lines separated oxidants and metal precursors. Ar flow was

split unequally, with 97 sccm flowing across the oxidant line and 348 sccm flowing across the metal precursor line. The base pressure in the reactor was ~2.5 Torr. Pressure was monitored with a capacitance manometer (Baratron 121A, MKS). Vacuum in the reactor was created using a mechanical pump. The reactor temperature was maintained at 225 ˚C ± 0.04 °C using a PID temperature controller (2604, Eurotherm). The metal precursor was tris(butylcyclopentadienyl) yttrium (Y(CpBt)3) (99.9 %, Strem Chemicals). The O precursor, H_2O (HPLC grade, Sigma Aldrich), was dosed using a vapor draw configuration at room temperature. The F precursor, HF-pyridine (70 wt. %, Sigma Aldrich), was used in the same configuration.

In situ mass changes during deposition were monitored with a quartz crystal microbalance (QCM) (Maxtek TM-400, Inficon). The crystal, a 6 MHz AT-cut crystal (Colorado Crystal Corp.), was held in a single sensor holder (BSH-150, Inficon) sealed with a high-temperature conductive epoxy (Epo-Tek H21D, Epoxy Technology). An additional ~20 sccm of Ar carrier gas was flowed through the QCM housing to prevent back-side deposition.

Ex situ thickness measurements were performed using X-ray reflectivity (XRR) (Bede D1, Jordan Valley Semiconductors) and spectroscopic ellipsometry (SE) (Model M-2000, J. A. Woollam Co., Inc.). For XRR, a high-resolution X-ray was used with a Cu Kα X-ray source (λ = 1.540 Å). The step size was 10 arcseconds and acquisition time was 10 seconds. Bede REFS software package (Jordan Valley Semiconductors) was used to

model the XRR data. Grazing-Incidence X-ray diffraction (GIXRD) was also measured on this X-ray diffractometer instrument. SE was used to determine thickness and index of refraction, n, and extinction coefficient, k. SE data was modelled using the CompleteEASE software package (J. A. Woollam Co., Inc.).

Compositional analysis was performed with X-ray photoelectron spectroscopy (XPS) (PHI 5600, RBD Instruments). A monochromatic Al-Kα (1486.6 eV) X-ray source was used. Depth profiling was performed with Ar^+ sputtering. The pass energy was 29.35 eV, and the step size was 0.25 eV. Data was collected with the AugerScan software package (RBD Instruments) and analyzed with the CasaXPS software package (Casa Software).

5.3 Results and Discussion

Deposition of the yttrium precursor, $Y(CpBt)_3$, is difficult because of its high molecular weight, 452.50 amu, and its low vapor pressure. Several reactor modifications were made so that a sufficiently large dose of the precursor could be delivered into the reactor and so that the precursor could be effectively purged out of the reactor. To deliver a sufficiently large dose, the precursor was heated to 170 ˚C and a flow-over dosing configuration was used, i.e. purge gas was redirected over the headspace of the precursor during each dose. To effectively purge the precursor, we used Ar gas instead

of N_2 because it is slightly heavier (18 vs. 14 amu). We set a high flow rate of the purge gas of 320 sccm.

5.3A YF_3 ALD

QCM measurements of YF_3 deposition show very linear growth over many deposition cycles. Figure 5.1 shows 100 cycles of YF_3 deposition on a quartz crystal coated with 300 cycles of Al_2O_3 ALD at 225 ˚C. The dose times for $Y(CpBt)_3$ and HF-pyridine were 0.3 and 1 second, respectively, with 30 second purge times between each precursor dose. A shorthand that we will use in this paper for dosing profiles is: (0.3, 30, 1, 30). The dose pressure of the HF-pyridine was 55 mTorr. The dose pressure of the $Y(CpBt)_3$ is unknown because of the flow-over dosing configuration used. The mass gain per cycle (MGPC) of YF_3 ALD measured over the 100 cycles shown in Figure 5.1 is 22 ng cm^{-2} $cycle^{-1}$. Initial nucleation on the Al_2O_3 surface is favorable, with larger mass gains over the first three cycles. YF_3 deposition is an ideal ALD process with short precursor dose times and reasonable purge times.

The idealness of YF_3 ALD is shown in the staircase-like growth and flat plateaus shown in a closer look at the QCM data. Figure 5.2 shows cycles 75-81 of the deposition shown in Figure 5.1. The average mass gain upon dosing $Y(CpBt)_3$ is 61 ng cm^{-2} and the average mass loss upon dosing HF-pyridine is 39 ng cm^{-2}, to give the overall MGPC of 22 ng cm^{-2} $cycle^{-1}$. The mass changes upon dosing each precursor are sharp and little change in mass is seen during the purges.

YF_3 deposition shows self-limiting behavior with respect to the amount of precursor dosed into the reactor. Self-limiting behavior is shown in Figure 5.3, where the

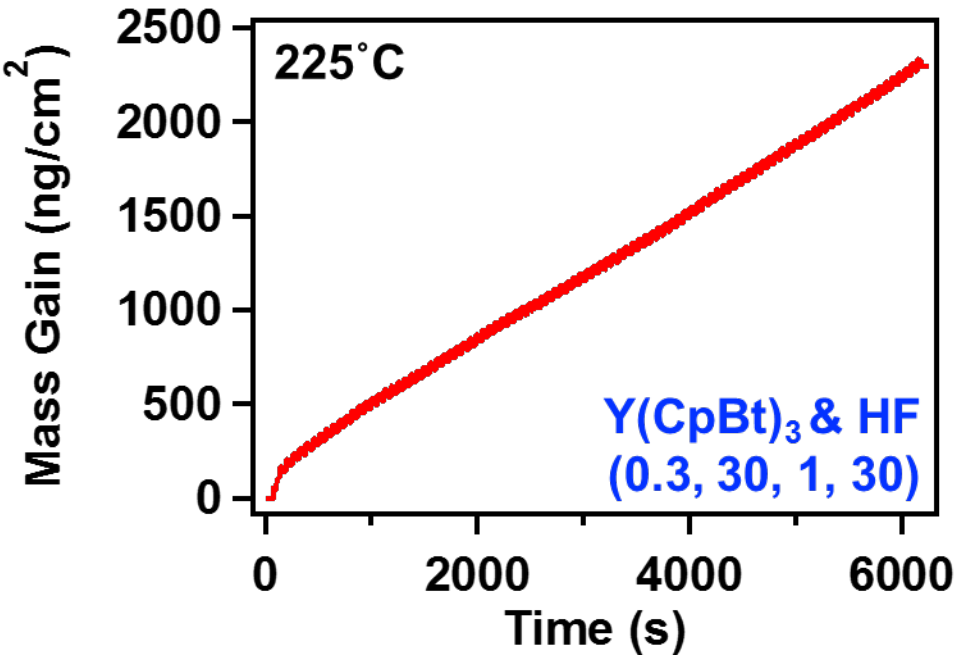

Figure 5.1 Linear growth of YF3 ALD. QCM measurements of mass changes over time for 100 cycles of YF3 ALD on Al2O3 at 225 ˚C using the dosing sequence (0.3, 30, 1, 30).

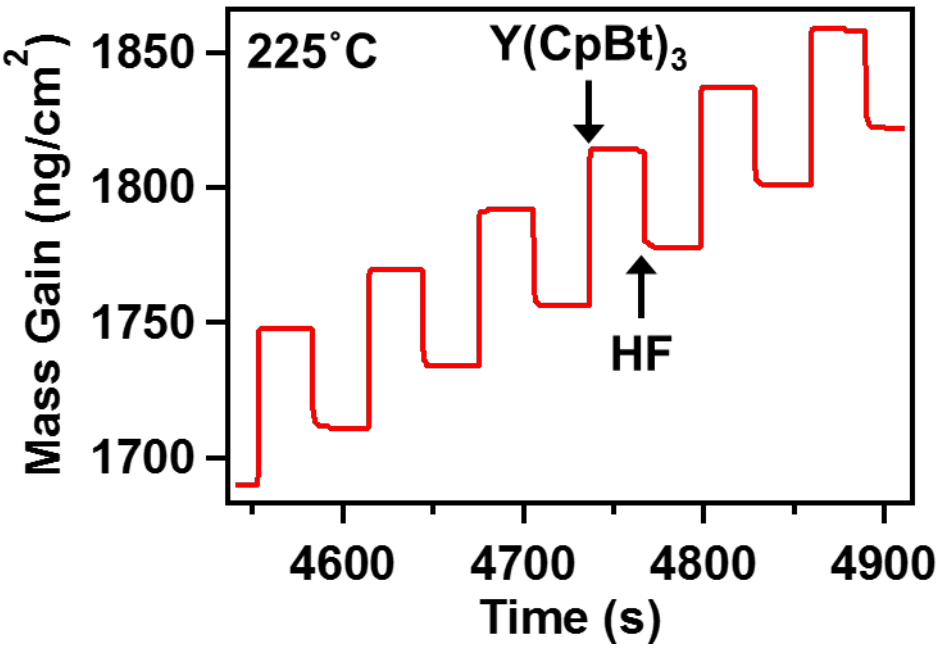

Figure 5.2 Expansion of linear growth of YF3 ALD. A closer look at the mass changes over time for 6 cycles in the deposition in Figure 5.1, representative of the linear growth region.

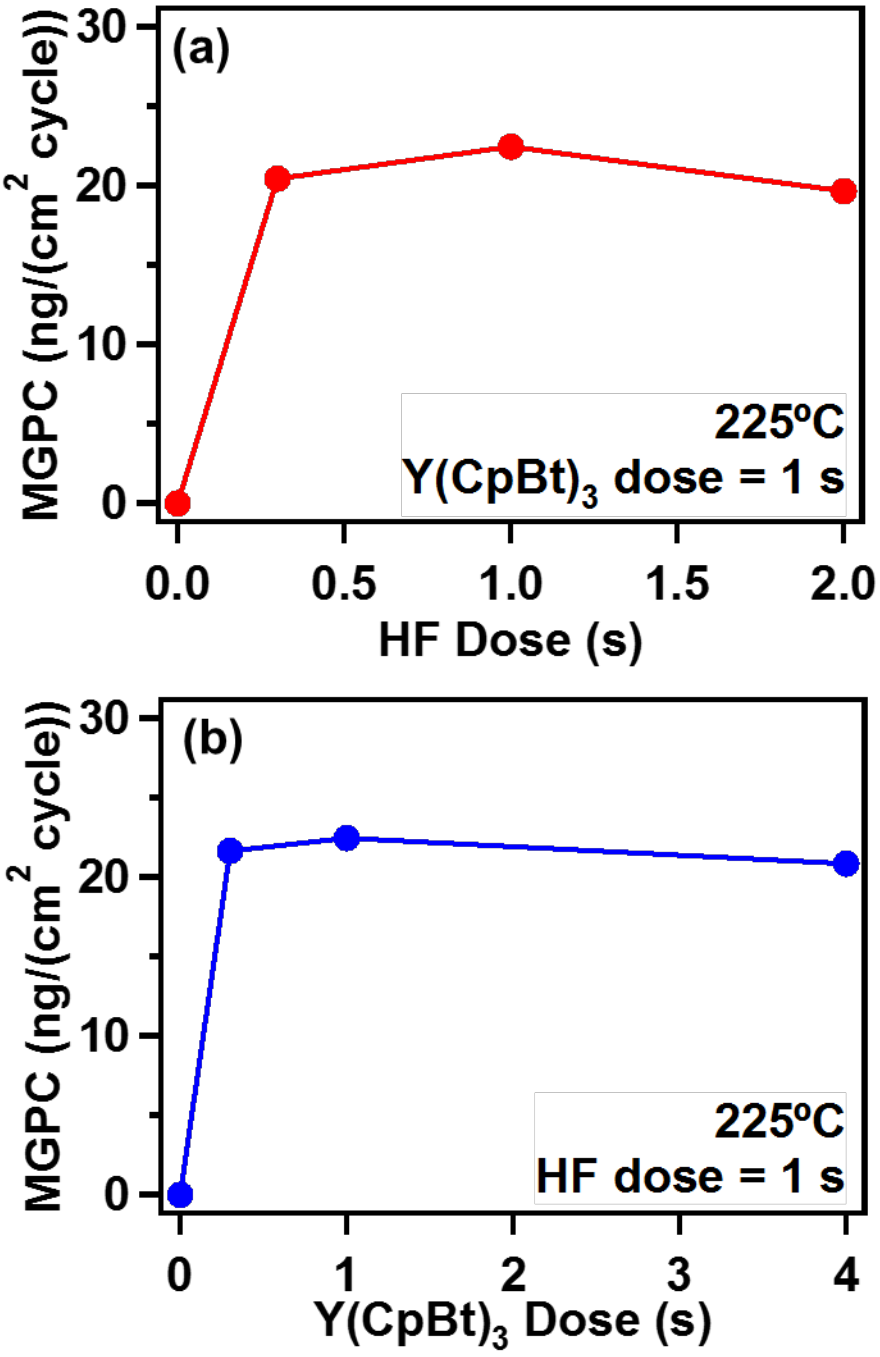

Figure 5.3 Self-limiting behavior of YF3 ALD. A) Growth rate of YF3 ALD as the dose of Y(CpBt)3 was varied from 0.3 to 4.0 s while HF was held at 1 s. B) Average growth rate as the dose of HF was varied from 0.3 to 2.0 s while Y(CpBt)3 dose was held at 1 s.

growth rate is compared to the amount of each precursor dosed into the reactor. In each of the graphs shown in Figure 5.3, one precursor is dosed at saturation while the length of the dose of the other precursor is varied. The saturated dose used for each precursor was one second. The dose pressure of the $Y(CpBt)_3$ is unknown because of the flow-over dosing configuration used. For HF-pyridine the dose pressure of the saturated dose was 55 mTorr. The length of the HF-pyridine dose was varied from 0.3 – 2.0 seconds as shown in Figure 5.3A, and the length of the $Y(CpBt)_3$ dose was varied from 0.3 – 4.0 seconds as shown in Figure 5.3B. The growth rate of 22 ng cm^{-2} $cycle^{-1}$ was consistent across all dose lengths used for both precursors. For both precursors, dose saturation was reached with the smallest dose of 0.3 seconds.

The linearity of growth and the growth rate were confirmed with ex situ thickness measurements using SE and XRR. YF_3 films deposited with 300, 600, 2500, and 3948 cycles on silicon with a native oxide were analyzed ex situ. SE measured thicknesses for these films were 113.5, 214.5, 1002.4, 1556.3 Å, respectively. These thickness measurements suggest a linear growth rate of 0.4 Å $cycle^{-1}$. Refractive indices measured with SE varied from 1.41 – 1.56 at a wavelength of 600 nm. The refractive index of bulk YF_3 is 1.53 at 600 nm.[15] The extinction coefficient for the film is zero in the range 240 to 1690 nm, indicating a transparent film. This extinction coefficient is expected based on the wide, 10.53 eV band gap of YF_3.[16] XRR thickness measurements for the two thinner films were consistent with SE measurements. Film roughness measured with XRR varied from 9 – 17 Å. The

density measured with XRR was 5.31 g cm^{-3}. The density of bulk YF_3 is 5.07 g cm^{-3}.[17] Using the density measured by XRR, the GPC measured by QCM can be used to calculate an Å $cycle^{-1}$ growth rate. This calculated growth rate is 0.4 Å $cycle^{-1}$, consistent with ex situ thickness measurements.

The composition of a YF_3 ALD film was measured by XPS with depth profiling by Ar^+ sputtering. A YF_3 film deposited with 600 ALD cycles onto a silicon substrate was analyzed. Excluding the surface and interface, the film was almost entirely composed of F and Y. Though the surface of the film showed a 19 % atomic concentration of C from adventitious C in the atmosphere, the rest of the film had no C. The majority of the film had a 2 % O impurity, with increasing O concentration at the interface with SiO_2. Excluding the interface and surface, the concentrations of F and Y in the film had a 3 to 1 ratio, consistent with YF_3.

GIXRD, HR-TEM, and electron diffraction were used to measure the crystallinity of a YF_3 film, as shown in Figure 5.4. YF_3 ALD films appeared highly crystalline. Peaks in the GIXRD spectrum of a 156 nm YF_3 film on Si agreed with peaks from a crystalline YF_3 reference spectrum with a primitive orthorhombic crystal structure, shown in Figure 5.4A.[17] Crystallinity was not dependent on the type of substrate nor on the thickness of the film. A 16 nm YF_3 film deposited on Al with a native oxide was also crystalline, as seen with HR-TEM and electron diffraction, shown in Figure 5.4B. The HR-TEM image shows large, several nm wide crystalline domains. The diffraction image shown in the

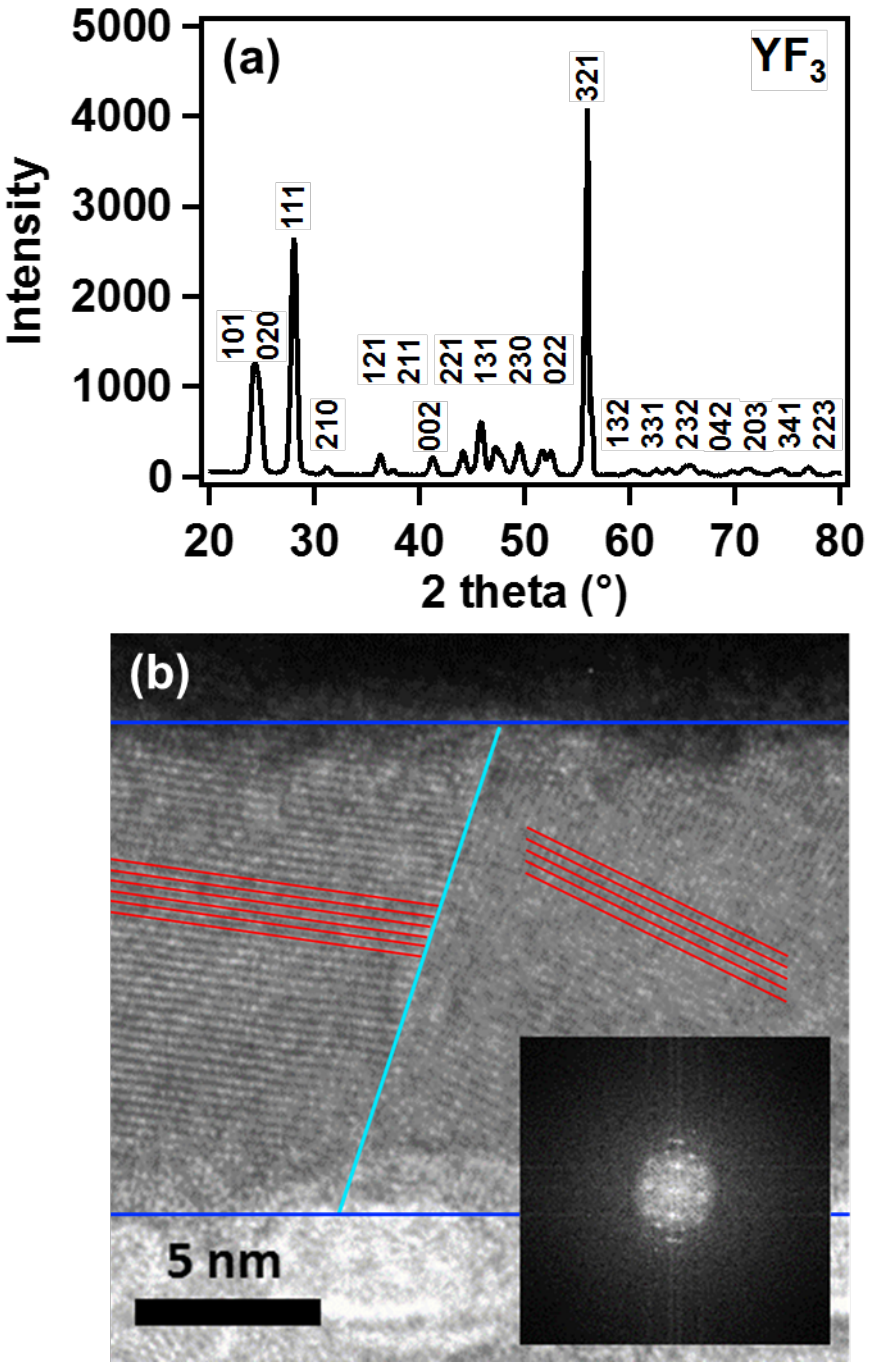

Figure 5.4 A) GIXRD of a 156 nm YF3 ALD film deposited on Si with peak assignments from an orthorhombic YF3 reference spectrum.17 B) HR-TEM of a 16 nm YF3 film deposited on aluminum showing large crystalline domains with diffraction inset.

inset of Figure 5.4B shows distinct diffraction spots, consistent with a crystalline film. Previous thin film studies reported crystallinity of YF_3 films deposited at temperatures above 200 ˚C.[13] Our YF_3 films were deposited at 225 ˚C, therefore crystallinity is expected.

The reaction mechanism for YF_3 ALD is expressed as two separate half reactions, as shown in Figure 5.5 and below:

$$YF_3 \,|\, xHF^* + Y(CpBt)_3 \rightarrow YF_3 \,|\, YF_x(CpBt)_{3-x}^* + xHCpBt \qquad (1)$$

$$YF_3 \,|\, YF_x(CpBt)_{3-x}^* + xHF \rightarrow YF_3 \,|\, YF_3 \,|\, xHF^* + (3-x)HCpBt \qquad (2)$$

The value of x in the above reactions can be calculated from the QCM results according to the procedure outlined by Lee et al.[18] This value represents the number of HF species adsorbed on the surface relative to each YF_3 species deposited per cycle. The number of HF species adsorbed on the surface is dependent on the Lewis acid strength of the metal fluoride, with more HF species adsorbed onto strong Lewis acid metal fluoride surfaces.[18] The value of x calculated from the QCM results of YF_3 ALD is 0.4, indicating that very few HF species adsorb to the surface. This behavior is consistent with YF_3 acting as a weak Lewis acid, similar to MnF_2 and ZnF_2 ALD.

5.3B Y_2O_3 ALD

Unlike YF_3 ALD, Y_2O_3 ALD is not an ideal ALD system. Y_2O_3 ALD shows an increasing growth rate with an increasing number of cycles. The increasing growth rate

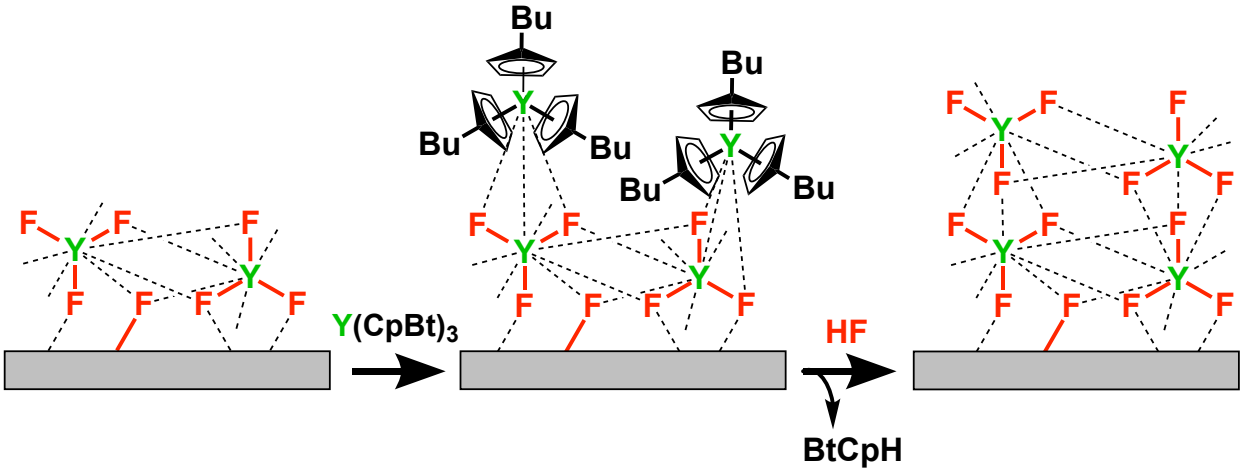

Figure 5.5 Proposed reaction mechanism for YF3 ALD. This mechanism is based on the mass changes measured with QCM of the ALD of YF3 using Y(CpBt)3 and HF precursors.

is related to the absorption of H_2O into the Y_2O_3 film. H_2O absorbed in the film is difficult to purge, leading to uncontrolled growth.[8] As the thickness of the Y_2O_3 film increases, the amount of H_2O absorption increases, leading to increasing growth rates with cycle number.

Despite the non-ideality, we report the details of Y_2O_3 ALD using our chamber here to lay the groundwork for the deposition of YO_xF_y films. Figure 5.6A shows 50 ALD cycles of Y_2O_3 using $Y(CpBt)_3$ and H_2O with a dose profile of (2, 30, 0.3, 30) at 225 ˚C. The dose pressure of H_2O is 50 mTorr. The average GPC over the first 50 cycles is 39 ± 4 ng cm^{-2} $cycle^{-1}$. Figure 5.6B shows cycles 39-45 of the Y_2O_3 deposition. The average mass gain upon dosing $Y(CpBt)_3$ is 59 ± 2 ng cm^{-2}. The average mass loss upon dosing H_2O is 20 ± 3 ng cm^{-2}. QCM studies measuring differences in GPC with increasing precursor dose size did not show self-limiting behavior for either precursor.

Ex situ XRR, SE and GIXRD analysis was performed on a Y_2O_3 film deposited on Si with 200 cycles of ALD. The growth rate of Y_2O_3 ALD was determined with ex situ analysis using XRR and SE. Both XRR and SE measured a film thickness of 163 Å, suggesting a growth rate of 0.8 Å $cycle^{-1}$. Film roughness measured with XRR was 8 Å and the density was consistent with the bulk density of Y_2O_3 of 5.01 g cm^{-3}. Using this density, the GPC from QCM analysis can be converted into a growth rate in Å $cycle^{-1}$. The QCM-derived growth rate is 0.8 Å $cycle^{-1}$ and agrees with ex situ thickness measurements. The

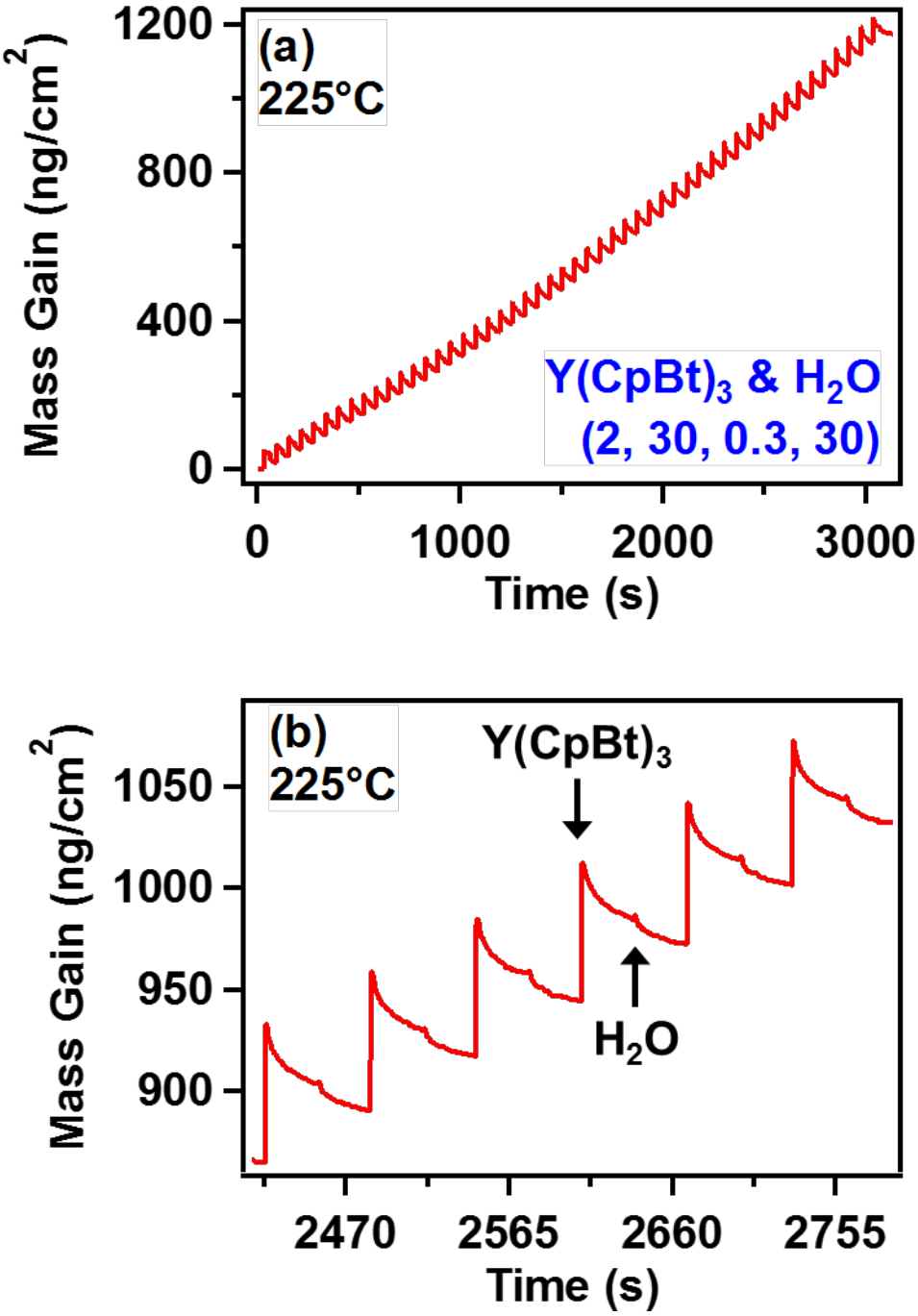

Figure 5.6 Pseudo-linear growth of Y2O3 ALD. A) QCM measurements of mass changes over time for 50 cycles of Y2O3 ALD on Al2O3 at 225 ˚C using the dosing sequence (2, 30, 0.3, 30). B) A closer look at the mass changes over time for 6 cycles in this deposition.

refractive index of this material measured with SE was 1.93 at 600 nm, the extinction coefficient was 0 between 240 and 1690 nm and both values are consistent with that of bulk Y_2O_3.[19] GIXRD was used to determine the crystallinity of the film. The film was highly crystalline and was consistent with the reference spectrum of a Y_2O_3 with a cubic crystal structure.[20]

XPS analysis with depth profiling was used to determine the composition of the film. C impurity was only present at the surface of the film, with 22.3 % C impurity, likely adventitious C. A stoichiometric Y_2O_3 should have a O/Y ratio of 1.5. Excluding the surface and interface of the film, XPS analysis revealed a O/Y ratio of 1.4. Y_2O_3 is prone to native point defects in the form of oxygen vacancies and oxygen interstitials. It is possible that the oxygen deficiency in this film may be a result of oxygen vacancies in the Y_2O_3 crystal structure of the ALD film. The presence of oxygen vacancies may contribute to the extreme depth of F^- penetration into Y_2O_3 upon surface exposure to HF, as detailed in the following section.

5.3C YO_xF_y ALD

A typical approach to depositing a mixed material thin film with controlled stoichiometry is to deposit a nanolaminate or multilayer structure. Nanolaminate thin films are deposited by alternating the deposition of two or more different materials. However, we found that depositing a YO_xF_y film using a nanolaminate approach was not possible. Attempts to use a nanolaminate approach by alternating cycles of YF_3 and

Y_2O_3 ALD resulted in YF_3 films, not YO_xF_y. There are two properties of the yttrium oxide/fluoride system that preclude a nanolaminate approach to deposition of this mixed material. First, the exchange reaction between Y_2O_3 and HF to form YF_3 is highly favorable, according the following reaction:

$$Y_2O_3 + 6\ HF \rightarrow 2\ YF_3 + 3\ H_2O \quad (3)$$

This reaction has $\Delta G^\circ = -102.9$ kcal mol^{-1} at 225 ˚C. The second unique property of this system is the depth of penetration of HF into Y_2O_3, as described in the following section. The result of these unique properties is that the thin layers of Y_2O_3 are converted to YF_3 when a nanolaminate approach is used. Any deposition scheme to create YO_xF_y films must accommodate these unique system properties.

Remarkably, we found that the reaction depth of HF into Y_2O_3 is well over 10 nm. XPS with depth profiling was used to determine the composition of a YO_xF_y film deposited with 200 cycles of Y_2O_3 ALD on sapphire, then exposed to 100 doses of HF at a pressure of 50 mTorr, as shown in Figure 5.7. The film deposition and HF exposure were conducted at 225 ˚C. The depth profile shows the presence of F throughout the entire thickness of the film. XPS of the near-surface of the film, excluding the region containing adventitious carbon, indicated a 34.5 % atomic concentration of Y, a 24.5 % atomic concentration of O and a 41.1 % atomic concentration of F. The concentration of F was highest at the surface of the film and decreased linearly from 41.1 % to 6.5 % at the interface with the sapphire substrate. As the relative F concentration decreased, the

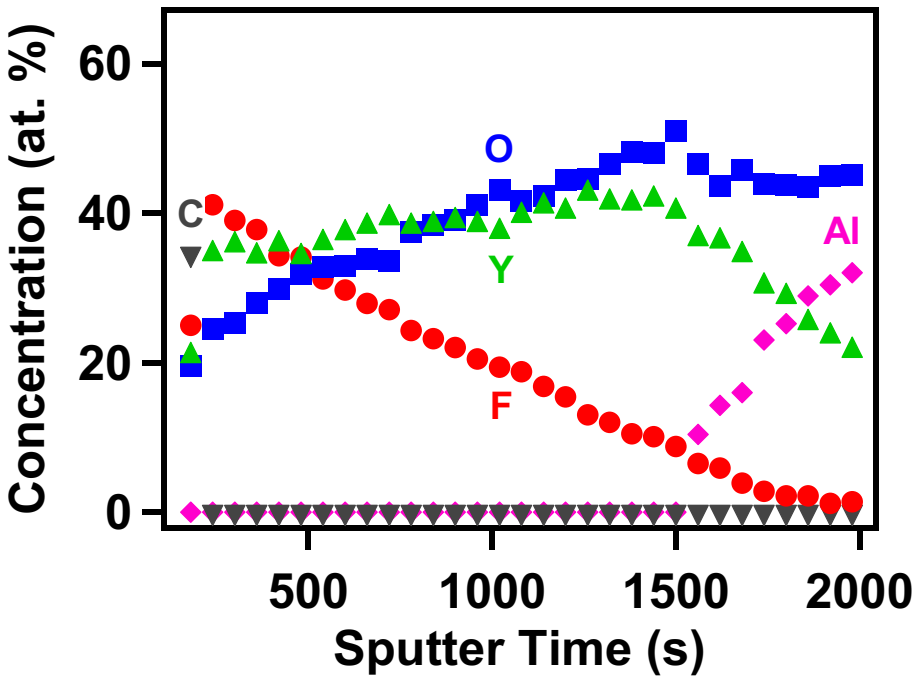

Figure 5.7 Indication of fluorine exchange reaction deep into Y2O3. An XPS depth profile of a 16 nm Y2O3 film deposited on sapphire with 200 ALD cycles after exposure to 5 Torr s of HF at 225 ˚C. The depth profile shows the presence of F throughout.

relative O concentration increased, suggesting that F exchanges for O in the film. The concentration of Y remains steady through the film. A thickness difference was also observed in this sample. The initial thickness of the Y_2O_3 film prior to exposure to HF was 163 Å, as measured by XRR. Upon exposure to HF the film thickness increased to 170 Å, indicating a 7 Å increase in thickness.

In situ QCM was used to determine the maximum depth of F^- reaction into a Y_2O_3 film. Exchange of F for O in the film can be monitored with QCM because there is a mass gain upon fluorination. According to reaction 3, each O is replaced by 2 F to maintain charge balance. Fluorination mass gain was measured by in situ QCM on six different Y_2O_3 films with thicknesses ranging from 2 – 64 nm, as shown in Figure 5.8. These different thicknesses of Y_2O_3 were exposed to 17 sequential doses of HF at a dose pressure of 50 mTorr. The overall trend in mass gain with HF exposures can be modelled with an exponential curve. In each sample, there was a large mass gain with the first HF exposure. The mass gain upon first HF exposure varied from 81 to 177 ng cm^{-2} and scaled with the thickness of the initial Y_2O_3 film. The HF exposures after the first exposure resulted in smaller mass gains. Samples with initial Y_2O_3 film thicknesses between 2 and 16 nm showed a positive relationship between total mass gain and initial Y_2O_3 film thickness. This trend suggests that fluorination is not limited to the surface of the film. Samples with initial Y_2O_3 film thicknesses of 16 nm or greater had similar mass gains. In these thicker films, the total mass gain upon fluorination was 315 ± 16 ng cm^{-2}

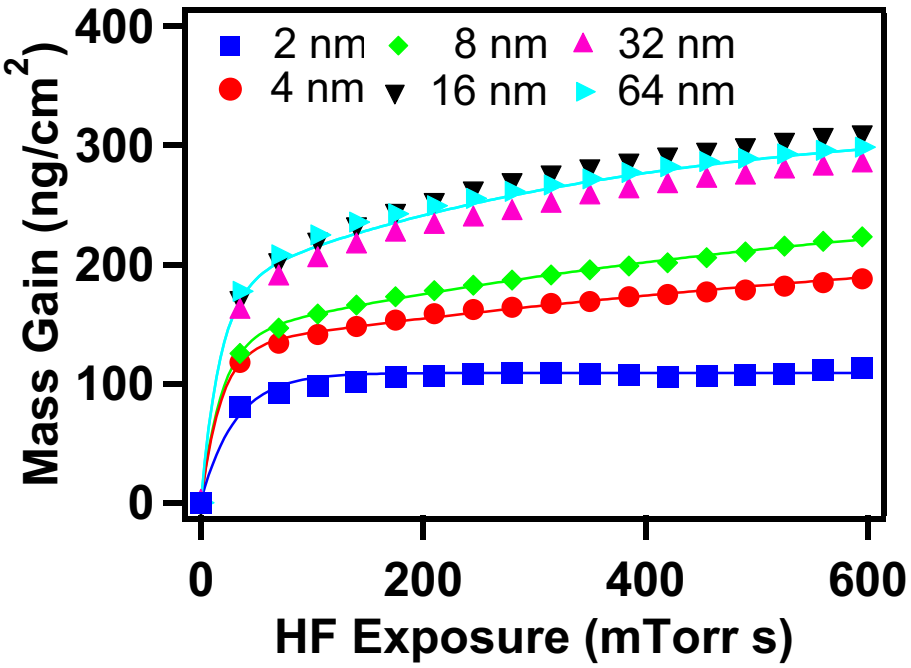

Figure 5.8 Depth of fluorine exchange reaction in Y2O3. QCM measurements of mass gains when different thicknesses of Y2O3 films are exposed to sequential doses of HF. The mass gain is indicative of the fluorine exchange reaction.

over the 17 HF exposures. The consistency in the mass gain in thicker Y_2O_3 films suggests that there is a maximum depth of F^- reaction into Y_2O_3. Because the total mass gain stops increasing with Y_2O_3 thickness at 16 nm, the F^- penetration depth limit is ~16 nm. The depth of F^- reaction into Y_2O_3 films, depicted in Figure 5.8, is unusual. Most metal oxides undergo exchange reactions with HF, but fluorination is typically limited to the surface of the metal oxide. For example, when HF is exposed to the surface of Al_2O_3, an exchange reaction occurs exclusively at the surface of the material, with F^- penetrating only 0.5 Å into the film.[21] In contrast, F^- penetrates ~16 nm into Y_2O_3. F^- penetration in Y_2O_3 is likely a diffusion process, and the 16 nm penetration limit is likely a diffusion limit. The deep diffusion of F^- is likely facilitated by the oxygen vacancy network in Y_2O_3. Y_2O_3 thin films contain point defects in the form of oxygen vacancies within their crystal structure.[22] These oxygen vacancies can create localized points of positive fixed charge.[23,24] The crystallinity is maintained in YO_xF_y films, as described below, and it is likely that deep F^- penetration relies on crystallinity to move through the oxygen vacancies in the film.

We used our knowledge of the depth of fluorination of Y_2O_3 to develop YO_xF_y films with a tunable and homogeneous composition. These films were created using super cycles, where each super cycle consisted of *n* numbers of cycles of Y_2O_3 ALD, followed by HF exposure. A cartoon of this super cycle approach is shown in Figure 5.9. The number of Y_2O_3 cycles (*n*) deposited prior to each HF exposure was used to control

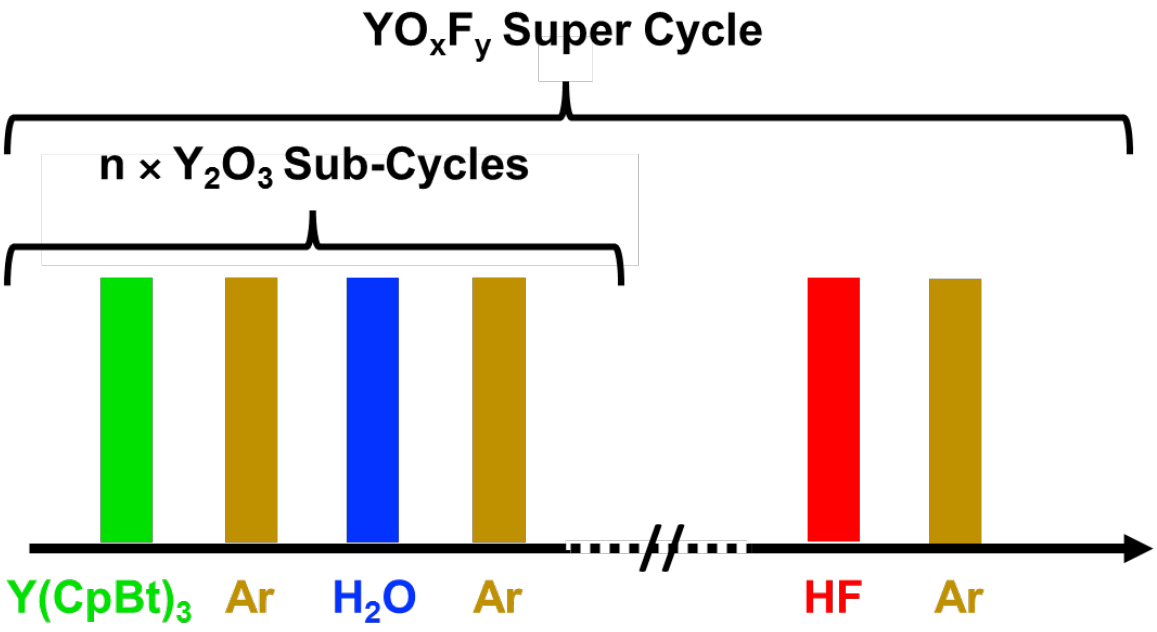

Figure 5.9 Super cycle dosing sequence for depositing YOxFy films. Each super cycle consists of *n* Y2O3 sub-cycles, followed by an HF dose, where n determines the composition of the resulting film.

the amount of F in the resulting film. Using fewer Y_2O_3 cycles per super cycle resulted in films with higher concentrations of F. To deposit a homogeneous film, *n* was constrained by the depth of F penetration and exchange. This depth is ~16 nm or ~200 cycles of Y_2O_3 ALD, as determined with in situ QCM in Figure 5.8. The number *n* reported here varied between 1 and 100. Super cycles were repeated to deposit a film of the desired thickness.

The tunability of the YO_xF_y films deposited using this super cycle approach is shown in Figure 5.10. By changing *n*, the composition of the YO_xF_y film is tuned. Four distinct YO_xF_y films were grown on Si at 225 °C. XPS with depth profiling was used to determine the composition of the films. The relative concentrations of F and O were compared in each film. The relative ratio of F was calculated by comparing the atomic concentration of F to the total concentration of anions (O + F) in the film. The ratio of F varied between 0.95 and 0.42. The compositions of these films were most consistent with the following stoichiometries: Y_7OF_{19}, Y_3OF_7, $Y_5O_4F_7$, YOF and $Y_9O_{10}F_7$ for depositions with *n* = 1, 10, 20, 50, and 100, respectively. Though a super cycle approach is used to deposit these YO_xF_y films, the XPS depth profiles indicate that the films are remarkably homogeneous. The films were also very pure. Excluding the surface and interface, all of these films were entirely composed of Y, O and F. The surface of the films showed small atomic concentrations of C from adventitious C in the atmosphere, and the rest of the film had no measurable C.

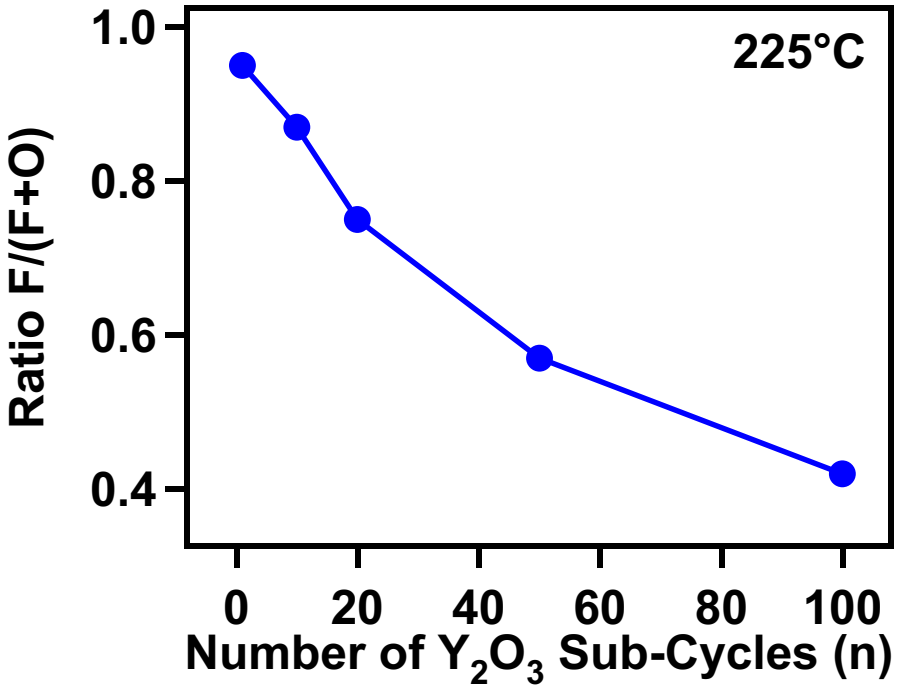

Figure 5.10 YOxFy films deposited with increasing numbers of Y2O3 sub-cycles have a decreasing relative composition of F. Relative F composition is defined as the amount of F compared to the total anion concentration (F+O) in the YOxFy film.

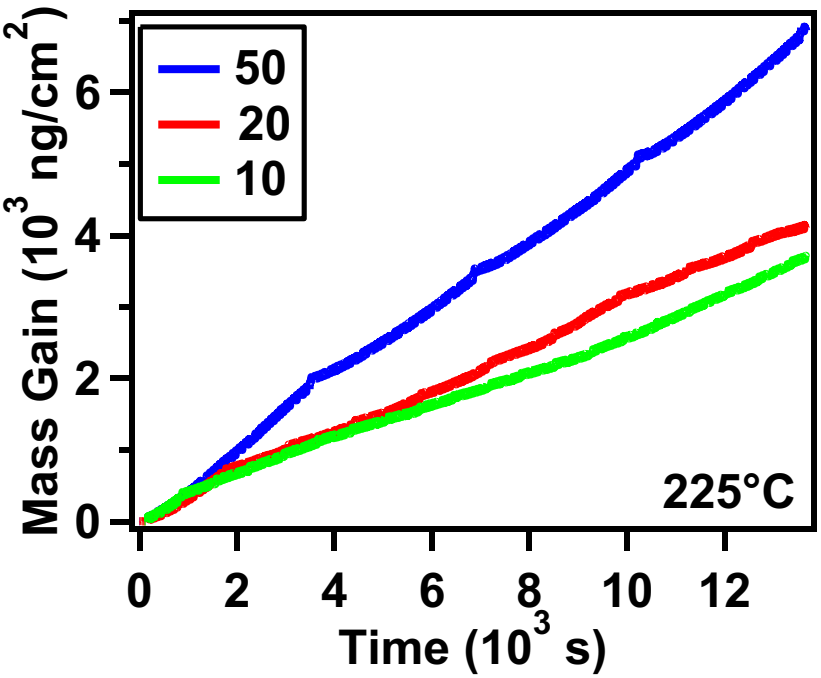

Figure 5.11 Linear growth of YOxFy ALD. QCM measurements of mass changes over time for the deposition of three YOxFy films with different n values indicated in the legend.

The growth rates of the distinct YO_xF_y films was determined using in situ QCM and ex situ XRR and SE. In situ QCM analysis of several YO_xF_y depositions revealed linear and consistent growth rates. QCM data for the deposition of three separate YO_xF_y films is shown in Figure 5.11. The figure shows 4, 10 and 20 super cycles of deposition, with *n* = 50, 20 and 10, respectively. The growth rates per super cycle (GPSC) are summarized in Table 1. Growth rates increase with *n*. The MGPC in within the Y_2O_3 sub-cycle region in each of these films was fairly consistent at 17 ± 5 ng cm^{-2} $cycle^{-1}$. In contrast, the mass gain during HF exposure increased with *n*. The linearity of growth and growth rates were confirmed with ex situ thickness measurements using SE and XRR. YO_xF_y films deposited with *n* = 50, 20 and 10 and 6, 15, and 30 super cycles, respectively, had film thicknesses of 124, 84 and 87 Å. The growth rates for these films are summarized in Table 1. The bulk density measured by XRR for all three films was 5.01 g cm^{-3}. From this density, the QCM GPSCs can be used to calculate growth rates in Å per super cycle. These growth rates from QCM are consistent with ex situ analysis. The refractive indices for these films are shown in Table 1. Refractive indices fell between the refractive indices of Y_2O_3 at 1.93 and YF_3 at 1.53. The refractive indices of the YO_xF_y films scale with the ratio of F in the film. The extinction coefficient for all three films was zero in the range 240 to 1690 nm.

Table 1. Growth Rates and Refractive Indices of YO_xF_y Films

No. Y_2O_3 Sub-Cycles (*n*)	GPSC by QCM (ng cm^{-2})	GPSC by SE (Å/ super cycle)	Refractive Index at λ = 600 nm
10	168 ± 46	3	1.65
20	356 ± 75	7	1.73
50	1023 ± 67	20	1.88

Consistent with YF_3 and Y_2O_3 films, YO_xF_y films appear highly crystalline, as measured with GIXRD. Each of these YO_xF_y films has a distinct crystal structure. The GIXRD spectrum of a 97 nm $Y_5O_4F_7$ film deposited with *n* = 20 is shown in Figure 5.12A. This film was deposited on sapphire at 225 ˚C. The GIXRD of the film is consistent with a reference spectrum of $Y_5O_4F_7$ with a body-centered orthorhombic crystal structure, depicted in Figure 5.12B.[25] The GIXRD spectrum of a 323 nm YOF film deposited with *n* = 50 is shown in Figure 5.13A. The film was deposited on sapphire at 225 ˚C. The GIXRD of this film is consistent with the reference spectrum of rhombohedral YOF, depicted in Figure 5.13B.[26] As mentioned above, it is likely that the consistency in the crystallinity of all of these yttrium-based films helps facilitate the deep penetration of F^-.

5.4 Conclusion

YF_3, Y_2O_3, and YO_xF_y films were deposited by ALD with the precursors $Y(CpBt)_3$, H_2O and HF. The YO_xF_y films deposited were Y_7OF_{19}, Y_3OF_7, $Y_5O_4F_7$, YOF and $Y_4O_5F_2$, as determined with XPS depth profiling. YO_xF_y films were deposited with a super cycle

dosing sequence. In each deposition, *n* was varied to deposit films with different compositions. The linear growth rates of YF_3 and YO_xF_y ALD were determined with in situ QCM and verified with XRR and SE. The growth rate of YF_3 was 0.4 Å cycle^{-1}. The growth rate of YO_xF_y scaled with *n* from 3 Å (super cycle)$^{-1}$ for a dosing scheme with *n* = 10 to 20 Å (super cycle)$^{-1}$ for a dosing scheme with *n* = 50. All of the yttrium-based films studied in this work were highly crystalline, as measured with GIXRD, and their crystal structures varied with their composition. The refractive index of these films also varied

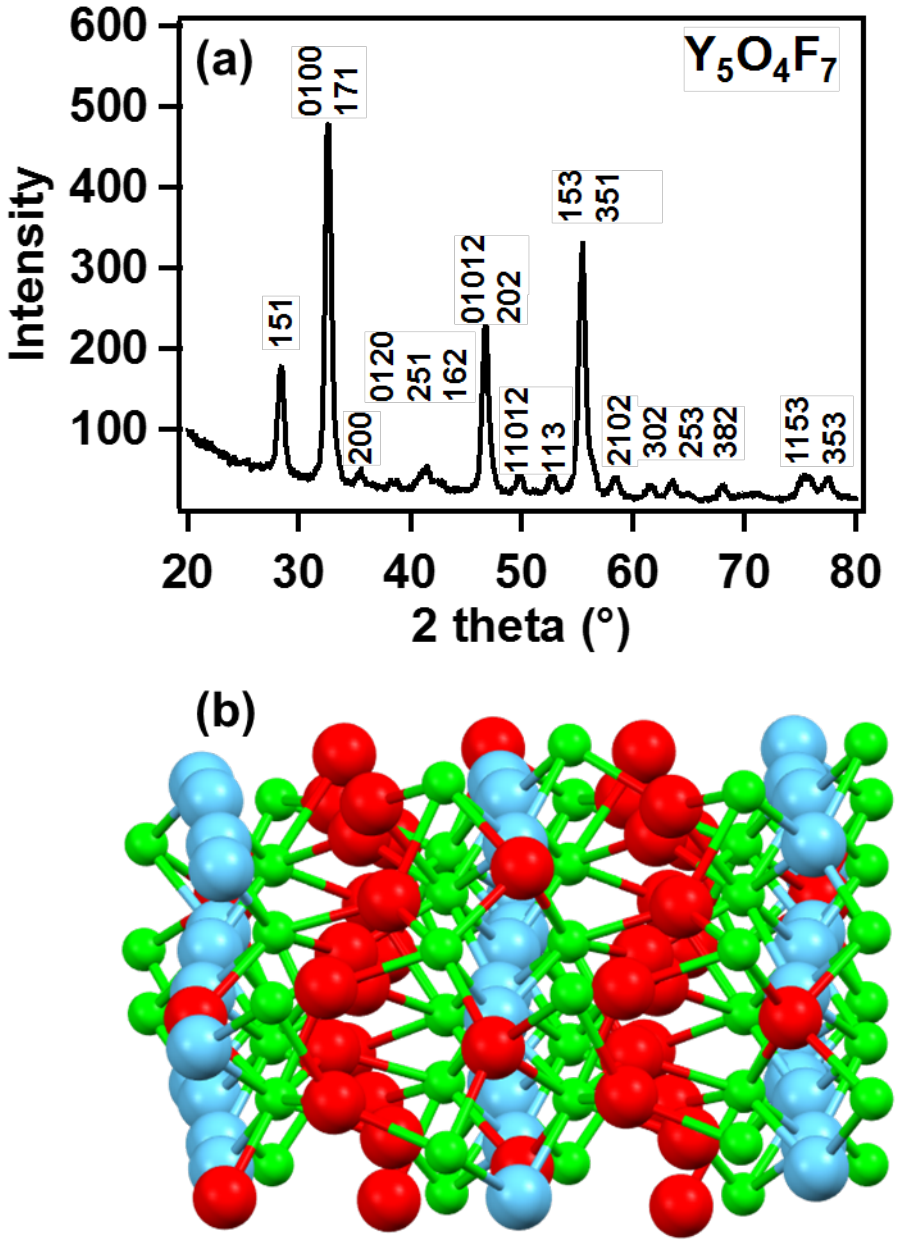

Figure 5.12 (a) GIXRD of a 97 nm $Y_5O_4F_7$ film deposited on sapphire using n = 20 with peak assignments from an orthorhombic $Y_5O_4F_7$ reference spectrum. (b) The crystal structure of the orthorhombic Y5O4F7 with color coding as follows: Y (green), O (blue), and F (red).

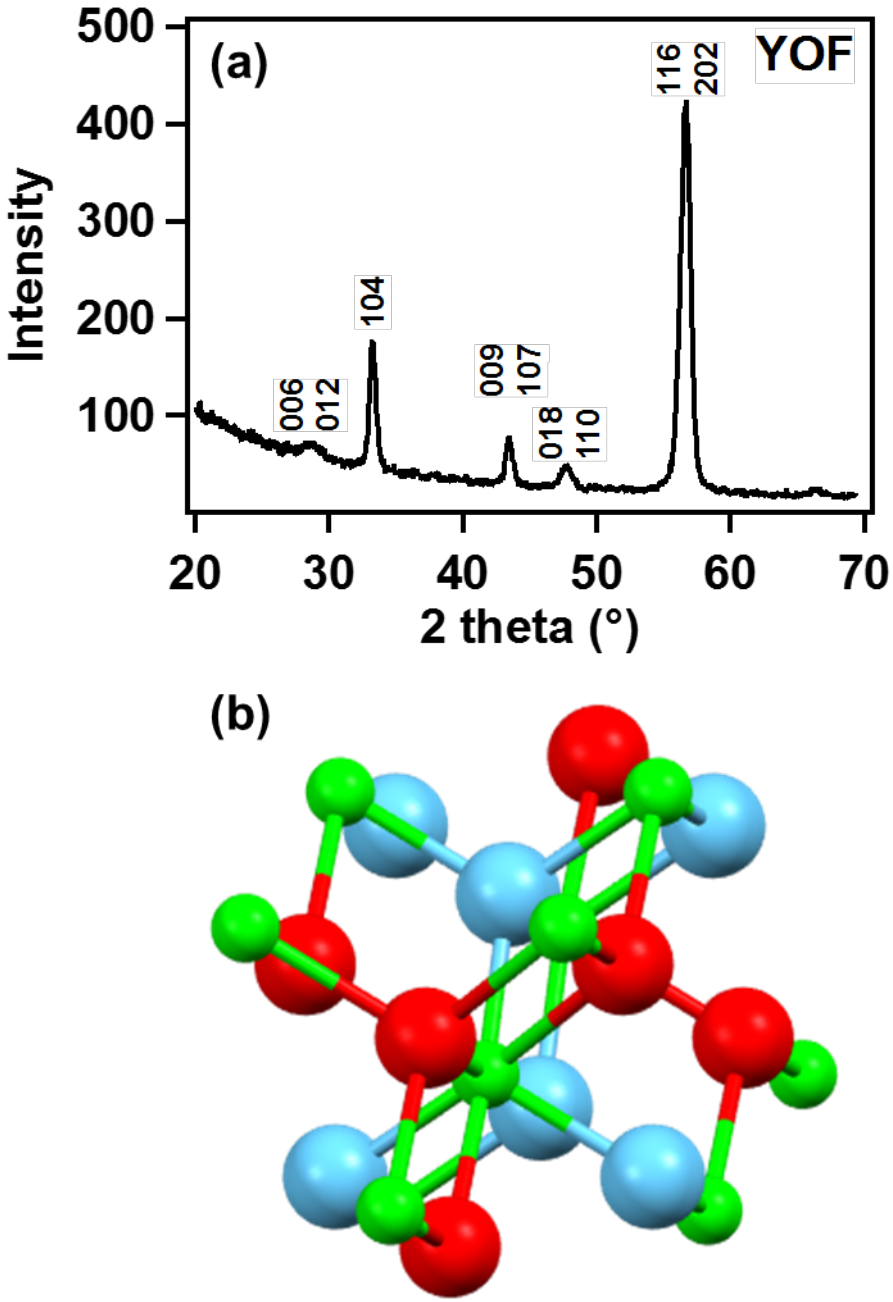

Figure 5.13 (a) GIXRD of a 323 nm YOF film deposited on sapphire using n = 50 with peak assignments from a rhombohedral YOF reference spectrum.26 (b) The crystal structure of the rhombohedral YOF used as a crystalline reference.

with composition, as measured with SE. All of these films had little to no carbon impurity, as measured with XPS depth-profiling.

A super cycle dosing scheme was needed to deposit YO_xF_y ALD films because of the deep penetration of the F^- exchange reaction in Y_2O_3. In this highly favorable reaction, F is exchanged

for O in the film. QCM and XPS depth profiling were used to determine that the limit of F penetration into Y_2O_3 was ~16 nm. The depth of penetration of F^- into Y_2O_3 is unusual compared to other metal oxides, where the exchange reaction is typically limited to the surface of the film. The deep penetration of F^- into Y_2O_3 is likely facilitated by the O vacancy network in Y_2O_3 and the high crystallinity of all of the deposited materials. Further work should explore the mechanism of F^- penetration in these materials further.

The high level of control over the composition of the YO_xF_y ALD films was possible because of the knowledge gained about F^- exchange in Y_2O_3. These YO_xF_y films have distinct properties and may interact differently with different reactive plasmas. With the high level of control over the composition of these films, it will be possible to tailor a protective coating for the type of reactive plasma used in each unique plasma chamber.

5.5 References

(1) Agarwal, A.; Kushner, M. J. *J. Vac. Sci. Technol. A* **2008**, *26* (3), 498–512.

(2) Cao, Y.-C.; Zhao, L.; Luo, J.; Wang, K.; Zhang, B.-P.; Yokota, H.; Ito, Y.; Li, J.-F. *Appl. Surf. Sci.* **2016**, *366*, 304–309.

(3) Ma, T.; List, T.; Donnelly, V. M. *J. Vac. Sci. Technol. A* **2017**, *35* (3), 031303.

(4) Miwa, K.; Takada, N.; Sasaki, K. *J. Vac. Sci. Technol. A* **2009**, *27* (4), 831–835.

(5) Shiba, Y.; Teramoto, A.; Goto, T.; Kishi, Y.; Shirai, Y.; Sugawa, S. *J. Vac. Sci. Technol. A* **2017**, *35* (2), 021405.

(6) Putkonen, M.; Sajavaara, T.; Johansson, L.-S.; Niinistö, L. *Chem. Vap. Depos.* **2001**, *7* (1), 44–50.

(7) Niinistö, J.; Putkonen, M.; Niinistö, L. *Chem. Mater.* **2004**, *16* (15), 2953–2958.

(8) de Rouffignac, P.; Park, J.; Gordon, R. G. *Chem. Mater.* **2005**, *17* (19), 4808–4814.

(9) Majumder, P.; Jursich, G.; Kueltzo, A.; Takoudis, C. *J. Electrochem. Soc.* **2008**, *155* (8), G152.

(10) Xu, R.; Selvaraj, S. K.; Azimi, N.; Takoudis, C. G. *ECS Trans.* **2013**, *50* (13), 107–116.

(11) Park, I.-S.; Chan Jung, Y.; Seong, S.; Ahn, J.; Kang, J.; Noh, W.; Lansalot-Matras, C. *J. Mater. Chem. C* **2014**, *2* (43), 9240–9247.

(12) Mai, L.; Boysen, N.; Subaşı, E.; Arcos, T. de los; Rogalla, D.; Grundmeier, G.; Bock, C.; Lu, H.-L.; Devi, A. *RSC Adv.* **2018**, *8* (9), 4987–4994.

(13) Pilvi, T.; Puukilainen, E.; Munnik, F.; Leskelä, M.; Ritala, M. *Chem. Vap. Depos.* **2009**, *15* (1–3), 27–32.

(14) Elam, J. W.; Sechrist, Z. A.; George, S. M. *Thin Solid Films* **2002**, *414* (1), 43–55.

(15) Bezuidenhout, D. F.; Clarke, K. D.; Pretorius, R. *Thin Solid Films* **1987**, *155* (1), 17–30.

(16) Krupa, J. .; Queffelec, M. *J. Alloys Compd.* **1997**, *250* (1–2), 287–292.

(17) Zalkin, A.; Templeton, D. H. *J. Am. Chem. Soc.* **1953**, *75* (10), 2453–2458.

(18) Lee, Y.; Sun, H.; Young, M. J.; George, S. M. *Chem. Mater.* **2016**, *28* (7), 2022–2032.

(19) Nigara, Y. *Jpn. J. Appl. Phys.* **1968**, *7* (4), 404–408.

(20) Baldinozzi, G.; Bérar, J. F.; Calvarin-Amiri, G. *Mater. Sci. Forum* **1998**, *278–281*, 680–685.

(21) Kondati Natarajan, S.; Elliott, S. D. *Chem. Mater.* **2018**, *30* (17), 5912–5922.

(22) Jollet, F.; Noguera, C.; Gautier, M.; Thromat, N.; Duraud, J.-P. *J. Am. Ceram. Soc.* **1991**, *74* (2), 358–364.

(23) Zheng, J. X.; Ceder, G.; Maxisch, T.; Chim, W. K.; Choi, W. K. *Phys. Rev. B* **2006**, *73* (10), 104101.

(24) Lacroix, B.; Paumier, F.; Gaboriaud, R. J. *Phys. Rev. B* **2011**, *84* (1), 014104.

(25) Bevan, D. J. M.; Mohyla, J.; Hoskins, B. F.; Steen, R. J. *Eur. J. Solid State Inorg. Chem.* **1990**, *27* (3), 451–465.

(26) Zachariasen, W. H.; *Acta Crystallogr.* **1951**, *4* (3), 231–236.

6. Bibliography

(1) Grubbs, R. K.; Steinmetz, N. J.; George, S. M. *J. Vac. Sci. Technol. B Microelectron. Nanom. Struct.* **2004**, *22* (4), 1811.

(2) Kessels, W. M. M.; Knoops, H. C. M.; Dielissen, S. A. F.; Mackus, A. J. M.; van de Sanden, M. C. M. *Appl. Phys. Lett.* **2009**, *95* (1), 13114.

(3) George, S. M.; Ott, A. W.; Klaus, J. W. *J. Phys. Chem.* **1996**, *100* (31), 13121–13131.

(4) Ferguson, J. .; Weimer, A. .; George, S. . *Thin Solid Films* **2002**, *413* (1–2), 16–25.

(5) Kazyak, E.; Chen, K.-H.; Wood, K. N.; Davis, A. L.; Thompson, T.; Bielinski, A. R.; Sanchez, A. J.; Wang, X.; Wang, C.; Sakamoto, J.; Dasgupta, N. P. *Chem. Mater.* **2017**, *29* (8), 3785–3792.

(6) Thimsen, E.; Riha, S. C.; Baryshev, S. V.; Martinson, A. B. F.; Elam, J. W.; Pellin, M. J. *Chem. Mater.* **2012**, *24* (16), 3188–3196.

(7) Kukli, K.; Kemell, M.; Castán, H.; Dueñas, S.; Seemen, H.; Rähn, M.; Link, J.; Stern, R.; Heikkilä, M. J.; Ritala, M.; Leskelä, M. *ECS J. Solid State Sci. Technol.* **2018**, *7* (5), P287–P294.

(8) Shao, H.-I.; Umemoto, S.; Kikutani, T.; Okui, N. *Polymer (Guildf).* **1997**, *38* (2), 459–462.

(9) Kim, A.; Filler, M. A.; Kim, S.; Bent, S. F. *J. Am. Chem. Soc.* **2005**, *127* (16), 6123–6132.

(10) Adamczyk, N. M.; Dameron, A. A.; George, S. M. *Langmuir* **2008**, *24* (5), 2081–2089.

(11) Yoshimura, T.; Tatsuura, S.; Sotoyama, W. *Appl. Phys. Lett.* **1991**, *59* (4), 482–484.

(12) Putkonen, M.; Harjuoja, J.; Sajavaara, T.; Niinistö, L. *J. Mater. Chem.* **2007**, *17* (7), 664–669.

(13) Loscutoff, P. W.; Zhou, H.; Clendenning, S. B.; Bent, S. F. *ACS Nano* **2010**, *4* (1), 331–341.

(14) Ivanova, T. V.; Maydannik, P. S.; Cameron, D. C. *J. Vac. Sci. Technol. A* **2012**, *30* (1), 01A121.

(15) Lee, J. S.; Lee, Y.-J.; Tae, E. L.; Park, Y. S.; Yoon, K. B. *Science* **2003**, *301* (5634), 818–821.

(16) George, S. M.; Lee, B. H.; Yoon, B.; Abdulagatov, A. I.; Hall, R. A. *J. Nanosci. Nanotechnol.* **2011**, *11* (9), 7948–7955.

(17) George, S. M.; Yoon, B.; Dameron, A. A. *Acc. Chem. Res.* **2009**, *42* (4), 498–508.

(18) Aleskovskii, V. B.; Kol'tsov, S. I. In *Abst. Sci. Tech. Conf.*; Goskhimizdat: Leningrad, 1965; p 67 (in Russian).

(19) Suntola, T.; Antson, J.; Pakkala, A.; Lindfors, S. In *SID International Symposium*; Digest of Technical Papers: San Diego, 1980; p 108.

(20) Suntola, T.; Antson, J. Method for Producing Compound Thin Films. US4058430A, 1977.

(21) Puurunen, R. L. *Chem. Vap. Depos.* **2014**, *20* (10-11–12), 332–344.

(22) Parsons, G. N.; Elam, J. W.; George, S. M.; Haukka, S.; Jeon, H.; Kessels, E.; Leskelä, M.; Poodt, P.; Ritala, M.; Rossnagel, S. M. *Cit. J. Vac. Sci. Technol. A* **2013**, *31*, 50818.

(23) Alvaro, E.; Yanguas-Gil, A. *PLoS One* **2018**, *13* (1), e0189137.

(24) Dendooven, J.; Deduytsche, D.; Musschoot, J.; Vanmeirhaeghe, R. L.; Detavernier, C. *J. Electrochem. Soc.* **2010**, *157* (4), G111.

(25) Sprenger, J. K.; Cavanagh, A. S.; Sun, H.; Wahl, K. J.; Roshko, A.; George, S. M. *Chem. Mater.* **2016**, *28* (15), 5282–5294.

(26) Sprenger, J. K.; Sun, H.; Cavanagh, A. S.; George, S. M. *J. Vac. Sci. Technol. A* **2018**, *36* (1), 01A118.

(27) Sprenger, J. K.; Sun, H.; Cavanagh, A. S.; Roshko, A.; Blanchard, P. T.; George, S. M. *J. Phys. Chem. C* **2018**, *122* (17), 9455–9464.

(28) Sneh, O.; Clark-Phelps, R. B.; Londergan, A. R.; Winkler, J.; Seidel, T. E. *Thin Solid Films* **2002**, *402* (1–2), 248–261.

(29) Lee, B.; Kirkpatrick, C.; Choi, Y.-H.; Yang, X.; Wang, Y.; Yang, X.; Huang, A.; Misra, V. *ECS Transactions* **2011**, *41*, 445–450.

(30) George, S. M. *Chem. Rev.* **2010**, *110* (1), 111–131.

(31) Bent, S.; Loscutoff, P. W.; Clendenning, S. *MRS Proc.* **2010**, *1249*, 1249-F02-3.

(32) Cha, S. H.; Park, A.; Lee, K. H.; Im, S.; Lee, B. H.; Sung, M. M. *Org. Electron.* **2010**, *11* (1), 159–163.

(33) Liu, C.; Wang, C.-C.; Kei, C.-C.; Hsueh, Y.-C.; Perng, T.-P. *Small* **2009**, *5* (13), 1535–1538.

(34) Brahim, C.; Ringuedé, A.; Cassir, M.; Putkonen, M.; Niinistö, L. *Appl. Surf. Sci.* **2007**, *253* (8), 3962–3968.

(35) Biener, M. M.; Biener, J.; Wichmann, A.; Wittstock, A.; Baumann, T. F.; Bäumer, M.; Hamza, A. V. *Nano Lett.* **2011**, *11* (8), 3085–3090.

(36) Lu, J.; Elam, J. W.; Stair, P. C. *Acc. Chem. Res.* **2013**, *46* (8), 1806–1815.

(37) Törndahl, T.; Platzer-Björkman, C.; Kessler, J.; Edoff, M. *Prog. Photovoltaics Res. Appl.* **2007**, *15* (3), 225–235.

(38) Correa Baena, J. P.; Steier, L.; Tress, W.; Saliba, M.; Neutzner, S.; Matsui, T.; Giordano, F.; Jacobsson, T. J.; Srimath Kandada, A. R.; Zakeeruddin, S. M.; Petrozza, A.; Abate, A.; Nazeeruddin, M. K.; Grätzel, M.; Hagfeldt, A. *Energy Environ. Sci.* **2015**, *8* (10), 2928–2934.

(39) Schmidt, J.; Merkle, A.; Brendel, R.; Hoex, B.; de Sanden, M. C. M. van; Kessels, W. M. M. *Prog. Photovoltaics Res. Appl.* **2008**, *16* (6), 461–466.

(40) Kim, B. J.; Kim, D. H.; Lee, Y.-Y.; Shin, H.-W.; Han, G. S.; Hong, J. S.; Mahmood, K.; Ahn, T. K.; Joo, Y.-C.; Hong, K. S.; Park, N.-G.; Lee, S.; Jung, H. S. *Energy Environ. Sci.* **2015**, *8* (3), 916–921.

(41) Dong, X.; Fang, X.; Lv, M.; Lin, B.; Zhang, S.; Ding, J.; Yuan, N. *J. Mater. Chem. A* **2015**, *3* (10), 5360–5367.

(42) Jung, Y. S.; Cavanagh, A. S.; Dillon, A. C.; Groner, M. D.; George, S. M.; Lee, S.-H. *J. Electrochem. Soc.* **2010**, *157* (1), A75.

(43) Piper, D. M.; Travis, J. J.; Young, M.; Son, S.-B.; Kim, S. C.; Oh, K. H.; George, S. M.; Ban, C.; Lee, S.-H. *Adv. Mater.* **2014**, *26* (10), 1596–1601.

(44) Han, X.; Gong, Y.; Fu, K. (Kelvin); He, X.; Hitz, G. T.; Dai, J.; Pearse, A.; Liu, B.; Wang, H.; Rubloff, G.; Mo, Y.; Thangadurai, V.; Wachsman, E. D.; Hu, L. *Nat. Mater.* **2016**.

(45) Onoe, M. *Proceddings Inst. Radio Eng.* **1957**, *45* (5), 694.

(46) Sauerbrey, G. *Zeitschrift für Phys.* **1959**, *155* (2), 206–222.

(47) Collins, R. W.; Kim, Y. *Anal. Chem.* **1990**, *62* (17), 887–890.

(48) Bethe, H. E.; Hildebrandt, G. *Biogr. Mem. Fellows R. Soc.* **1988**, *34*, 134–176.

(49) Marra, W. C.; Eisenberger, P.; Cho, A. Y. *J. Appl. Phys.* **1979**, *50* (11), 6927–6933.

(50) Parratt, L. G. *Phys. Rev.* **1954**, *95* (2), 359–369.

(51) Siegbahn, K.; Nordling, C.; Fahlman, A.; Nordberg, R.; Hamrin, K.; Hedman, J.; Johansson, G.; Bergmark, T.; Karlsson, S.-E.; Lindgren, I.; Lindgren, B. *Nov. acta Regiae Soc. Sci. Ups. Ser. IV* **1967**, *20*.

(52) Magasinski, A.; Zdyrko, B.; Kovalenko, I.; Hertzberg, B.; Burtovyy, R.; Huebner, C. F.; Fuller, T. F.; Luzinov, I.; Yushin, G. *ACS Appl. Mater. Interfaces* **2010**, *2* (11), 3004–3010.

(53) Li, J.; Lewis, R. B.; Dahn, J. R. *Electrochem. Solid-State Lett.* **2007**, *10* (2), A17.

(54) Hochgatterer, N. S.; Schweiger, M. R.; Koller, S.; Raimann, P. R.; Wöhrle, T.; Wurm, C.; Winter, M. *Electrochem. Solid-State Lett.* **2008**, *11* (5), A76–A80.

(55) Munao, D.; van Erven, J. W. M.; Valvo, M.; Garcia-Tamayo, E.; Kelder, E. M. *J. Power Sources* **2011**, *196* (16), 6695–6702.

(56) Jeena, M. T.; Lee, J.-I.; Kim, S. H.; Kim, C.; Kim, J.-Y.; Park, S.; Ryu, J.-H. *ACS Appl. Mater. Interfaces* **2014**, *6* (20), 18001–18007.

(57) McNeill, I. C.; Sadeghi, S. M. T. *Polym. Degrad. Stab.* **1990**, *29* (2), 233–246.

(58) Nguyen, C. C.; Yoon, T.; Seo, D. M.; Guduru, P.; Lucht, B. L. *ACS Appl. Mater. Interfaces* **2016**, *8* (19), 12211–12220.

(59) Hays, K. A.; Ruther, R. E.; Kukay, A. J.; Cao, P.; Saito, T.; Wood, D. L.; Li, J. *J. Power Sources* **2018**, *384*, 136–144.

(60) Son, S.-B.; Wang, Y.; Xu, J.; Li, X.; Groner, M.; Stokes, A.; Yang, Y.; Cheng, Y.-T.; Ban, C. *ACS Appl. Mater. Interfaces* **2017**, *9* (46), 40143–40150.

(61) Piper, D. M.; Travis, J. J.; Young, M.; Son, S.-B.; Kim, S. C.; Oh, K. H.; George, S. M.; Ban, C.; Lee, S.-H. *Adv. Mater.* **2014**, *26* (10), 1596–1601.

(62) Ma, Y.; Martinez de la Hoz, J. M.; Angarita, I.; Berrio-Sanchez, J. M.; Benitez, L.; Seminario, J. M.; Son, S.-B.; Lee, S.-H.; George, S. M.; Ban, C.; et al. *ACS Appl. Mater. Interfaces* **2015**, *7* (22), 11948–11955.

(63) García, J. M.; García, F. C.; Serna, F.; de la Peña, J. L. *Prog. Polym. Sci.* **2010**, *35* (5), 623–686.

(64) Tashiro, K.; Kobayashi, M.; Tadokoro, H. *Macromolecules* **1977**, *10* (2), 413–420.

(65) Yang, H.; Wang, Y.; Duh, J.-G. *ACS Sustain. Chem. Eng.* **2018**, *6* (10), 13302–13311.

(66) Choi, N.-S.; Yew, K. H.; Choi, W.-U.; Kim, S.-S. *J. Power Sources* **2008**, *177* (2), 590–594.

(67) Chen, J.; Liu, Q.; Wang, B.; Li, F.; Jiang, H.; Liu, K.; Wang, Y.; Li, M.; Lu, Z.; Wang, D. *J. Electrochem. Soc.* **2017**, *164* (7), A1526–A1533.

(68) Higgs, D. J.; DuMont, J. W.; Sharma, K.; George, S. M. *J. Vac. Sci. Technol. A Vacuum, Surfaces, Film.* **2018**, *36* (1), 01A117.

(69) Sharma, K.; Hall, R. A.; George, S. M. *J. Vac. Sci. Technol. A Vacuum, Surfaces, Film.* **2015**, *33* (1), 01A132.

(70) Yersak, A. S.; Sharma, K.; Wallas, J. M.; Dameron, A. A.; Li, X.; Yang, Y.; Hurst, K. E.; Ban, C.; Tenent, R. C.; George, S. M. *J. Vac. Sci. Technol. A Vacuum, Surfaces, Film.* **2018**, *36* (1), 01A123.

(71) Oliver, W. C.; Pharr, G. M. *J. Mater. Res.* **1992**, *7* (06), 1564–1583.

(72) Wang, Y.; Zhang, Q.; Li, D.; Hu, J.; Xu, J.; Dang, D.; Xiao, X.; Cheng, Y.-T. *Adv. Energy Mater.* **2018**, *8* (10), 1702578.

(73) Elam, J. W.; Routkevitch, D.; Mardilovich, P. P.; George, S. M. *Chem. Mater.* **2003**, *15* (18), 3507–3517.

(74) Jin, Y.; Zhu, B.; Lu, Z.; Liu, N.; Zhu, J. *Adv. Energy Mater.* **2017**, *7* (23), 1700715.

(75) McDowell, M. T.; Lee, S. W.; Nix, W. D.; Cui, Y. *Adv. Mater.* **2013**, *25* (36), 4966–4985.

(76) Li, L.; Cabán-Acevedo, M.; Girard, S. N.; Jin, S. *Nanoscale* **2014**, *6* (4), 2112–2118.

(77) Girishkumar, G.; McCloskey, B.; Luntz, A. C.; Swanson, S.; Wilcke, W. *J. Phys. Chem. Lett.* **2010**, *1* (14), 2193–2203.

(78) Gao, B.; Sinha, S.; Fleming, L.; Zhou, O. *Adv. Mater.* **2001**, *13* (11), 816–819.

(79) Yao, Y.; Zhang, J.; Xue, L.; Huang, T.; Yu, A. *J. Power Sources* **2011**, *196* (23), 10240–10243.

(80) Wu, X.; Shi, Z.; Wang, C.; Jin, J. *J. Electroanal. Chem.* **2015**, *746*, 62–67.

(81) Molina Piper, D.; Lee, Y.; Son, S.-B.; Evans, T.; Lin, F.; Nordlund, D.; Xiao, X.; George, S. M.; Lee, S.-H.; Ban, C. *Nano Energy* **2016**, *22*, 202–210.

(82) Jury, W. A.; Vaux, H. *Proc. Natl. Acad. Sci. U. S. A.* **2005**, *102* (44), 15715–15720.

(83) LIGTT. *50 Breakthroughs: Critical scientific and technological advances needed for sustainable global development*; LBNL Institute for Globally Transformative Technologies: Berkeley, CA, 2014.

(84) Porada, S.; Zhao, R.; van der Wal, A.; Presser, V.; Biesheuvel, P. M. *Prog. Mater. Sci.* **2013**, *58* (8), 1388–1442.

(85) Suss, M. E.; Porada, S.; Sun, X.; Biesheuvel, P. M.; Yoon, J.; Presser, V.; Biesheuvel, M.; Yoon, J.; Presser, V. *Energy Environ. Sci.* **2015**, *8* (8), 2296–2319.

(86) La Mantia, F.; Pasta, M.; Deshazer, H. D.; Logan, B. E.; Cui, Y. *Nano Lett.* **2011**, *11* (4), 1810–1813.

(87) Pasta, M.; Wessells, C. D.; Cui, Y.; La Mantia, F. *Nano Lett.* **2012**, *12* (2), 839–843.

(88) Lee, J.; Kim, S.; Kim, C.; Yoon, J. *Energy Environ. Sci.* **2014**, *7* (11), 3683–3689.

(89) Conway, B. E. *J. Electrochem. Soc.* **1991**, *138* (6), 1539–1548.

(90) Cao, Y.; Xiao, L.; Wang, W.; Choi, D.; Nie, Z.; Yu, J.; Saraf, L. V.; Yang, Z.; Liu, J. *Adv. Mater.* **2011**, *23* (28), 3155–3160.

(91) Van Nghia, N.; Ou, P.-W.; Hung, I.-M. *Electrochim. Acta* **2015**, *161*, 63–71.

(92) Guo, S.; Yu, H.; Jian, Z.; Liu, P.; Zhu, Y.; Guo, X.; Chen, M.; Ishida, M.; Zhou, H. *ChemSusChem* **2014**, *7* (8), 2115–2119.

(93) Young, M. J.; Holder, A. M.; George, S. M.; Musgrave, C. B. *Chem. Mater.* **2015**, *27* (4), 1172–1180.

(94) Young, M. J.; Neuber, M.; Cavanagh, A. C.; Sun, H.; Musgrave, C. B.; George, S. M. *J. Electrochem. Soc.* **2015**, *162* (14), A2753–A2761.

(95) Mai, L.; Li, H.; Zhao, Y.; Xu, L.; Xu, X.; Luo, Y.; Zhang, Z.; Ke, W.; Niu, C.; Zhang, Q. *Sci. Rep.* **2013**, *3*, 1718.

(96) Simon, P.; Gogotsi, Y. *Nat. Mater.* **2008**, *7* (11), 845–854.

(97) Yuan, Y.; Zhan, C.; He, K.; Chen, H.; Yao, W.; Sharifi-Asl, S.; Song, B.; Yang, Z.; Nie, A.; Luo, X.; Wang, H.; Wood, S. M.; Amine, K.; Islam, M. S.; Lu, J.; Shahbazian-Yassar, R. *Nat. Commun.* **2016**, *7*, 13374.

(98) Chen, D.; Ding, D.; Li, X.; Waller, G. H.; Xiong, X.; El-Sayed, M. A.; Liu, M. *Chem. Mater.* **2015**, *27* (19), 6608–6619.

(99) Smith, K. C.; Dmello, R. *J. Electrochem. Soc.* **2016**, *163* (3), A530–A539.

(100) Yang, J.; Zou, L.; Song, H.; Hao, Z. *Desalination* **2011**, *276* (1–3), 199–206.

(101) Yang, J.; Zou, L.; Song, H. *Desalination* **2012**, *286*, 108–114.

(102) Toupin, M.; Brousse, T.; Bélanger, D. *Chem. Mater.* **2004**, *16* (16), 3184–3190.

(103) Yan, W.; Kim, J. Y.; Xing, W.; Donavan, K. C.; Ayvazian, T.; Penner, R. M. *Chem. Mater.* **2012**, *24* (12), 2382–2390.

(104) Jung, Y. S.; Cavanagh, A. S.; Riley, L. A.; Kang, S.-H.; Dillon, A. C.; Groner, M. D.; George, S. M.; Lee, S.-H. *Adv. Mater.* **2010**, *22* (19), 2172–2176.

(105) *Seawater Corrosion Handbook*; Schumacher, M., Ed.; Noyes Data Corporation: Park Ridge, New Jersey, 1979.

(106) Burton, B. B.; Fabreguette, F. H.; George, S. M. *Thin Solid Films* **2009**, *517* (19), 5658–5665.

(107) Martin, S. J.; Granstaff, V. E.; Frye, G. C. *Anal. Chem.* **1991**, *63* (20), 2272–2281.

(108) Martin, S. J.; Spates, J. J.; Wessendorf, K. O.; Schneider, T. W.; Huber, R. J. *Anal. Chem.* **1997**, *69* (11), 2050–2054.

(109) Porada, S.; Bryjak, M.; van der Wal, A.; Biesheuvel, P. M. *Electrochim. Acta* **2012**, *75*, 148–156.

(110) Porada, S.; Borchardt, L.; Oschatz, M.; Bryjak, M.; Atchison, J. S.; Keesman, K. J.; Kaskel, S.; Biesheuvel, P. M.; Presser, V. *Energy Environ. Sci.* **2013**, *6* (12), 3700–3712.

(111) Yang, S.; Jeon, S.; Kim, H.; Choi, J.; Yeo, J.; Park, H.; Kim, D. K. *ACS Sustain. Chem. Eng.* **2016**, *4* (8), 4174–4180.

(112) Cavanagh, A. S.; Wilson, C. A.; Weimer, A. W.; George, S. M. *Nanotechnology* **2009**, *20* (25), 255602.

(113) Ferguson, J. .; Weimer, A. .; George, S. . *Thin Solid Films* **2000**, *371* (1), 95–104.

(114) McCormick, J. A.; Cloutier, B. L.; Weimer, A. W.; George, S. M. *J. Vac. Sci. Technol. A Vacuum, Surfaces, Film.* **2007**, *25* (1), 67–74.

(115) Zydor, A.; Elliott, S. D. *J. Phys. Chem. A* **2010**, *114* (4), 1879–1886.

(116) Pasta, M.; Battistel, A.; La Mantia, F. *Energy Environ. Sci.* **2012**, *5* (11), 9487–9491.

(117) Lee, J.; Yu, S.-H.; Kim, C.; Sung, Y.-E.; Yoon, J. *Phys. Chem. Chem. Phys.* **2013**, *15* (20), 7690–7695.

(118) Kim, S.; Lee, J.; Kim, C.; Yoon, J. *Electrochim. Acta* **2016**, *203*, 265–271.

(119) Porada, S.; Weinstein, L.; Dash, R.; van der Wal, A.; Bryjak, M.; Gogotsi, Y.; Biesheuvel, P. M. *ACS Appl. Mater. Interfaces* **2012**, *4* (3), 1194–1199.

(120) Kim, T.; Dykstra, J. E.; Porada, S.; van der Wal, A.; Yoon, J.; Biesheuvel, P. M. *J. Colloid Interface Sci.* **2015**, *446*, 317–326.

(121) Rica, R. A.; Ziano, R.; Salerno, D.; Mantegazza, F.; Brogioli, D. *Phys. Rev. Lett.* **2012**, *109* (15), 156103.

(122) Franceschetti, D. R.; Macdonald, J. R. *J. Appl. Phys.* **1979**, *50* (1), 291–302.

(123) Murray, J. W. *J. Colloid Interface Sci.* **1974**, *46* (3), 357–371.

(124) Balistrieri, L. S.; Murray, J. W. *Geochim. Cosmochim. Acta* **1982**, *46* (6), 1041–1052.

(125) Avraham, E.; Bouhadana, Y.; Soffer, A.; Aurbach, D. *J. Electrochem. Soc.* **2009**, *156* (6), 95–99.

(126) Wallas, J. M.; Young, M. J.; Sun, H.; George, S. M. *J. Electrochem. Soc.* **2018**, *165* (10), A2330–A2339.

(127) Biesheuvel, P. M. *J. Colloid Interface Sci.* **2009**, *332* (1), 258–264.

(128) Zhao, R.; Biesheuvel, P. M.; Miedema, H.; Bruning, H.; van der Wal, A. *J. Phys. Chem. Lett.* **2010**, *1* (1), 205–210.

(129) Tsai, W.-Y.; Taberna, P.-L.; Simon, P. *J. Am. Chem. Soc.* **2014**, *136* (24), 8722–8728.

(130) Levi, M. D.; Levy, N.; Sigalov, S.; Salitra, G.; Aurbach, D.; Maier, J. *J. Am. Chem. Soc.* **2010**, *132* (38), 13220–13222.

(131) Haldane, F. D. M.; Anderson, P. W. *Phys. Rev. B* **1976**, *13* (6), 2553–2559.

(132) Wolverton, C.; Zunger, A. *Phys. Rev. Lett.* **1998**, *81* (3), 606–609.

(133) Raebiger, H.; Lany, S.; Zunger, A. *Nature* **2008**, *453* (7196), 763–766.

(134) Padilha, A. C. M. M.; Raebiger, H.; Rocha, A. R.; Dalpian, G. M. *Sci. Rep.* **2016**, *6*, 28871.

(135) Agarwal, A.; Kushner, M. J. *J. Vac. Sci. Technol. A Vacuum, Surfaces, Film.* **2008**, *26* (3), 498–512.

(136) Cao, Y.-C.; Zhao, L.; Luo, J.; Wang, K.; Zhang, B.-P.; Yokota, H.; Ito, Y.; Li, J.-F. *Appl. Surf. Sci.* **2016**, *366*, 304–309.

(137) Ma, T.; List, T.; Donnelly, V. M. *J. Vac. Sci. Technol. A Vacuum, Surfaces, Film.* **2017**, *35* (3), 031303.

(138) Miwa, K.; Takada, N.; Sasaki, K. *J. Vac. Sci. Technol. A Vacuum, Surfaces, Film.* **2009**, *27* (4), 831–835.

(139) Shiba, Y.; Teramoto, A.; Goto, T.; Kishi, Y.; Shirai, Y.; Sugawa, S. *J. Vac. Sci. Technol. A Vacuum, Surfaces, Film.* **2017**, *35* (2), 021405.

(140) Putkonen, M.; Sajavaara, T.; Johansson, L.-S.; Niinistö, L. *Chem. Vap. Depos.* **2001**, *7* (1), 44–50.

(141) Niinistö, J.; Putkonen, M.; Niinistö, L. *Chem. Mater.* **2004**, *16* (15), 2953–2958.

(142) de Rouffignac, P.; Park, J.; Gordon, R. G. *Chem. Mater.* **2005**, *17* (19), 4808–4814.

(143) Majumder, P.; Jursich, G.; Kueltzo, A.; Takoudis, C. *J. Electrochem. Soc.* **2008**, *155* (8), G152.

(144) Xu, R.; Selvaraj, S. K.; Azimi, N.; Takoudis, C. G. *ECS Trans.* **2013**, *50* (13), 107–116.

(145) Park, I.-S.; Chan Jung, Y.; Seong, S.; Ahn, J.; Kang, J.; Noh, W.; Lansalot-Matras, C. *J. Mater. Chem. C* **2014**, *2* (43), 9240–9247.

(146) Mai, L.; Boysen, N.; Subaşı, E.; Arcos, T. de los; Rogalla, D.; Grundmeier, G.; Bock, C.; Lu, H.-L.; Devi, A. *RSC Adv.* **2018**, *8* (9), 4987–4994.

(147) Pilvi, T.; Puukilainen, E.; Munnik, F.; Leskelä, M.; Ritala, M. *Chem. Vap. Depos.* **2009**, *15* (1–3), 27–32.

(148) Elam, J. W.; Sechrist, Z. A.; George, S. M. *Thin Solid Films* **2002**, *414* (1), 43–55.

(149) Bezuidenhout, D. F.; Clarke, K. D.; Pretorius, R. *Thin Solid Films* **1987**, *155* (1), 17–30.

(150) Krupa, J.; Queffelec, M. *J. Alloys Compd.* **1997**, *250* (1–2), 287–292.

(151) Zalkin, A.; Templeton, D. H. *J. Am. Chem. Soc.* **1953**, *75* (10), 2453–2458.

(152) Lee, Y.; Sun, H.; Young, M. J.; George, S. M. *Chem. Mater.* **2016**, *28* (7), 2022–2032.

(153) Nigara, Y. *Jpn. J. Appl. Phys.* **1968**, *7* (4), 404–408.

(154) Baldinozzi, G.; Bérar, J. F.; Calvarin-Amiri, G. *Mater. Sci. Forum* **1998**, *278–281*, 680–685.

(155) Kondati Natarajan, S.; Elliott, S. D. *Chem. Mater.* **2018**, *30* (17), 5912–5922.

(156) Jollet, F.; Noguera, C.; Gautier, M.; Thromat, N.; Duraud, J.-P. *J. Am. Ceram. Soc.* **1991**, *74* (2), 358–364.

(157) Zheng, J. X.; Ceder, G.; Maxisch, T.; Chim, W. K.; Choi, W. K. *Phys. Rev. B* **2006**, *73* (10), 104101.

(158) Lacroix, B.; Paumier, F.; Gaboriaud, R. J. *Phys. Rev. B* **2011**, *84* (1), 014104.

(159) Bevan, D. J. M.; Mohyla, J.; Hoskins, B. F.; Steen, R. J. *Eur. J. Solid State Inorg. Chem.* **1990**, *27* (3), 451–465.

(160) Zachariasen, W. H. *Acta Crystallogr.* **1951**, *4* (3), 231–236.